SAPIENZA
UNIVERSITÀ DI ROMA

Facoltà di Scienze Matematiche
Fisiche e Naturali

Tesi di dottorato in Fisica degli acceleratori
XXXI Ciclo

Material science and accelerator R&D: Reflectivity and Photo Yield measurements of vacuum chamber technical surfaces

Relatore
Prof. M. Migliorati

Correlatore
Dott. R. Cimino

Candidata
Eliana La Francesca

Matricola
1138498

Alla mia famiglia.

Contents

Introduction

A very large circular hadron collider seems, actually, to be the only approach to reach energy levels far beyond the range of the Large Hadron Collider (LHC), during the coming decades, so as to provide access to new particles with masses up to tens of TeV. The international Future Circular Collider (FCC) study is designing hadron, lepton and lepton-hadron colliders based on a new 100 km tunnel in the Geneva region. In particular for FCC-hh (hadron-hadron) the main focus and ultimate goal of the study are high-luminosity proton-proton collisions at a centre of mass energy of 100 TeV, using 16 T Nb_3Sn dipole magnets. The relativistic gamma factor ($\gamma = 53000$) is higher than those of many electron storage ring light sources. The wave lengths of the emitted photons are in the X-ray region, which is comparable with those as light sources.

One of the most important challenges in modern high energy colliders is represented by the effects due to Synchrotron Radiation (SR). SR can cause significant problems, like heat load on the accelerator walls, photon stimulated desorption, production of primary and secondary electrons (electron cloud effect) and consequently beam instability.

In general, radiation interacting with the accelerators vacuum walls can be either reflected or absorbed. The absorbed component can generate photoelectrons. The number and energy distribution of the photoemitted electrons depend on the SR spectrum (that can be exactly calculated from machine parameters like beam energy, radius of curvature, particle type, etc), as well as on detailed wall chamber composition, shape, roughness and reflective properties. In high energy hadron colliders, with a very large circumference, the incidence angle is very grazing. This implies that the photoelectrons are mainly created close to the surface, so that the detailed surface composition, contaminants and cryoadsorbates (in cold systems) become important in determining reflectivity properties of surfaces and Photo Yield (PY). PY, also known as quantum efficiency, measures the number of electrons generated per incident photon as a function of energy and incidence angle. Such material properties are important elements to determine beam instabilities and vacuum behaviour.

In dipoles, photoelectrons generated directly by SR are produced in the

orbit plane, hence the perpendicular dipole field will let them bounce back to the wall without interaction with the beam. On the other hand, reflected or scattered photons will also hit top and bottom of the vacuum chamber generating electrons parallel to the magnetic field. Such electrons, as in free field regions, will not be confined by the magnetic field and will interact with the relativistic beam. This could generate beam instabilities and initiate a secondary electron multiplication called e^-cloud multipacting. Electrons accelerated by the positive charge of the circulating beam will hit the opposite wall and generate other secondary electrons. In this way, a cascade effect can increase the e-cloud density. The number of secondary electrons depends on the Secondary Electron Yield (SEY) of the material. This evidence motivates various studies to mitigate SEY, through coatings, scrubbing and conditioning, laser treatments, etc.

In order to reduce SR reflectivity and to mitigate SEY and then the e-cloud build-up, Saw-Tooth structure and laser treated (LASE) copper which have been chosen for FCC-hh beam screen (BS).

The absorbed radiation also induces heat load. For example in, FCC-hh a Synchrotron Radiation Heat Load of 28.4 W/m/aperture in the arcs is predicted. This value is very large as compared to LHC where it is only 0.17 W/m/aperture. If one needs to dissipate such heat load on the cold bore, at temperature 1.9 K, 3 GW of power are necessary to cool the whole machine. This means that FCC-hh needs a Beam Screen (BS) to intercept SR and its heat load at highest possible temperature, compatible with all other constraints (vacuum, impedance etc).

It has been highlighted that also high reflectivity could be advantageous for reducing SR induced heat load in cold dipoles. Carbon coating (CC) of smooth vacuum chamber surfaces was suggested as a mean to reduce the heat load in cold part of the machine, by forward reflecting most SR and its deposited power towards ad hoc designed room temperature absorbers.

The present work experimentally investigates the behaviour of the accelerators wall representative materials in conditions close to operational environment. In this Ph.D. a systematic experimental campaign was carried out to study Reflectivity and Photo Yield of several Copper samples. The studied samples are:

- two copper samples with two smooth surfaces finished differently (one lapped and one elecro-polished);
- two copper samples with two smooth surfaces with 50 nm of Carbon Coating;
- LHC type Cu-colaminated on stainless steel sample, with and without Carbon Coating;
- LHC beam screen with Saw-Tooth structure;

- Laser Treated Copper sample made by the Science & Technology Facility Council (STFC).

We identified the Optics Beamline and the Reflectometer endstation in Berlin (HZB BESSY-II), as an ideal tool for the experimental investigations of the previous samples in realistic machine conditions. Access to this beamtime has been granted trough beamtime accepted proposals.

We studied reflectivity and photo yield in UV and XUV range (from 35 eV to 1800 eV) at grazing angles (0.25, 0.5 and 1 degree).

For technical surfaces, i.e surfaces with a degree of roughness with the same order of magnitude than accelerators beam pipe, it is important to consider that at very grazing angles, surface contaminants must be taken into account; furthermore, industrially prepared surfaces are sufficiently rough so that diffuse contribution is not negligible and Total Reflectivity is different from Specular Reflectivity.

The roughness value are obtained via AFM (Atomic Force Microscope) and the measurements are performed at the Centro di Ricerca per le Nanotecnologie applicate all'Ingegneria (CNIS) in Rome.

The Reflectivity measurements confirm the importance of air contaminants in Reflectivity behaviour and the role played by roughness. For technical surfaces, scattered light cannot be neglected and it is important to consider the Total Reflectivity (that is the Specular Reflectivity combined with the scattered light) instead of Specular Reflectivity component alone.

Carbon coating (CC) increases Total Reflectivity (as long as incidence angle is below its critical angle), in particular at higher energy, and reduces absorption and related Heat Load. Photo Yield does not seem to significantly depend on roughness and it decreases with CC.

For LASE Cu, reflectivity have been found to be substantially lower than for untreated copper and LHC Saw-Tooth sample.

Photo Yield measurements show a considerable reduction in LASE and LHC Saw-Tooth samples compared to flat samples, but very similar to each other.

This work is divided in four parts. In the first chapter main Synchrotron Radiation characteristics and problems, i.e. Heat Load, Gas load and electrons emission, the electron cloud phenomenon, and motivations of these studies, are presented. Reflectivity, its variation due to roughness and coating are described in the second chapter. Surface modifications and treatments (Saw-Tooth and Laser Ablation Surface Engineering) of studied samples are also discussed. The third and fourth chapters concern the experimental set-up description and the data analysis and results.

Chapter 1

Synchrotron Radiation detrimental effects

Synchrotron Radiation causes significant problems in particle accelerators like heat load on the accelerator walls, photon stimulated desorption, production of photo electrons (seeding electron cloud effect) and consequently beam instability. In this chapter the details of synchrotron radiation and its detrimental effects on machine operation are reported.

1.1 Synchrotron Radiation

Electromagnetic radiation is emitted by charged particles when accelerated. If the charged particles are accelerated radially ($\vec{v} \perp \vec{a}$) the light emitted is called magnetobremsstrahlung or *Synchrotron Radiation* (SR). The main characteristics of SR are:

- broad and continuous spectrum, which could cover from microwave to hard X-rays (gamma rays in Large Electron-Positron Collider (LEP)), depending on the energy and type of circulating particles;
- high intensity;
- high stability;
- pulsed time structure (in pulsed beam);
- polarization;
- natural narrow angular collimation;
- high brilliance.

All these properties depend on the characteristics of the machine (storage rings or colliders) and they are particularly useful to investigate the nature

and property of materials. However, SR can be a remarkable problem from the machine operation point of view. The principal problems and mitigation are described in this and the next chapters.

In fig. 1.1 a qualitative representation of radiation pattern is reported. Emission from a charged particle moving at a non relativistic speed, $v \ll c$ i.e. $\beta = v/c \ll 1$ (c is the speed of light), is similar to that of an oscillating dipole with its maximum intensity in the direction perpendicular to the acceleration and does not depend on the particle speed (fig. 1.1, side (a)).

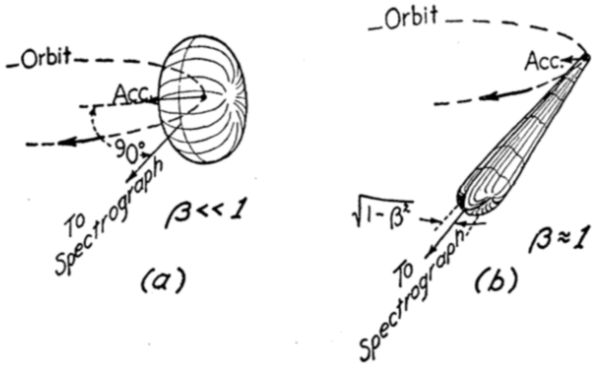

Figure 1.1: Qualitative radiation patterns to be expected from electrons on a circular orbit (a) at low energy and (b) as distorted by relativistic transformation at high energy. [96]

For relativistic effects, when the speed of emitting particles increases to relativistic values ($v \approx c$) the radiation pattern is compressed into a narrow cone in the direction of motion. The usual low-velocity toroidal radiation pattern with its zero at an angle of 90° to the directions of the maxima, as in fig. 1.1, side (a), is distorted and the emission is peaked in the direction of the velocity, resulting into an emission tangential to the particle orbit,(fig. 1.1, side (b)) [56, 68, 96].

The vertical half-opening angle is the inverse of Lorentz factor

$$\gamma^{-1} = \sqrt{1-\beta^2}, \qquad \beta = v/c.$$

The Power radiated by a particle on a surface is the flux of the Poynting vector:

$$\vec{S} = \frac{1}{\mu_0}\vec{E} \times \vec{B} \tag{1.1}$$

The electric and magnetic field generated by a charged particle in relativistic motion along a given trajectory, $\vec{x} = \vec{r}(t)$ can be computed starting from the fields expressed in terms of the Liénard-Wiechert potentials:

$$\vec{B} = -\vec{\nabla} \times \vec{A} \tag{1.2}$$

$$\vec{E} = \frac{\partial \vec{A}}{\partial t} - \vec{\nabla}\phi \tag{1.3}$$

where ϕ and $\vec{A}$ are:

$$\phi(\vec{x},t) = \left[\frac{e}{(1-\vec{\beta}\cdot\vec{n})R}\right]_{ret}, \qquad \vec{A}(\vec{x},t) = \left[\frac{e\vec{\beta}}{(1-\vec{\beta}\cdot\vec{n})R}\right]_{ret}. \tag{1.4}$$

Here $\vec{n}$ is a unit vector in the direction between particle and observer (see fig. 1.2). The subscript $[\quad]_{ret}$ means that the quantity in the square brackets has to be evaluated at the retarded time t', defined by

$$t = t' - \frac{R(t')}{c}.$$

Potentials and fields at the position x at time t are determined by the

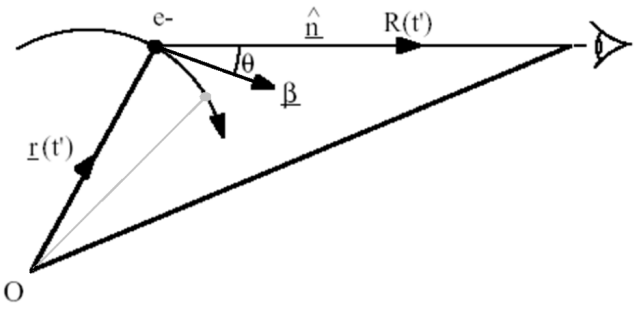

Figure 1.2: Present (t) and retarded(t') positions of a charge in motion. Gray line indicates the position of a particle ar time t

particle at time t', $t - t'$ is the time it takes for the radiation to travel the distance to the observer $R(t')$ and θ is the angle between velocity and observer.

The magnetic and electric fields, using Liénard-Wiechert potentials, can be written in the forms

$$\vec{B} = \frac{1}{c}[\vec{n}\times\vec{E}]_{ret} \tag{1.5}$$

$$\vec{E}(\vec{x},t) = \frac{e}{4\pi\varepsilon_0}\left[\frac{\vec{n}-\vec{\beta}}{\gamma^2-(1-\vec{\beta}\cdot\vec{n})^3R^2}\right]_{ret} + \frac{e}{4\pi\varepsilon_0 c}\left[\frac{\vec{n}\times[(\vec{(n)}-\vec{\beta})\times\dot{\vec{\beta}}]}{(1-\vec{\beta}\cdot\vec{n})^3R}\right]_{ret} \tag{1.6}$$

Looking at 1.5 and 1.6 we can divide the fields in two components: the *velocity field* or generalized Coulomb field (first term on the right side of eq. 1.6), which is independent from the acceleration, and radiation or *acceleration field* (second term on the right side of eq. 1.6), which depend

linearly on $\dot{\vec{\beta}}$ [56]. The second term is dominant in both circular and linear accelerators.

In non relativistic conditions the acceleration field can be written as:

$$\vec{E}_a(\vec{x},t) = \frac{e}{4\pi\varepsilon_0 c}\left[\frac{\vec{n}\times(\vec{n}\times\dot{\vec{\beta}})}{R}\right]_{ret} \tag{1.7}$$

this implies that the power radiated per unit solid angle is:

$$\frac{dP}{d\Omega} = \frac{1}{\mu_0 c} \mid R\vec{E}_a \mid^2 = \frac{e^2}{(4\pi)^2\varepsilon_0 c} \mid \vec{n}\times(\vec{n}\times\dot{\vec{\beta}}) \mid^2 . \tag{1.8}$$

The total instantaneous radiated power is given by integrating $dP/d\Omega$ over the solid angle and is given by the Larmor's formula:

$$P = \frac{e^2}{6\pi\varepsilon_0 c} \mid \dot{\vec{\beta}} \mid^2 \tag{1.9}$$

This result can be generalized in relativistic case as:

$$P = \frac{e^2}{6\pi\varepsilon_0 c}\gamma^6\left[\left|\dot{\vec{\beta}}\right|^2 - \left|\vec{\beta}\times\dot{\vec{\beta}}\right|\right]. \tag{1.10}$$

The result obtained in 1.10 means that for linear accelerators (LINAC)

$$P = \frac{e^2}{6\pi\varepsilon_0 m^2 c^3}\left|\frac{d\vec{p}}{dt}\right|^2 \tag{1.11}$$

where m is the rest mass of the particle, and $\vec{p}$ its momentum. In circular trajectories, on the contrary, the total radiated power is:

$$P = \frac{e^2}{6\pi\varepsilon_0 m^2 c^3}\gamma^2\left|\frac{d\vec{p}}{dt}\right|^2 ; \tag{1.12}$$

i.e.

$$P(v \parallel a) \approx 1/\gamma^2 P(v \perp a).$$

The power radiated in LINAC is negligible compared to the one in circular accelerators.[1] In circular machines the total instantaneous power radiated by a particle can be written as:

$$P = \frac{e^2}{6\pi\varepsilon_0 c}\left|\dot{\vec{\beta}}\right|^2\gamma^4 = \frac{e^2 c}{6\pi\varepsilon_0}\frac{\gamma^4}{\rho^2} = \frac{e^4\beta^6}{6\pi\varepsilon_0 m^4 c^5}E^2B^2 \tag{1.13}$$

with E particle energy. The equation 1.13 implies:

[1] Nevertheless, this is not true for high energy LINAC. The emission of Synchrotron Radiation in the CLIC beam-delivery system (BDS) is one of the major limitations of the machine performance [32].

- Strong dependence on the rest mass of the particle ($\propto 1/m^4$);
- Proportionality to value of bending radius ($\propto 1/\rho^2$);
- Proportionality to the magnetic field of the bending dipoles ($\propto B^2$).

For high energy electrons ($\beta \simeq 1$) the Energy Loss per turn, per particle, is (in practical units)[56, 93]:

$$U_{0,electrons}(keV) = \frac{e^2\gamma^4}{3\varepsilon_0\rho} = 88.46\frac{E^4(GeV)}{\rho(m)} \tag{1.14}$$

and the power radiated by a beam of average current I_b

$$P_{electrons}(kW) = \frac{e^2\gamma^4}{3\varepsilon_0\rho}I_b = 88.46\frac{E^4(GeV)I(A)}{\rho(m)}; \tag{1.15}$$

for proton beams the equations 1.14 and 1.15 become:

$$U_{0,protons}(keV) = \frac{e^2\gamma^4}{3\varepsilon_0\rho} = 7.783\frac{E^4(TeV)}{\rho(m)} \tag{1.16}$$

$$P_{protons}(kW) = \frac{e^2\gamma^4}{3\varepsilon_0\rho}I_b = 7.783\frac{E^4(TeV)I(A)}{\rho(m)}. \tag{1.17}$$

The energy radiated per unit frequency interval per unit solid angle is [56]:

$$\frac{d^3I}{d\Omega d\omega} = \frac{3e^2}{16\pi^3\varepsilon_0 c}\left(\frac{2\omega\rho}{3c\gamma^2}\right)^2\left(1+\gamma^2\theta^2\right)^2\left[K^2_{2/3}(\xi) + \frac{\gamma^2\theta^2}{1+\gamma^2\theta^2}K^2_{1/3}(\xi)\right] \tag{1.18}$$

where the function K is a modified Bessel function of the second kind, θ is the latitude with respect to the orbit plane. Only for very small values of θ there will be an appreciable radiation intensity. The parameter ξ is defined as:

$$\xi = \frac{\rho\omega}{3c\gamma^3}\left(1+\gamma^2\theta^2\right)^{3/2} \tag{1.19}$$

The first term in the square bracket of 1.18 corresponds to radiation polarized in the plane of orbit, and the second to radiation polarized perpendicular to that plane.

The properties of modified Bessel functions (see [56]) are such that the radiation intensity is negligible for $\xi \gg 1$, i.e. for large angles. Higher is the frequency, smaller is the critical angle beyond which there will be negligible radiation. The critical frequency ω_c beyond which there is negligible radiation at any angle is defined as the frequency when $\xi = 1/2$ and $\theta = 0$. So,

$$\omega_c = \frac{3}{2}\frac{c}{\rho}\gamma^3 \tag{1.20}$$

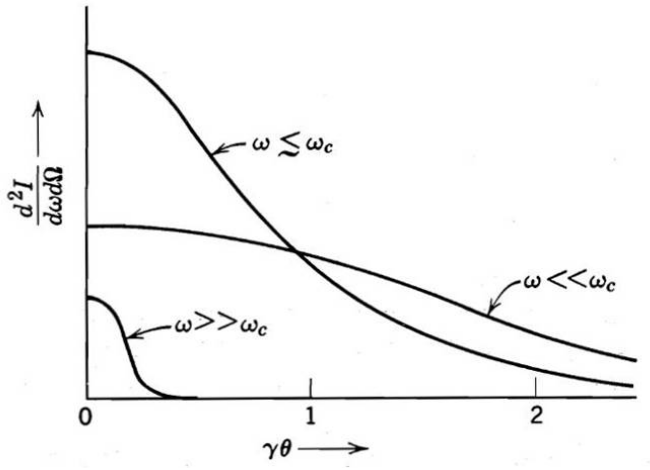

Figure 1.3: Differential frequency spectrum as a function of angle. For frequencies comparable to the critical frequency ω_c, the radiation is confined to angles of the order of γ^{-1}. For much smaller (larger) frequencies, the angular spread is larger (smaller). [56]

and the critical angle is defined as the angle for which

$$\xi(\theta_c) \simeq \xi(0) + 1 \tag{1.21}$$

and is approximately

$$\theta_c \simeq \frac{1}{\gamma}\left(\frac{2\omega_c}{\omega}\right)^{1/3} \tag{1.22}$$

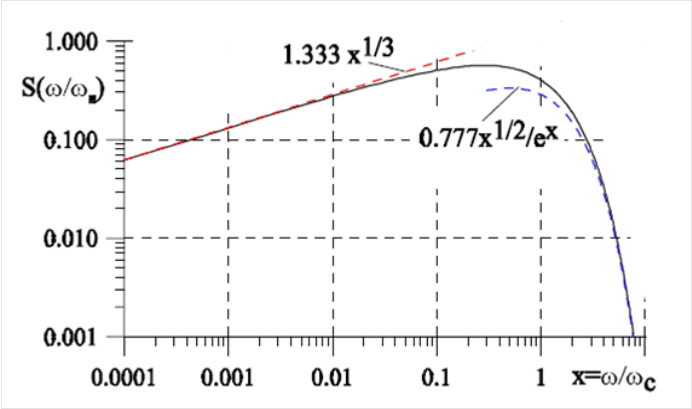

Figure 1.4: Frequency distribution of radiated energy, the red (blue) dashed line shows the behaviour for $\omega \ll \omega_c$ ($\omega \gg \omega_c$,).

For frequencies much larger than the critical frequency and angles much larger than the critical angle, synchrotron radiation emission is negligible. Figure 1.3 shows the angular distribution for frequencies related to ω_c: the high energy components are confined to a very small angular range.

Integrating over all angles yields the spectral density distribution, see fig. 1.4 and it is interesting to note that

$$\frac{dI}{d\omega} \propto \omega^{1/3} \quad for \quad \omega \ll \omega_c, \qquad \frac{dI}{d\omega} \propto \omega^{1/2} e^{-\omega} \quad for \quad \omega \gg \omega_c, \tag{1.23}$$

the peak occurs approximately at 0.3 ω_c. The critical frequency splits the spectrum in two parts each of which contains half of the total energy radiated.

We define the critical photon energy as

$$\varepsilon_c = \hbar\omega_c = \frac{3}{2}\frac{\hbar c}{\rho}\gamma^3. \tag{1.24}$$

with $\hbar = h/2\pi$ reduced Planck constant. The number of photons emitted by a particle per meter is expressed as [74]:

$$N_\gamma = \frac{5\alpha}{2\sqrt{3}}\frac{\gamma^3}{\rho} \tag{1.25}$$

where $\alpha = \frac{1}{4\pi\varepsilon_0}\frac{e^2}{\hbar c}$ is the fine-structure constant. Then, the relationship between radiated power and photon energy is shown in figure 1.5. The increase of critical energy pushes the radiation on high energy photons. Note that, there is no dependence on the critical energy at longer wavelength.

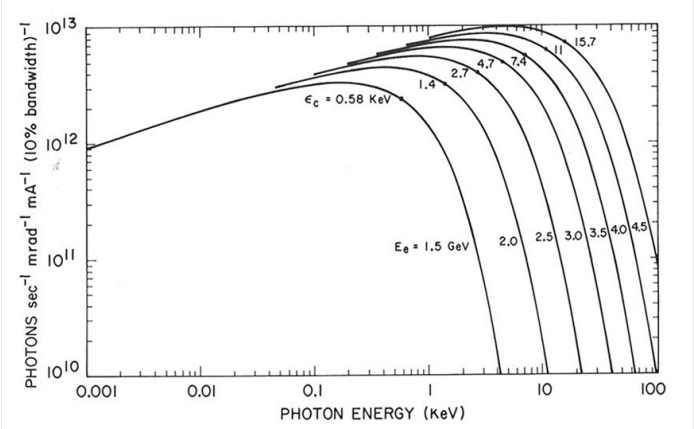

Figure 1.5: Dependence of the frequency distribution of radiated energy via synchrotron emission on the particle (in this case electron) energy.

The three main effects of SR on an accelerator (especially on the vacuum system) are given below (see fig.1.6).

- Heat load: when SR hits a surface, it transfers its energy to the surface. The SR heats up the beam pipe, and sometimes damages it by excess heating and thermal stress.

- Gas load: when SR hits a surface, it desorbs gas molecules from the surface. The gas desorption increases vacuum pressure. The pressure rise reduces the beam lifetime and increases background noise in the detector.
- Emission of electrons: when SR hits a surface, the surface emits electrons. The emitted photoelectrons enhance the formation of the electron cloud, which leads to electron cloud instabilities (for positive beams)[90].

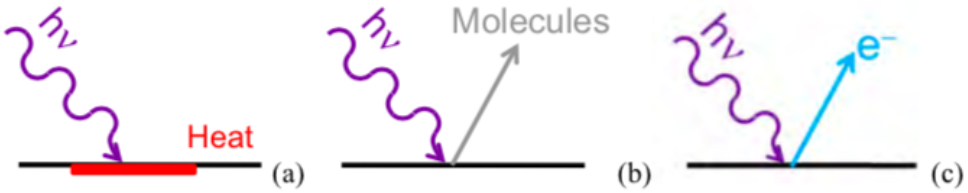

Figure 1.6: Three principal effects of Synchrotron Radiation interaction with accelerator walls. (a) heat load, (b) gas desorption, (c) electron emission.

Thus, the study of light distribution is important, not only as emitted from the proton beam (SR), but also after different reflections, which will occur in the vacuum pipe.

1.2 Synchrotron radiation in FCC-hh

All the discussions made up to now are completely general and apply to every accelerator. Now we want to go into details and calculate the synchrotron radiation for accelerators such as LHC and FCC-hh.

In the previous section we have seen that the power emitted by synchrotron radiation in proton accelerators becomes not negligible in the TeV range (see equations 1.16 and 1.17), i.e. in the operative area of modern hadron colliders. In fact, for proton colliders preceding LHC, SR was always negligibly small owing to the large proton mass. For the LHC, SR influenced the design only through the efforts needed to avoid dissipating the radiated energy at liquid Helium temperature. The post-LHC future circular collider will be the first for which beam dynamics and ring optimization will be dominated by SR [93].

The FCC-hh is designed to reach 100 TeV in the centre of mass, increasing considerably the current limit of LHC 14 TeV. To do this challenging result 100 km of tunnel are necessary and 16 T superconducting Nb_3Sn magnets. Such dipoles need cryogenic system at supercritical helium temperature (cold bore temperature 1.9 K).

Table 1.1: Comparison of the LHC, HL LHC (HiLumi i.e. High Luminosity upgrade of LHC) and FCC-hh design parameters [1].

	LHC (design)	**HL-LHC**	**FCC-hh** baseline	**FCC-hh** ultimate
c.m. Energy [TeV]	14		100	
Circumference C [km]	26.7		100	
Dipole field [T]	8.33		16	
Arc filling factor	0.79		0.79	
Numper of bunches n at - 25 ns - 50 ns	2808		10600 53000	
Bunch population N [10^{11}] - 25 ns - 5 ns	1.15	2.2	1.0 0.2	
Beam current [A]	0.584	1.12	0.5	
Peak luminosity [10^{34} cm^{-2} s^{-1}]	1.0	5.0	5.0	< 30.0
Stored energy per beam [GJ]	0.392	0.694	8.4	
SR power per ring [MW]	0.0036	0.0073	2.4	
Arc SR heat load [W/m/aperture]	0.17	0.33	28.4	
Energy loss per turn [MeV]	0.0067		4.6	
Critical photon energy [keV]	0.044		4.3	

In table 1.1 some relevant parameters of FCC-hh and their comparison with LHC and H-L LHC are reported. In particular, it is important to

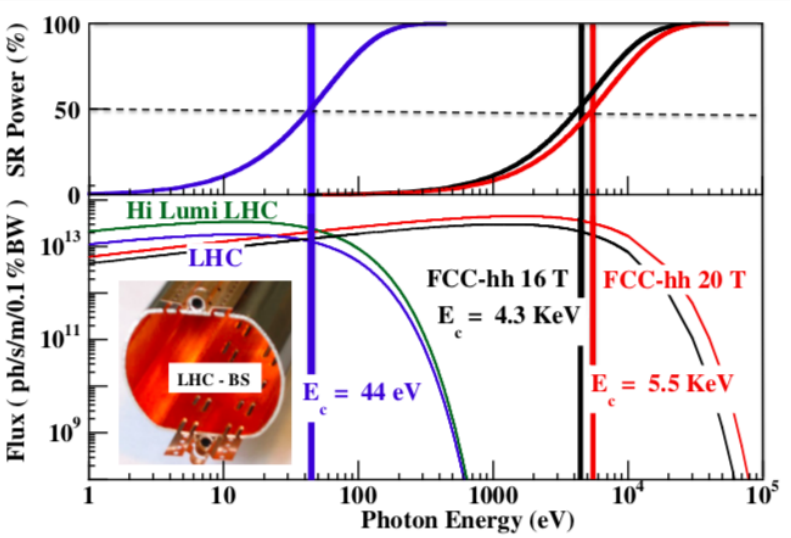

Figure 1.7: Calculated SR properties and critical energies ε_c for nominal parameters of: LHC, HL-LHC, FCC-hh with 16 and 20 T dipole magnets. Top panel: percentage of SR power carried by all photons at lower energies than a given photon energy ($h\nu$); Bottom panel: Calculated SR Flux. Inset: picture of LHC Beam Screen [25].

highlight the high values of SR power radiated per ring (2.4 MW vs 0.0036 MW), Arc SR heat load (28.4 W/m/aperture vs 0.17 W/m/aperture) and the critical photon energy (4.3 keV vs 44 eV).

In fig. 1.7, spectra of SR (top panel) and the power transported in FCC-hh (bottom panel) are reported. In FCC-hh the critical energy is in the X-ray range, the radiation will impinge onto accelerators wall at $\sim$ 21 m from the source with an incidence angle 0.077°(1.35 mrad) and photon fan strip $\sim$ 2 mm. In LHC the majority of the photons are generated in IR-UV range, while in FCC-hh more than half photons are in the soft and hard X-rays region.

FCC-hh is characterised, also, by a high photon flux, defined as[75]:

$$\dot{\Gamma}[photons/m/s] = 7.017 \cdot 10^{16} \cdot \frac{E[TeV]}{\rho[m]} \cdot I_b[mA]. \tag{1.26}$$

It is commonly accepted that the generation of photoelectrons starts from a photon energy of $\sim$4 eV, corresponding to the typical work-function value of the materials irradiated by the SR photons (copper, stainless steel). In the LHC, for baseline conditions, the flux is $1 \cdot 10^{17}$ ph/s/m, and only 52% of this amount is above 4 eV. In the FCC-hh, on the other hand, the flux $1.7 \cdot 10^{17}$ ph/s/m with 88 % of the flux above 4 eV, meaning in

fact more than 2.5 times higher effective SR flux [75]. However, SR can interact directly with adsorbates binding energy and activate gas load also behind 4 eV.

1.3 Heat load

When SR hits the inner wall of a beam pipe, it transfers energy to the surface, resulting in heating. This problem is particularly delicate in cryogenic machines. In fig.1.8 the minimum power (Carnot's efficiency) needed to remove 1 W from a cold surface varying its temperature is reported. At low temperature, we can write the Carnot efficiency as:

$$\eta = \frac{T_w}{T_c} - 1 \approx \frac{T_w}{T_c} \tag{1.27}$$

where T_w is ambient temperature (300 K) and T_c is cold temperature, which we consider that of cold bore (1.9 K). The power needed to dissipate the high FCC-hh heat-load, on two arcs of 100 km, in Carnot limit is:

$$P_{Carnot} = 2 \cdot HL_{Arc} \cdot \eta \cdot C = 28.4 \cdot \frac{300}{1.9} \cdot 100000 \cdot m \cdot \frac{W}{m}$$

where HL_{Arc} is the heat load per Arc and C is the ring circumference. Typically, the efficiency with respect to Carnot cycle is 0.3, for which:

$$P \simeq P_{Carnot}/0.3 \simeq 28.4 \cdot \frac{300}{1.9} \cdot \frac{1}{0.3} \cdot 100000 \cdot m \cdot \frac{W}{m} \approx 3GW \tag{1.28}$$

i.e. an enormous quantity of power at the plug. To avoid this problem in LHC the Beam Screen (BS) was introduced.

The main purpose of the BS is to intercept the beam induced heat load before it reachs the cold mass at lowest temperature. BS operation temperature must be such to minimize the total energy loss. In tab. 1.2 the intensity and origin of BS heat loads [W/m/aperture] for the present LHC and its upgrades, High Luminosity and High Energy, are reported. In fact, not only SR is the origin of Heat Load, but also the presence of electron cloud (see next) and beam induced image current in the resistive wall.

In FCC-hh synchrotron radiation from the beams is both "harder" (X-rays) and more intense with respect to LHC. Beam screens, already mandatory for LHC for cryogenic reasons, are compulsory for High Luminosity LHC and FCC-hh to absorb the synchrotron radiation at higher temperature than that of the superconducting magnets and thus reduce the entropic load on the refrigeration system. The actual design of FCC-hh BS will be discussed in the next chapter.

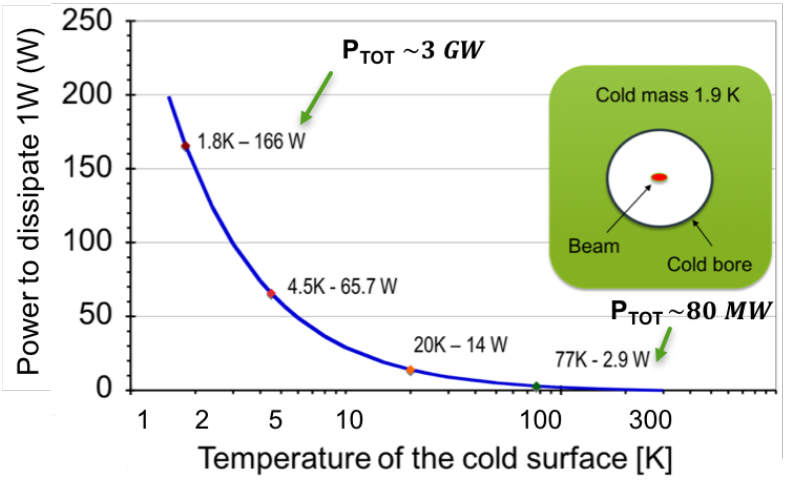

Figure 1.8: Minimum power (Carnot) needed to remove 1 W from a cold surface at different temperature values [58].

Table 1.2: Beam screen heat load for present LHC and its upgrade [12].

Case	Temperature K	Sync. radiation W/m/aperture	Image current W/m/aperture	Electron cloud W/m/aperture	Total
LHC nominal	5 - 20	0.17	0.18	0.45	0.79
LHC ultimate	5 - 20	0.24	0.39	0.79	1.40
HL-LHC 25 ns	5 - 20	0.32	0.66	1.00	2.00
HL-LHC 50 ns	5 - 20	0.25	0.83	0.36	1.40
HE-LHC 50 ns	5 - 20	2.90	0.22	0.12	3.20
HE-LHC 50 ns	40 - 60	2.90	1.20	0.12	4.20

HL-LHC: high luminosity upgrade (14 TeV center of mass energy, $\sim 10^{35}$ cm^{-2} s^{-1} luminosity)
HE-LHC: high energy upgrade (33 TeV center of mass energy, $\sim 2 \cdot 10^{34}$ cm^{-2} s^{-1} luminosity)
25 ns and 50 ns refer to spacing of particle bunches

The design of the beam screen is important not only to reduce the energy load of the cryogenic system, but it is also an essential feature to ensure good vacuum conditions and to limit the development of collective effects and beam instabilities [12].

1.4 Beam induced desorption

The general equation describing the molecular density of the residual gas in the vacuum chamber is given by [18, 75]:

$$n_g = \frac{P}{k_B T} = \frac{Q}{S \cdot k_B T}$$
$$n_g = \frac{(\eta_{ph} + \eta'_{ph}) \cdot \dot{\Gamma}_{ph} + (\eta_e + \eta'_e) \cdot \varphi_e + \Sigma(\eta_j + \eta'_j) \cdot \sigma_g \cdot \frac{I_b}{e} n_g + A \cdot q_g}{S \cdot k_B T} \tag{1.29}$$

Where:
n_g is the molecular gas density,
P is the pressure,
k_B is the Boltzmann constant,
T is the temperature,
Q is the outgassing,
η_{ph} and η'_{ph} are the primary and secondary photon molecular desorption yield (MDY), respectively,
η_e and η'_e are the primary and secondary electron MDY,
η_j and η'_j are the primary and secondary ion MDY,
$\dot{\Gamma}_{ph}$ is the photon flux on the chamber wall,
φ_e is the electron impingment rate hitting the chamber's wall,
σ_g is the gas ionization cross section,
A is the area,
q_g is the thermal outgassing.

In general atomic or simple molecular desorption will typically be a first-order process (i.e. a simple molecule on the surface of the substrate desorbs into a gaseous form). Recombinative molecular desorption will generally be a second-order process (two hydrogen atoms on the surface desorb and form a gaseous H_2 molecule).

In equation 1.29 it is possible to recognize four different contributions: photon-induced desorption, electron-induced desorption, ion-induced desorption and thermal outgassing. Synchrotron radiation plays a role in three of these mechanisms. In fact, SR can induce desorption directly (also behind 4 eV), it can generate photo-electrons (see next section), it can be absorbed heating the surface and consequently favour a thermal outgassing (residual gas can be ionized directly by the positevely charged beam). Let's consider the Photon Stimulated Desorption (PSD) process where SR photons trigger the desorption of gas molecules from the vacuum chamber when they hit the walls.

For a given material, the lower is the temperature the lower is the molecular desorption. The reason of this phenomenon is that gas molecules at low temperature need a higher amount if transferred energy to be released [10]. In fig. 1.9 primary photodesorption coefficient for a stainless steel surface at room temperature, 77 K and 4.2 K at a critical photon energy of 45.3 eV are shown. Another interesting aspect of PSD is its dependence on SR critical energy [42]. MDY is higher for higher critical energy. In fig. 1.10 MDY dependence on ε_c for the common gas species of baked Cu at RT are shown, the values of SR critical energy for LHC and FCC-hh are reported too.

During machine operation, 'beam cleaning' of the vacuum system effectively reduces the molecular desorption yield by several orders of

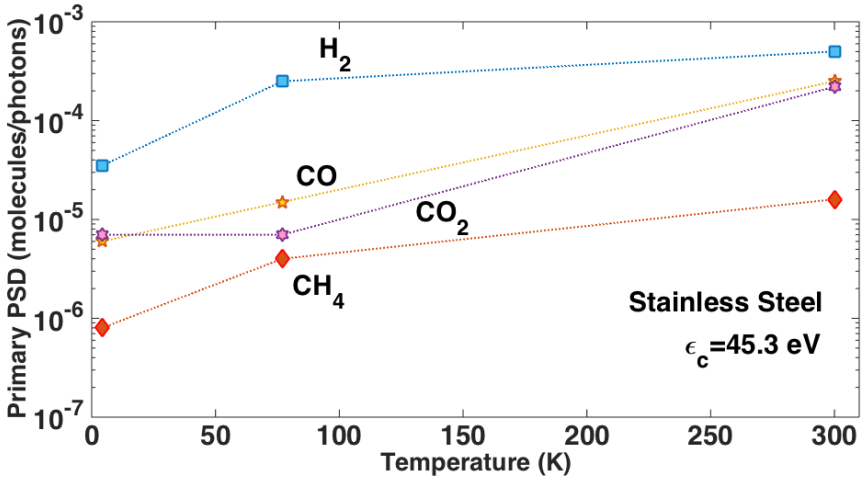

Figure 1.9: Measured primary photodesorption yield(molecules/photon) of a stainless steel surface, at normal incidence, at room temperature, 77 K and 4.2 K at a critical photon energy of 45.3 eV [10].

magnitude. Since it would be very expensive to build a vacuum system with sufficient pumping speed to guarantee the required beam lifetime at the start-up, most synchrotron light sources and storage rings take advantage of the beam cleaning process. It is an accepted design concept that the required vacuum performance will be achieved after an initial conditioning time only. The cleaning time or, more specifically, the integrated beam dose which is required to reduce the molecular desorption yield from its initial large value, can be estimated with good accuracy using the exponential dependence on the beam dose D (mA h) [44]:

$$\eta = \eta_0 \cdot D^{-a} \tag{1.30}$$

Where η is the yield depending on the dose,
η_0 is the initial yield,
D is the photon dose (photons/meter),
a is the decaying slope, it is found to vary between 0.6 to $\sim$1 and is depending on the specific machine.

In cryogenic temperature operation machines there is an increase of the desorption yield due to the condensed gas layers being released at lower energies as the thickness of the layer increases. This effect, typically, does not happen inside the beam screen considering that the high radiation flux present is such to clean the surface and setting the coverage in an equilibrium state. However, it has been taken into account for the case of the cold bore, where all the desorbed gas from inside the BS is accumulated over time and the leaked radiation through the pumping holes can trigger its secondary desorption. The coverage can then grow up to considerably

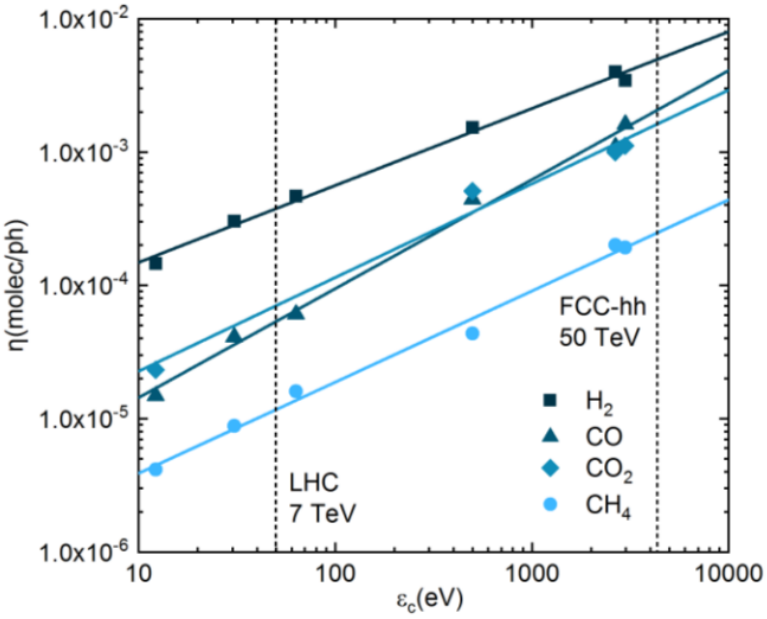

Figure 1.10: MDY dependence on ε_c for the common gas species of baked Cu at RT [7, 42, 75].

high levels, yielding an increase of MDY of several orders of magnitude higher than a bare surface just within the first days of vacuum conditioning [75].

1.5 Electron cloud phenomenon

When SR hits the vacuum chamber surface, photoelectrons are emitted. The quantum efficiency, or Photo Yield (PY), measures the number of electrons generated per incident photon as a function of incidence angle, surface roughness, characteristics of the material, photon energy. If the beam is positively charged (like in LHC and FCC-hh), it attracts the electrons. The electrons, accelerated by the next bunch's field, hit the surface again and emit other electrons (secondary electrons). Depending on several parameters as surface reflectivity, photo-emission and secondary-emission yield (SEY), this mechanism can lead to the fast build-up of an electron cloud with potential implications for beam stability and heat load on the cold beam screen [81].

In fig. 1.11 an artistic view of the e^-cloud process is reported. Lower is the energy of secondary electron higher is the probability to survive in the time between two bunches.

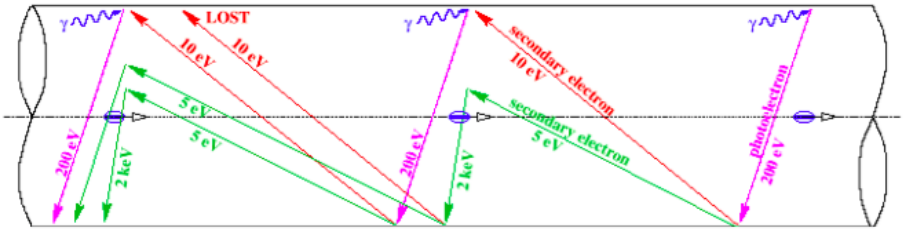

Figure 1.11: Artistic view of the e⁻cloud build up. Original representation by F. Ruggiero.

1.5.1 Electron cloud build up

It has to be noticed that photoelectrons are not the only possible seed to initiate the e⁻cloud process. Electron cloud effect (ECE) has been observed to occur also in Proton Synchrotron (PS) and Super Proton Synchrotron (SPS) where SR has not enough energy to generate photoelectrons [9, 53]. In general, in fact, primary electrons can be generated also by:

- beam loss (ion beams case),
- ionization of the residual gas in the chamber,
- impact on the wall at grazing angles of particles lost by the beam.

Let's consider primary electrons generated by SR. The rate of their production can be estimated by [26]:

$$\frac{dN_{e\gamma}}{ds} \approx PY \frac{dN_\gamma}{ds} \approx PY \frac{5}{2\sqrt{3}} \frac{\alpha\gamma}{\rho} \tag{1.31}$$

where:
dN_γ/ds is the number of photons emitted in a dipole per unit length and per particle,
PY is the photo yield,
γ is the Lorentz factor,
α is fine structure constant,
ρ is curvature radius.

The geometrical distribution of the photo-emitted electrons in the beam pipe depends also by shape and reflectivity, R, of the chamber wall. In the next chapter we will see the PY and R properties more in detail. In dipoles the photo-emitted electrons in orbit plane are constrained to move along the field lines (because of the magnetic field) with a small cyclotron radius. The consequence of this it is that they will not impinge the accelerator walls and consequently will not partecipate to e⁻cloud build up. Nevertheless, the reflected component of SR will illuminate

top and bottom walls generating electrons perpendicularly to the orbit plane. Such photoelectrons are not confined by magnetic field and then spiral along the field lines activating a cascade effect that leads to the formation of an electron cloud. Furthermore, SR, in its reflection, can generate electrons in a drift tube, where there is no field able to confine them and they will participate to multipacting.

We have said that the primary electrons can also be generated by ionization of residual gas. In this case the number of electrons produced per unit length by a bunch of N_b particles is:

$$\frac{dN_{e,ion}}{ds} = N_b \cdot \frac{P}{RT} \cdot \sigma_{ion} \tag{1.32}$$

where P is the pressure, T is the temperature, R is the gas constant and σ_{ion} is the ionization cross section.

The last mechanism able to generate primary electrons is due to particles lost by the beam. In this case they will produce a large number of electrons impacting on the wall at grazing angle. This mechanism is typical of heavy ions beams [94].

Primary electrons are non-relativistic ($v \ll c$) but, in presence of highly relativistic positive beam, they are attracted by the bunch in direction orthogonal to the orbit plane. The energy transfer is simple to analyse if the electron is far away from the beam. In this case, the electron is essentially stationary as a bunch passes, and the effect of the bunch can be considered simply that of changing the momentum of the electrons by an amount which only depends on its radial position in the beam pipe (*kick approximation*, see fig. 1.12). This is often the situation for the photoelectrons when they are first produced.

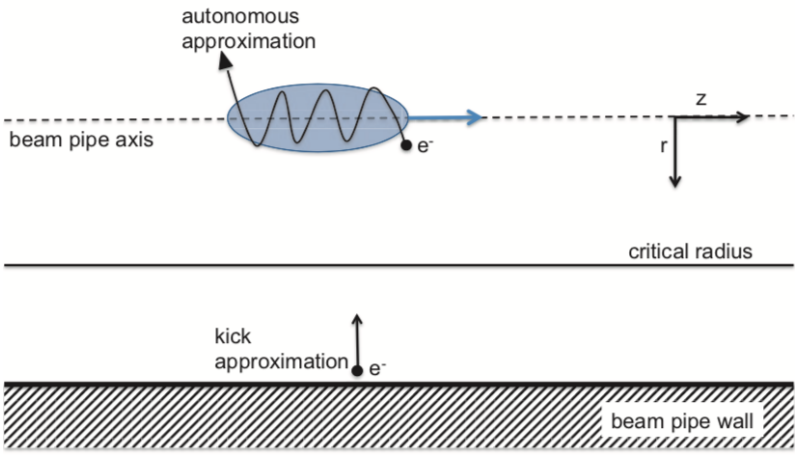

Figure 1.12: Electron beam interaction in kick and autonomous approximation in a cylindrical beam pipe [26].

However, particles which are closer to the beam can get temporarily trapped in the radial potential of the bunch, and will thus oscillate around it (*autonomous regime*). The energy transfer to such particles is more difficult to analyse [16]. There is a critical radius r_c that separates these two regimes (see fig. 1.12). It can be calculated as:

$$r_c \approx 2\sqrt{N_b r_e \sigma_z \sqrt{\frac{2}{\pi}}} \tag{1.33}$$

where N_b is the number of particles in the bunch, σ_z the bunch length, r_e the classical radius of the electron. The energy gain in the two regimes can be written as [26]:

$$\Delta E_{kick} = 2m_e c^2 \left(\frac{N_b r_e}{r}\right)^2 \tag{1.34}$$

and

$$\Delta E_{bunch} = \frac{1}{2} m_e \omega_e^2 \sigma_r^2 \tag{1.35}$$

where m_e is electron mass, c is speed of light, r is the distance between bunch and electron, σ_z the bunch length, σ_r is the bunch radius (in cylindrical and uniform approximation) and ω_e is the harmonic oscillation frequency of electrons trapped inside the bunch:

$$\omega_e = c\sqrt{\frac{2\pi r_e N_b}{\sigma_r^2 \sigma_z}}. \tag{1.36}$$

In figure 1.13 an example of photoelectron energy distribution at the moment of emission (blue) and after the first bunch passage (red) as computed by the code ECLOUD [82] for an LHC dipole is shown. It is evident the energy transfer from the beam to the electrons in the vacuum chamber, although a significant density of low energy electrons still exists.

The primary mechanism causing a build-up of electron cloud is beam induced multipacting. Here electrons accelerated by the electric field of the passing bunches hit the vacuum chamber wall with such an energy to produce, on average, more than one secondary electron per incident one. The number of secondary electrons depends on the SEY of the chamber material, which is a function of the primary electron energy, its angle of incidence, and the chamber surface composition and history. If the wall chamber SEY is larger than unity, the electron population grows rapidly in time with successive bunch passages, leading to a high electron cloud density.

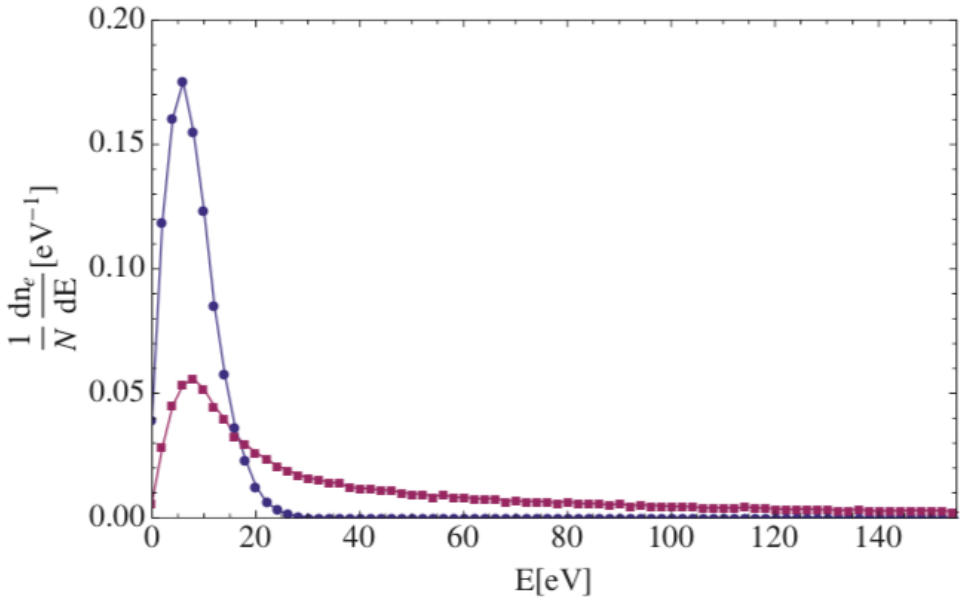

Figure 1.13: Photoelectron energy distribution at the moment of emission (blue) and after the first bunch passage (red) as computed by the code ECLOUD [82] for an LHC dipole [26].

The resonance condition to multipacting, in absence of magnetic field for a round chamber of radius b and short bunches of N_b particles, spaced by s_b, can be written as:

$$N_b r_e s_b = b^2. \tag{1.37}$$

If this condition is fulfilled, at every bunch passage not only new primary electrons will be created and accelerated to produce secondaries, but also all the secondaries produced by previous bunches will be accelerated by the beam leading to an exponential growth of the electron density. In general, if multipacting occurs the e^- cloud density grows exponentially until the equilibrium is reached under the influence of the space charge field of the cloud itself [26].

The electron density decays in the gap between bunch trains. Experimental observations show that such decay is much slower then expected and a sort of memory effect seems to occur [38, 57].

1.5.2 Secondary Electron Yield (SEY)

SEY measures the capability of a solid surface to produce secondary electrons, once it is irradiated by electrons of different primary energy, and it is commonly denoted by $\delta(E)$. The number of secondary electrons emitted in any particular event depends on the energy and angle of

incidence of the primary electron, as well as the properties of the surface. It is defined as the ratio of the number of electrons leaving the sample surface ($I_{out}(E)$) to the number of incident electrons ($I_{in}(E)$) per unit area:

$$\delta(E) = I_{out}(E)/I_{in}(E) = 1 - I_s(E)/I_{in}(E) \tag{1.38}$$

where $I_s(E)$ is the sample current.

Secondary electron emission can be described by a three-step process:

1. absorption of primary electrons and generation of secondary electrons,
2. transmission of the secondary electrons through the material,
3. escape of electrons over the vacuum barrier.

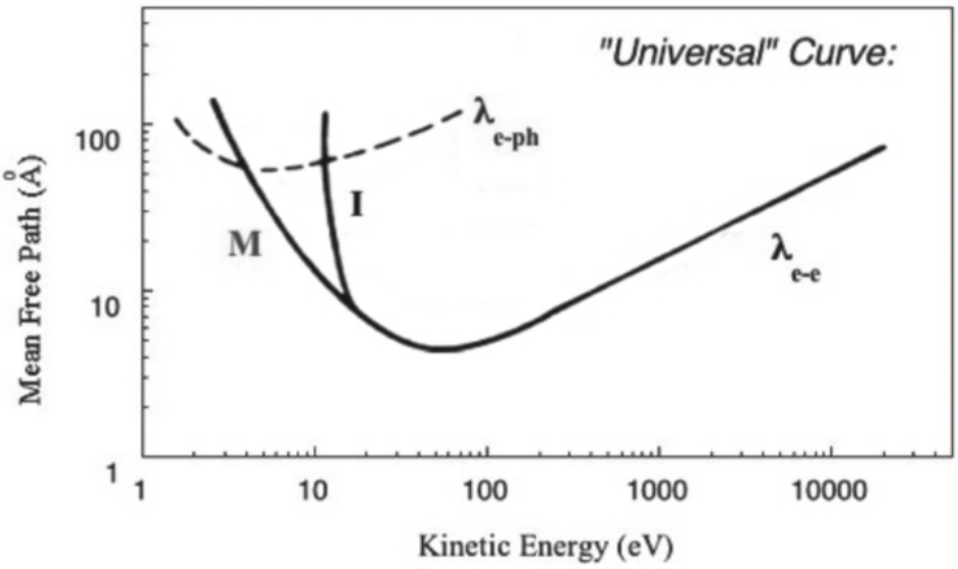

Figure 1.14: The "universal" curve (averaged over a wide range of materials) of the energy dependence of the escape depth of electrons in metallic (M) and insulating (I) solids for electron-electron (λ_{e-e}), and electron-phonon (λ_{e-ph}) scattering [37].

The first two steps are governed by the universal mean free path curve reported in fig. 1.14. Looking at this figure it is easy to believe how efficient the low energy electrons are in the production of secondary electrons. High energy electrons penetrate deeply in the solid and generate many internal electrons, nevertheless they will not able to escape in the vacuum chamber. On the contrary low energy electrons, in particular with energy between 10 eV an 1000 eV, penetrate only few monolayers. The secondaries are generated near the surface and the emission is easier.

In figure 1.14 we can recognise also the difference between metal and insulator: in metals, conduction electrons interact with secondary ones

(λ_{e-e} scattering) that lose energy. This effect reduces the number of the secondaries with enough energy to escape in the vacuum. In insulator this is not true. The wide band-gap present in insulators, prevents low energy secondary electrons from losing energy through electron-electron collisions. If the electron energy is below approximately twice the band-gap, the electron–phonon scattering (λ_{e-ph}) is dominant. This involves a larger mean free path and a large SEY value, i.e. the electrons reaching the vacuum barrier are more energetic than in metals and can overcome the vacuum barrier until insulator is electrically charged [26].

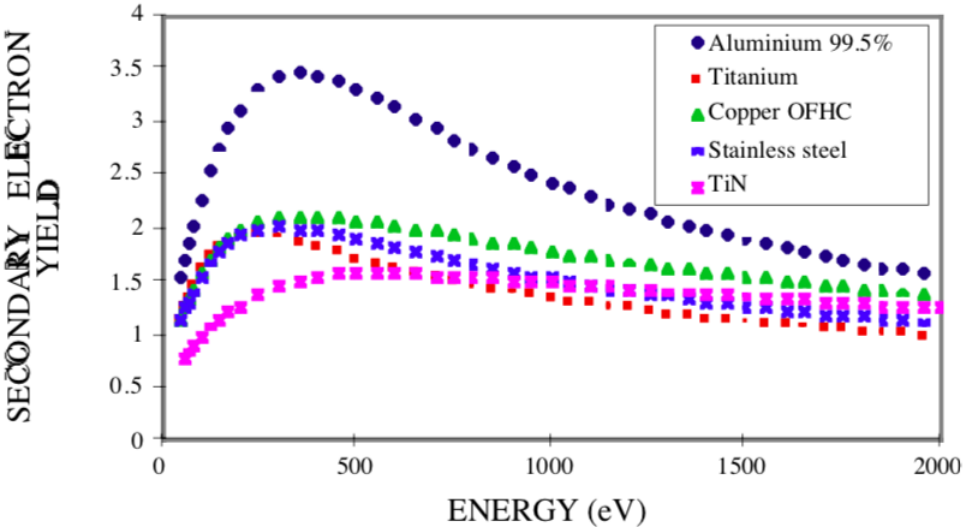

Figure 1.15: SEY measurements of various as received technical materials [14].

The escape process introduces an additional variable in δ because:

- metal work function can vary due to different crystal surface orientation and reconstruction,
- sub-monolayer gas adsorption on metals can significantly vary their work function,
- metals with different surface roughness have different work functions,
- surfaces of nominally the same material can show very different properties, depending on the history of the material.

There is, therefore, a difference between pure materials and technical materials. It is due to the presence of a surface layer (oxide and contaminants) which can be removed by an argon ion bombardment. Furthermore, the SEY of as received samples is significantly reduced, for instance, by baking under vacuum (e.g. to 300°C), a process leading mainly to the removal of the water vapour adsorbed on their surface [14].

For convenience, it is often quoted a single number for the SEY, which gives the maximum number of electrons emitted per incident electron under any conditions.

In figure 1.15 SEY measurements of various as received technical materials ar reported. The very high value of the Al technical sample is due to the insulating Aluminum-Oxide surface layer [45, 46](Al tends to oxidise in air much more promptly than the other typical accelerators surfaces). It is interesting to underline the very similar behaviour of SEY in Cu, Ti and St St, in particular at low energy. This can be explained as the effect of surface contaminant layer (as mentioned before, primary electrons with energy between 10 eV and 1000 eV can penetrate inside the material of $\sim$ 10 Å, so they are very sensible to surface contaminants). Also the value of TiN is affected by sample history, in [91], for example, the "as received" value is more similar to Cu, Ti and St St, so "as received" is not a well defined chemical state.

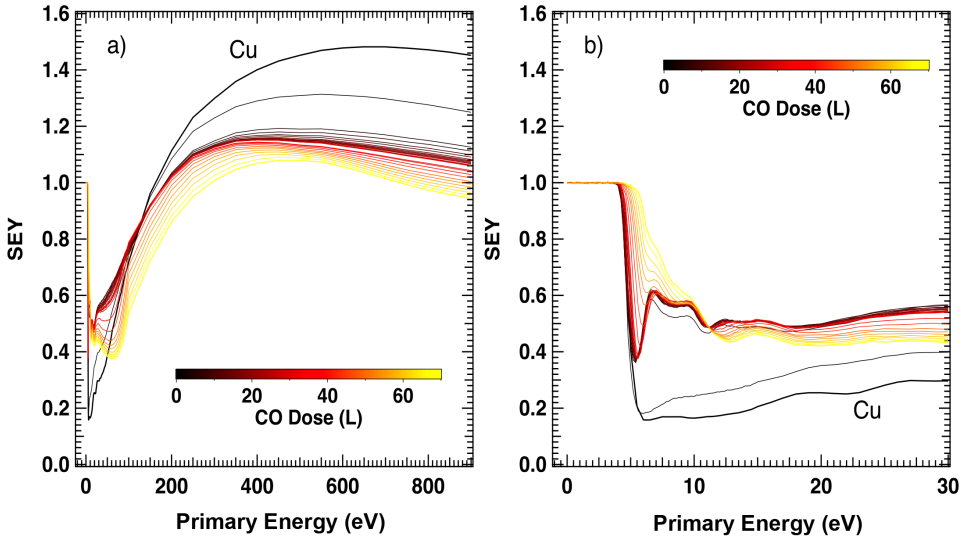

Figure 1.16: Cu SEY curves versus primary electrons energy as a function of the CO dose in the a) 0 ÷ 900 eV and b) 0 ÷30 eV ranges [8].

In cryogenic machines on the wall surface there will be some condensed gas layers that will influence the SEY. In fig. 1.16 we can see Cu SEY curves versus primary electrons energy as a function of the CO dose at high (0 ÷ 900 eV) and low energy (0 ÷30 eV) of primary impinging electrons. SEY, in the High-Energy range, gives important information about the formation of thick adsorbate layers and about the interaction of the primary beam with them. In the Low Energy range, the presence of characteristic peaks, at different energies, is a clear evidence of the adsorption of one or few gas layers on the substrate. These results show

how SEY measurements can be used to follow the adsorption process also at low coverages [8]. Value below 5 eV in fig. 1.16 are non-sense because

1.5.3 Effects on the beam

The presence of an electron-cloud may be responsible of collective effects as:

- electron stimulated desorption,
- emittance blow-up,
- incoherent tune shift,
- coupled-bunch and single-bunch instability.

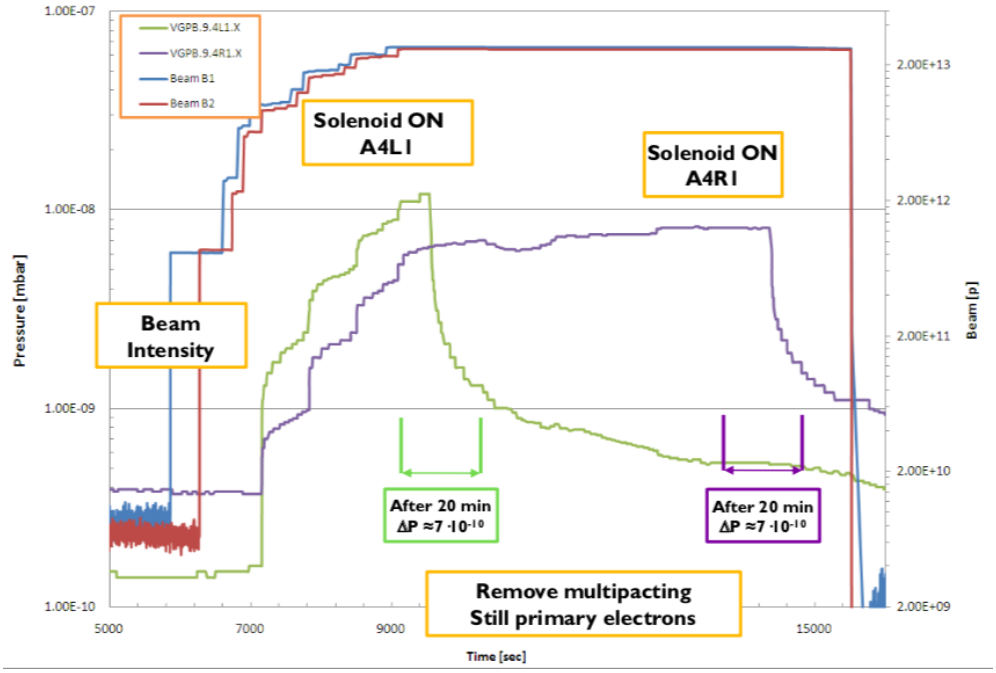

Figure 1.17: Observed pressure reduction when a solenoidal field of 20 Gauss is applied. Blue and red lines represent counter-circulating bunch population (right abscissa), green and purple are vacuum gauges readings (left abscissa) [22, 23].

An evidence of the electron cloud effect is the pressure increasing. The vacuum pressure readings (green and purple lines) during injection in LHC are reported in fig. 1.17. The data are acquired during LHC commissioning phase in October 2010. Solenoids with a magnetic field of ∼50 Gauss have been installed in all the cold warm transition of the LHC and are used during physic operation. Their role is to avoid multipacting in order to minimise the pressure increase stimulated by electron bombardments

by confining the secondary electrons close to the wall's surface. As shown in fig. 1.17, when the solenoids are not powered, a pressure increase is recorded when nominal LHC beam is present in the machine [22]. The use of a solenoid to mitigate ECE will be discussed below.

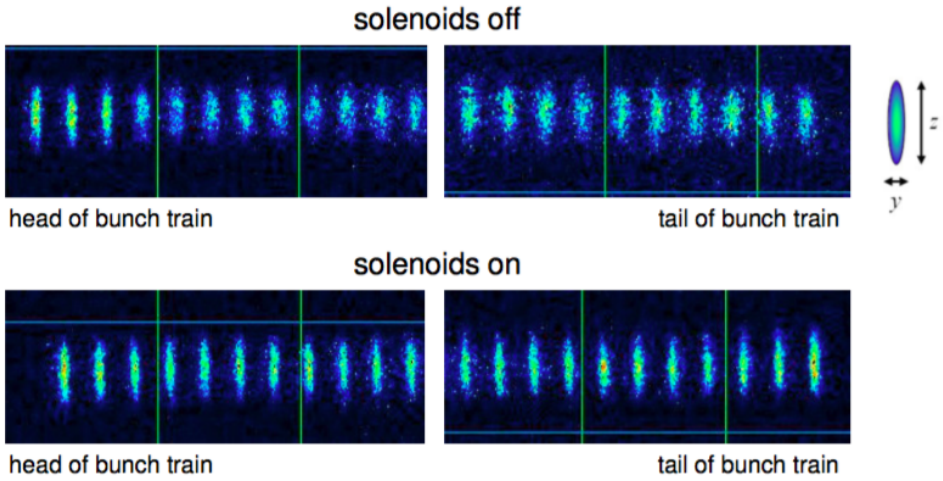

Figure 1.18: Bunch shape in head and tail part of the train taken by a streak camera in absence (on the top) and presence (on the bottom) of solenoidal field [39, 102].

Another evidence for the electron cloud effect was the beam size blow up, as shown in fig. 1.18. Bunch shape in head and tail part of the train are taken by a streak camera in absence (on the top) and presence (on the bottom) of solenoidal field. The vertical beam size starts to increase at the third or fourth bunch when the solenoids are powered off, while such an increase is not seen with the solenoid field on [39, 102]. ECE, increasing the beam size, increase the emittance of the beam, decreasing the luminosity.

The presence of an electron cloud generates an electric field acting on the positive charged beam as a focusing lens. Bunch-by-bunch tune shift increasing along the bunch trains is characteristic of the presence of an e^-cloud. This effect has been measured in all the machines affected by ECE. In fig. 1.19 a comparison of measured vertical tune shift and simulation (using POSINST) are shown[28, 35].

If the electron density around the beam exceeds a threshold value, the electron cloud causes a beam instability, called the electron cloud instability. In primis, in multibunch operation, the presence of EC can correlate the motion of the bunches with each other. Let's consider a bunch train and suppose that one of these passes through the cloud, not in its centre of symmetry. The interaction will induce an asymmetry in electron distribution. This perturbation will affects the following bunches.

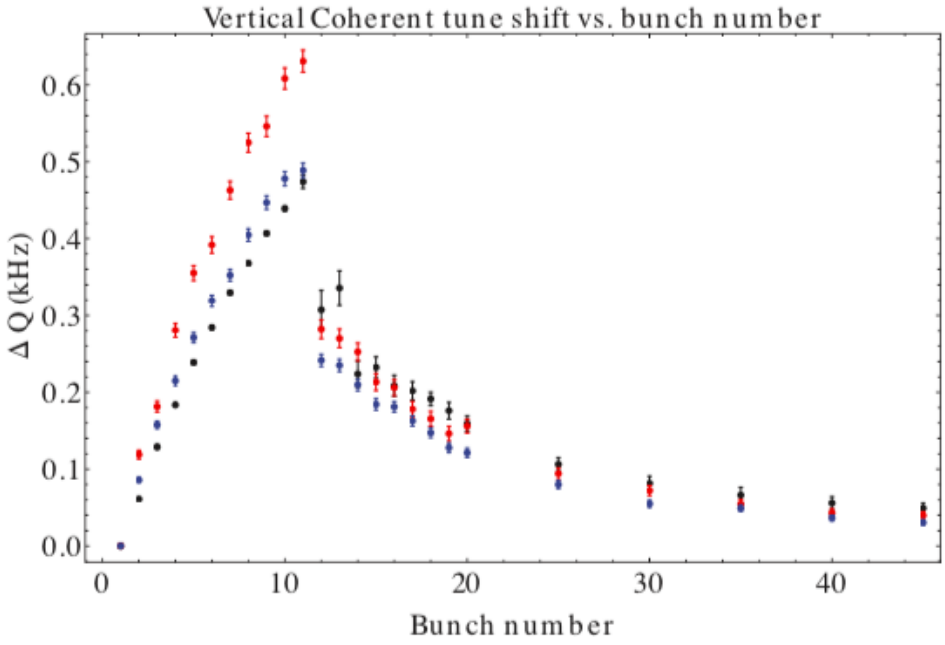

Figure 1.19: Measured vertical tune shift (black points) versus bunch number, for a train of 10 positron bunches, with 0.75 mA/bunch at 5.3 GeV spaced by 14 ns, followed by witness bunches at various spacings. Red points are computed (using POSINST) based on direct radiation and an ad hoc assumption about the scattered photons. Blue points, which are in better agreement with the data, are computed using results from Synrad3D as input to POSINST [28, 35].

The result will be an unwanted betatron oscillation of the bunch train (see fig. 1.20, left panel), resulting in a coupled bunch instability. Multibunch instabilities driven by an electron cloud were observed with positron beams at the KEK Photon Factory [55], at BEPC [48], at KEKB [95], at PEPII [40] and at DAΦNE [33] as well as with proton beams at the CERN SPS [9].

In secundis, a beam going through an electron cloud focuses the electrons, changing their density along the bunch thus inducing non-linear fields that can couple the motion of the head and tail of the bunch. If the bunch is perfectly centered on the pipe axis, the effect will be symmetrical and no coherent kick is generated along the bunch. If the head of the bunch is slightly displaced, an asymmetric perturbation will take place. After several turns (i.e. passages through the electron cloud), the perturbation in the head motion transfers to the bunch tail, and its amplitude may grow and lead to an unstable coherent motion of the whole bunch. This effect is shown in Fig. 1.20, right panel.

Depending on the cloud density [102], the instability could appear as a beam breakup with a rise time much shorter than the synchrotron

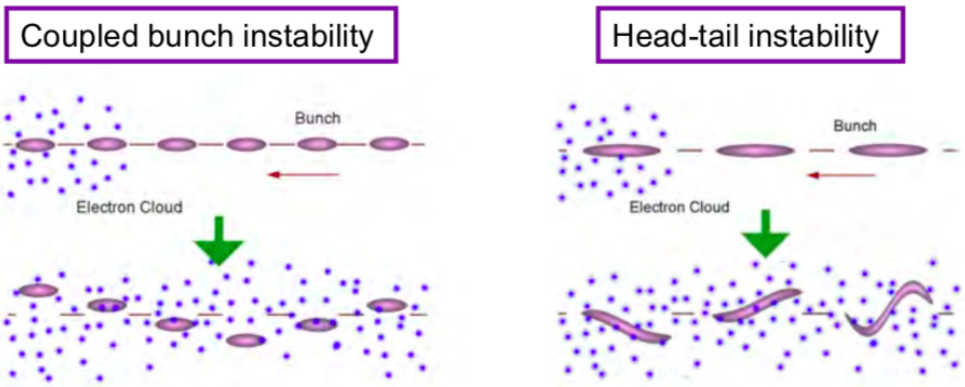

Figure 1.20: Artistic view of two types of electron cloud instabilities: coupled bunch (on the left) and single bunch (on the right) instability [90].

period ($\tau \ll T_s$), as a transverse mode coupling instability with a rise time comparable to the synchrotron period ($\tau \approx T_s$), or as a conventional head–tail instability, which typically has a slower growth rate ($\tau \gg T_s$) [26].

1.5.4 Mitigation strategies

Considering the importance of the problem, many countermeasures have been developed and adopted over time to reduce the effect of electron cloud. There are two ways to mitigate the ECE: passive countermeasures, which aim to the reduction of the surface parameters such as SEY and/or PY, and active countermeasures which introduce external electric or magnetic fields in order to reduce the e^- cloud formation.

The main techniques tested in several machines are:

i. beam pipe with antechambers,

ii. coating with low SEY materials,

iii. geometrical modification of the surface (grooved or laser treated),

iv. electron or photon scrubbing,

v. solenoidal fields,

vi. clearing electrodes.

i) In this case the beam pipe is designed in such way that SR irradiates the side wall of the antechamber, far from the beam. The photoelectrons do not interface with the beam [80, 92]. The antechamber structure is effective at low beam current. This solution is actually used in SuperKEKB (see fig. 1.21), where NEG strips to increase the pumping are inserted in the

antechamber. This solution is efficient also to reduce the SR heat load through use of absorber and it is, also, the design beam pipe of FCC-ee [15, 58]. In FCC-hh beam screen will be a sort of antechamber and will be discussed in the next chapter.

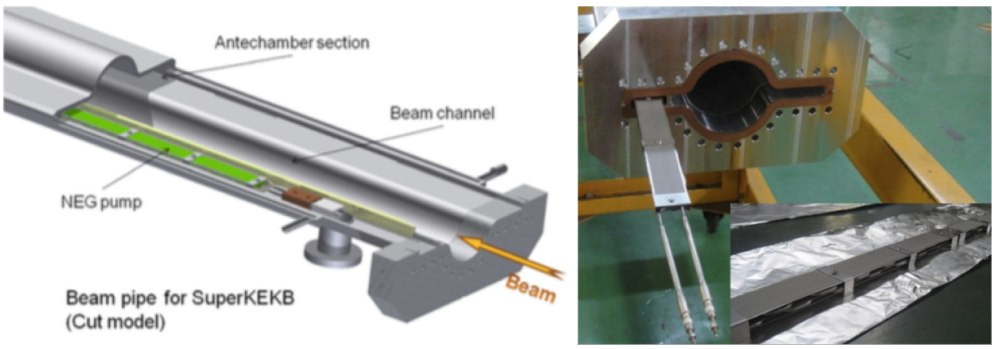

Figure 1.21: Schematic drawing of a beam pipe for the arc sections of the LER (low energy ring) in SuperKEKB (left panel). A picture of beam pipe with multilayered NEG (i.e. Non Evaporable Getters, like TiZrV) strips in inserted in the antechamber [92].

ii) Another approach is to coat the accelerator wall with a low SEY material, compatible with impedance requirements. In general the SEY of air exposed metals can be decreased by in-situ cleaning under vacuum, for instance by a vacuum chamber bake-out. Possible candidates of coatings are TiN, TiZrV NEG and a-C (i.e. amorphous Carbon). The NEG activation, i.e. applied heat treatment, involves the dissolution of the surface oxides into the bulk of the NEG materials. In fig.1.22 we can see how δ_{max} decreases with the increase of activation temperature [52]. However, it is not always possible to insert heaters to activate NEG (for example in cold magnets), and this material without this process shows an high SEY.

Another material with a low SEY is Carbon, in particular in crystalline HOPG (i.e. Highly oriented pyrolytic graphite. It is a highly pure and ordered form of synthetic graphite) and in its amorphous version [43, 63]. A temperature treatment is useful also in this case. In fig. 1.23 we can see δ_{max} decreasing with the increasing of annealing temperature.

iii) A very simple and effective solution is given by geometrical modification of surface. A surface with a grooved structure is found to have low SEY [59, 78, 79, 89, 100]. In fig. 1.24, two types of grooved surfaces are shown: triangular and rectangular grooves. The first ones are characterized by the angle α between continuous triangles, while the rectangular ones are characterized by the period b, dwell width a, depth h and a flat top thickness. An initial electron whose trajectory (see fig. 1.24 a) and b)), is shown in red hits the surface at point A and produces secondary

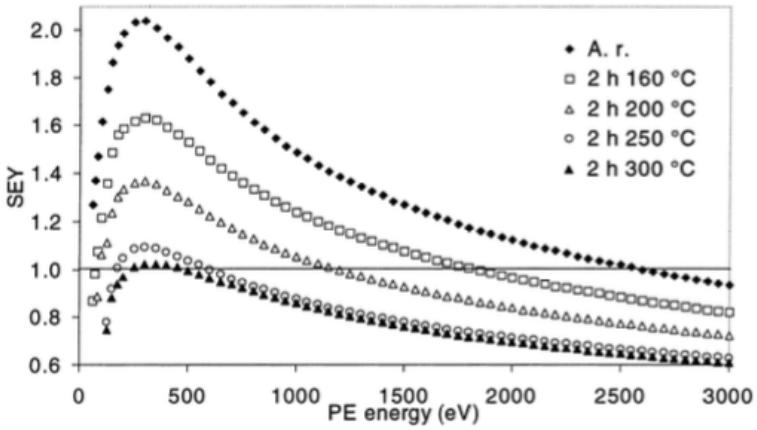

Figure 1.22: SEY versus primary electron energy (PE) energy of the TiZrV NEG coating; as received (A.r.) and after 2 h heating at 160 °C, 200 °C, 250 °C, 300 °C [26, 52].

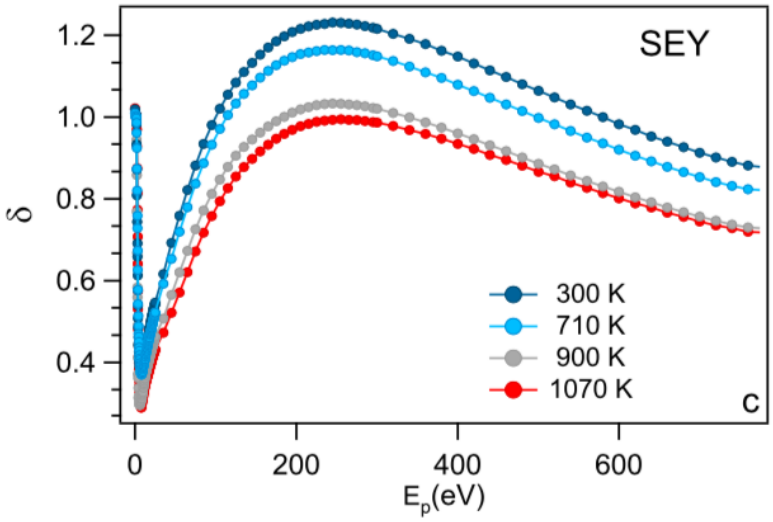

Figure 1.23: SEY curves measured on the C films as a function of the annealing temperature. [63].

electrons shown with blue lines.

Depending on the emission angle, some of the secondary electrons can escape the groove and move away from the surface. Other secondary electrons would hit an inner side of the groove. With some probability they will be absorbed, or they can generate further secondary electrons (which are second generation secondaries) whose trajectories are shown in green. The process may repeat several times until the energy of higher generations becomes too low and they are absorbed by the surface [79]. Panels (c) and (d) in fig. 1.24 show the experimental evidence of the SEY

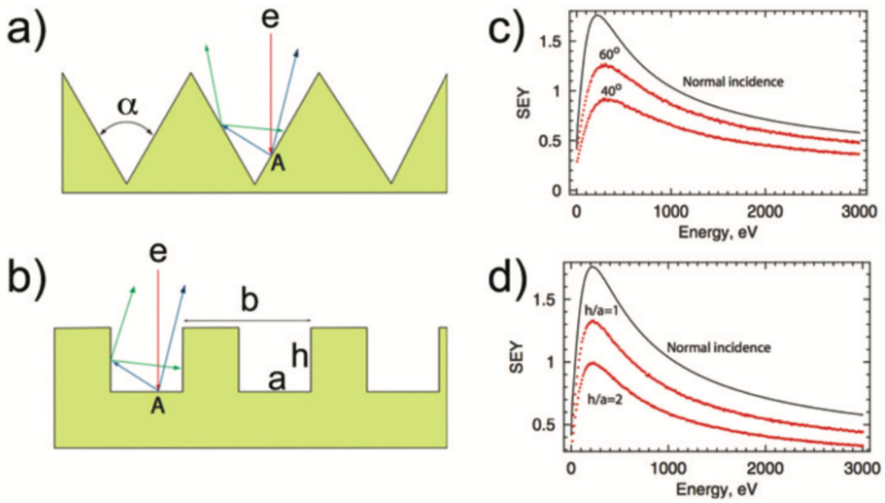

Figure 1.24: Triangular (a) and rectangular (b) grooves on the surface. Triangular grooves are characterized by the angle α. Rectangular grooves have a period b, width a and depth h. (c) Comparison of the effective SEY for α= 60° and 40° triangular grooves and the reference case of the flat surface and (d) SEY for rectangular grooves assuming a = 2/3b. Red dotted lines correspond to different aspect ratios of the rectangular grooves: the bottom line is for h/a = 2 and the middle one corresponds to h/a = 1. Full line corresponds to the reference case of the flat surface [28, 79, 89].

reduction obtained from a grooved surface for two different configuration of both grooved profiles. A Saw-Tooth structure is present also in LHC BS to reduce the SR Reflectivity and, consequently, secondaries. It will be described in the next chapter. Finally, it is important to underline that it is possible to realize also microscopic grooved surface with Laser Ablation Surface Engineering (LASE) technique that will be discuss in the next chapter.

iv) As said before it is observed that when a surface is exposed to an electron or photon beam, its SEY decreases. In fact, while the cloud is forming, the electron beam, hitting the accelerator walls, causes a reduction of their SEY value (see fig. 1.25). Such process is called *Scrubbing*.

The beneficial effect of electron beam scrubbing on these surfaces coincides with the formation of a graphitic surface film. Since the SEY of graphite and amorphous carbon is lower than that of air exposed metals, the presence of the a-C thin film reduces the effective SEY of the surface. Graphitic film growth occurs because, in general, technical surfaces are covered by C containing contaminants that, once exposed to the electron flux, tend to decompose and partly rearrange in graphitic assemblies [21, 26, 27, 71–73]. A similar mechanism is observed in presence of photon irradiation. In photon scrubbing the process is mediated by the low energy

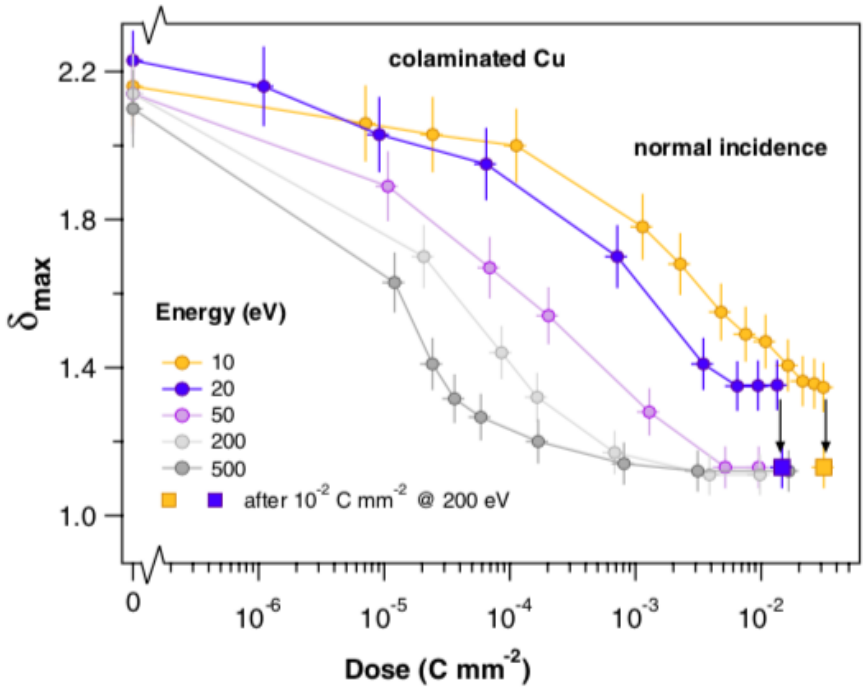

Figure 1.25: δ_{max} as a function of the dose for different impinging electron energies at normal incidence on colaminated Cu of the LHC beam screen. The squares represent the δ_{max} values measured after an additional electron dose of 1.0×10^{-2} Cmm^{-2} at 200 eV [27].

photoelectrons emitted by the surface (due to PY of material). For this reason the photon scrubbing could be less efficient than electrons [24].

v) An electrode in a beam pipe with a high positive potential attracts the electrons around the beam orbit. A drastic effect in reducing electron density is expected and has been confirmed in experiments. The requirement for the clearing electrode is to clear the electrons within one bunch spacing. Because of the beam's space-charge effect, clearing the electrons is more difficult in short bunched beam. Clearing electrodes are installed efficiently, for example, in positron ring arcs of DAΦNE (see fig. 1.26) [6].

vi) With a solenoidal magnetic field along the beam pipe, the electrons emitted from the surface return to the surface due to Larmor motion. Emitted photoelectrons or secondary electrons have an energy of several tens of electron volts. Hence, a magnetic field of several tens of Gauss is sufficient. If this process is fast enough, the solenoid of field can clear the electrons between two bunch passages. In fact, also in presence of the bunch potential, electrons still perform circle-like orbits and are maintained close to the chamber's wall. For a relativistic electron, the

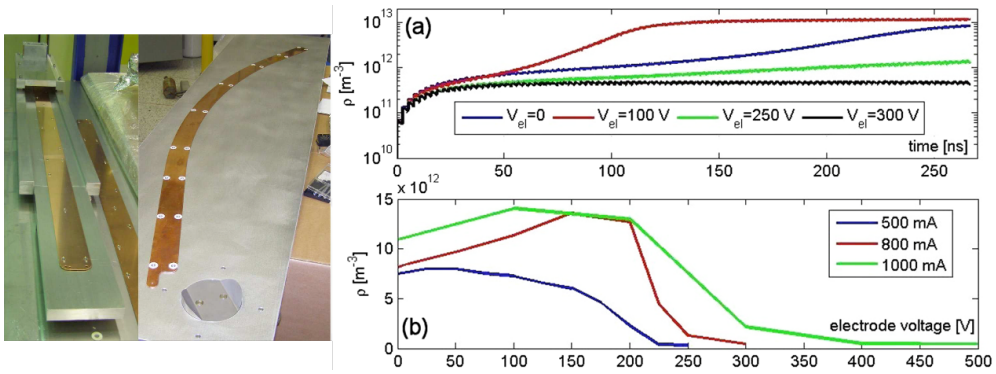

Figure 1.26: Images of the electrodes inserted in the wiggler and dipole chambers of the DAΦNE positron ring (left panel). (Right panel) (a) Evolution of the electron cloud density for different values of electrodes voltage, (b) e^- cloud density at the end of the bunch train [6, 26].

equation of motion can be written

$$\dot{\vec{v}} = -\vec{v} \times \frac{e\vec{B}}{\gamma mc} = \vec{\omega} \times \vec{v} \tag{1.39}$$

where $\vec{\omega} = e\vec{B}/(\gamma mc)$ is the cyclotron frequency of the electron. The solution of 1.39 is a helix parallel to $B_{solenoid}$ with radius $r = v_\perp/\omega$. The resonant magnetic field is given by

$$B_{res} = \frac{\pi m_e c}{s_b e} \tag{1.40}$$

where s_b is the bunch spacing. If this occurs, electrons hit the chamber wall in synchronism with the bunch passage and multipacting is enhanced [19, 26]. However there is a threshold value of bunch population, related to the energy gain of the electrons in the cloud during the passage of a bunch and independent of the bunch spacing.

In fig. 1.27 an example of solenoid field effect is shown. Here we can see electron orbits (top row), energy at the wall (middle row), and electron-cloud distribution (bottom row) with 0 G (left column) and 60G (right column) solenoid fields in a very long bunch case, i.e. the Spallation Nuclear Source's (SNS) accumulator drift region [99]. However, solenoids cannot be adopted in many parts of the ring not only where space constraints do not allow to wrap any coil around the chamber but also because in magnetic field regions, external solenoid fields are not effective in suppressing the build-up of the electron cloud. This make solenoids an effective countermeasure but not sufficient to guarantee total suppression of ECE [26].

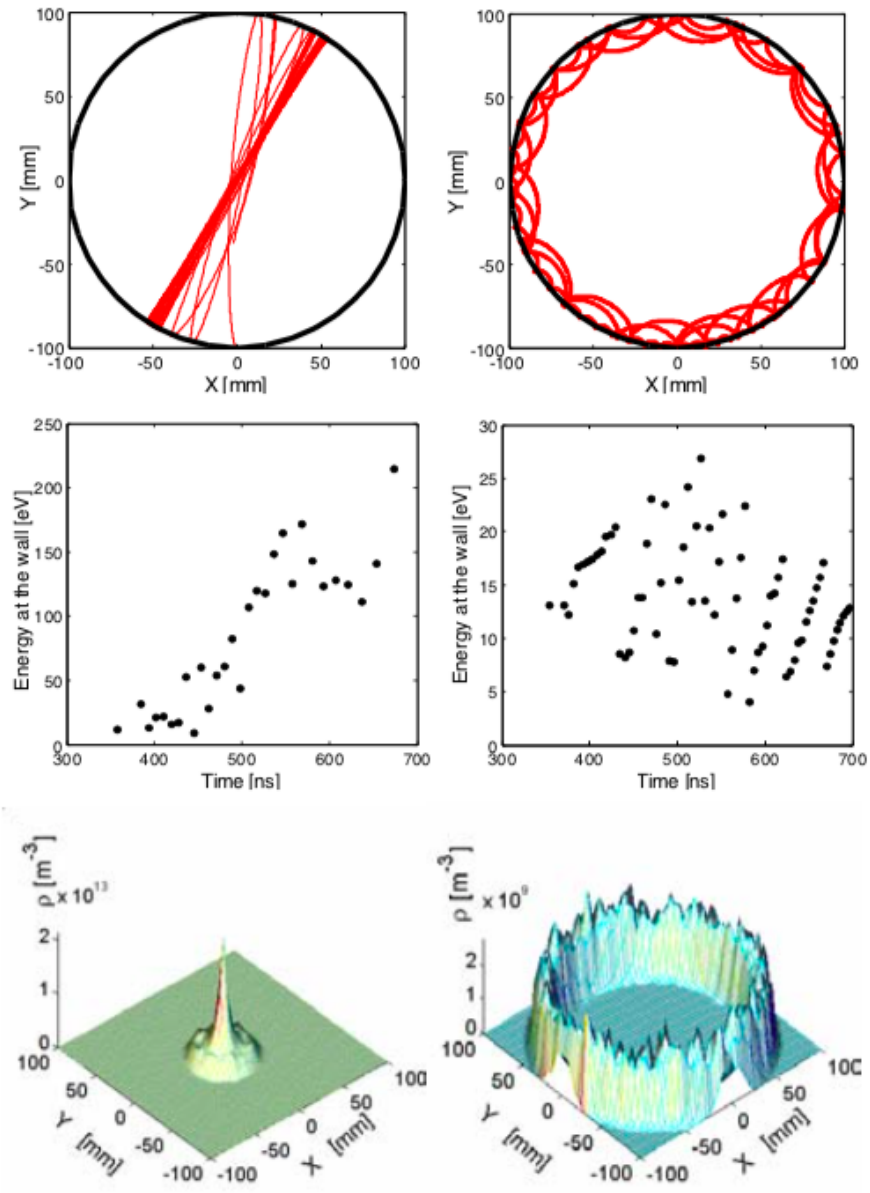

Figure 1.27: Electron orbit (top row), energy at the wall (middle row), and electron-cloud distribution (bottom row) with 0 G (left column) and 60G (right column) solenoid fields in the SNS's accumulator drift region [99].

1.6 State of art

In order to understand in detail the electron cloud effect and make reliable predictions for the future, detailed models of the e^-cloud formation in the different elements of the lattice are developed. One of these is the PyECLOUD simulation code [34, 54]. This model includes the main dipole and quadrupole magnets, shorter corrector magnets and drift spaces. To model the generation of photoelectrons in PyECLOUD build-up simulations some parameters are needed [34]:

- Y_i, Y_i^*: Photoelectrons Yields (per incident and absorbed photon, respectively) in the region of direct impact of the Synchrotron radiation;
- Y_r, Y_r^*: Photoelectron Yields in the remaining part of the chamber;
- R_i, R_r: Reflection rates in the region of direct SR impact and in the remaining part of the chamber, respectively;
- N_i, N_r: Photoelectrons emitted in the region of direct impact of the SR and in the remaining part of the chamber, respectively;
- N_t Total number of emitted photoelectrons;
- $n_\gamma(E > W_{Cu})$ Number of photons with an energy above the beam screen work function, emitted per proton and per m in the bending magnets.

		45 eV		194 eV	
Surface	Status	R (%)	Y* (e/ph)	R (%)	Y* (e/ph)
Cu co-lam.	as-received	80.9	0.114	77.0	0.318
	air baked	21.7	0.096	18.2	0.180
Cu elect.	as-received	5.0	0.084	6.9	0.078
Cu sawtooth	as-received	1.8	0.053	-	-
	150°C, 9h	1.3	0.053	1.2	0.052
	150°C, 24h	1.3	0.040	1.2	0.040

Figure 1.28: Forward scattering photon reflection R and photoelectron yields per absorbed photon, Y^*, of the studied materials under different surface conditioning, irradiated by 45eV and 194 eV critical energy Synchrotron Radiation [11].

Thus Reflectivity and Photo Yield are fundamental parameters that must be known to validate simulations. Experimental data about them concern mainly LHC beam screen (BS). The LHC BS was extensively studied with dedicated measurements between 1998 and 2012 [11, 13, 24, 67, 83]. The present section summarizes the main results of these studies that are relevant for the simulation of the electron cloud formation in the LHC arcs.

	45 eV		194 eV	
Dose (ph/m)	R (%)	Y* (e/ph)	R (%)	Y* (e/ph)
~ 2 10^{19}	8	0.029	7	0.040
1.5 10^{22}		0.015		0.022

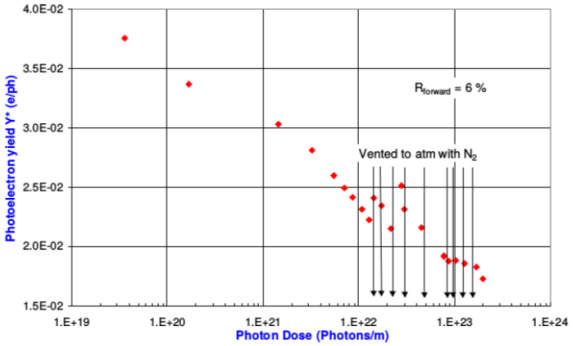

Figure 1.29: Photo Yield and forward scattered reflectivity of a copper colaminated material with a sawtooth structure at 45 and 194 eV as a function of dose (on the left); Photo Yield per adsorbed photon of a copper colaminated sleeve with a sawtooth structure submitted to synchrotron radiation with a critical energy of 194 eV at 11 mrad incidence versus photon dose [13].

In [11], the properties of several materials were studied using SR from the EPA ring at CERN, including co-laminated copper with and without a "macroscopic" sawtooth structure. In this case, in fact, the sample had not the LHC sawtooth structure but rather 0.5 mm step height and 10 mm periodicity, mounted such that the photons were incident quasi-normal to the vertical face of the sawtooth. It was possible to measure the reflectivity (only in the forward direction), as well as the Photo Yield, Y^*. The results of this paper are given in fig. 1.28. In this case the samples were irradiated by 45 eV and 194 eV critical energy Synchrotron Radiation, the incidence angle was $\theta_i = 11$ mrad, i.e. $\sim 0.6°$, with a beam divergence of ± 3.9 mrad.

In [13] the effect of photon-induced conditioning on the Photo Yield of co-laminated copper with sawtooth (LHC sawtooth) was quantified. Photon scrubbing with a dose of $1.5 \cdot 10^{22} ph/m$, corresponding to about 40 hours of nominal LHC operation, caused a decrease of the photoelectron yield by roughly 50% (see fig. 1.29).

The angular distribution of reflected photons is studied in detail in [67]. In this case SR from a bending magnet beamline at ELETTRA, Italy (BEAR) has been used to measure the Reflectivities (forward, backscattered and diffuse), for a flat and a saw-tooth structured Cu co-laminated surface using both white light SR, similar to the one emitted by LHC, and

monochromatic light, energy range between 8 eV and 200 eV. The main results are shown in fig. 1.30. The sawtooth structure was able to reduce the total reflectivity by over than 70%, in particular in forward direction.

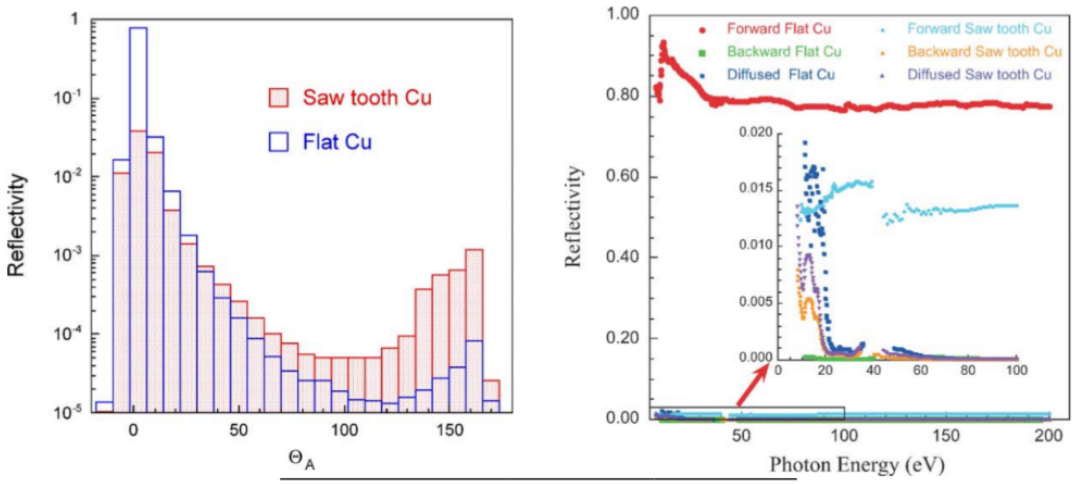

	Flat sample	Saw-tooth sample
Forward scattering (%)	80	4
Back scattering (%)	0	2
Diffused (%)	2	4
Total	82	10

Figure 1.30: Left: Measured reflectivity of Cu samples for different angles with incidence angle θ_i=26 mrad, i.e. $\sim 1.56°$. Right: Measured Reflectivities for different photon energies and material configurations. Bottom: Summary of Reflectivities for LHC-type photon spectrum. [67].

In [24] many aspects connected with photoemission properties relevant for accelerators are analysed. Among these there are the kinetic energy spectra of photoelectrons, the angular spectra of photoemission and the dependency of Photo Yield on photon energy. Furthermore, also the total Photo Yields and how these are affected by photon-induced conditioning is reported (see fig. 1.31). Measurements were performed at BESSY, Berlin. Several materials used for accelerator technology were studied including copper, although only without a sawtooth structure. Unlike in the previously mentioned measurement campaigns, the Reflectivity were not measured.

Sample	I_{sample} (μA)	I_{mirror} (μA)	Photon flux [photons/(s mm^2)]	PY (electrons/photon)
Au	3.72	3.59	5.6×10^{14}	0.041 ± 0.010
Cu	3.8	2.4	3.8×10^{14}	0.063 ± 0.010
Cu-ab.	1.94	0.83	1.5×10^{14}	0.093 ± 0.010
TiN	8.3	4.2	6.5×10^{14}	0.080 ± 0.010
TiZr	2.4	1.1	1.7×10^{14}	0.088 ± 0.010
TiZr II	1.6	0.76	1.2×10^{14}	0.084 ± 0.010
Cu-el.	1.5	0.88	1.4×10^{14}	0.070 ± 0.010
Pd	0.87	0.48	7.5×10^{13}	0.072 ± 0.010
St 707	4.9	3.6	5.7×10^{14}	0.053 ± 0.010
Al	9.0	3.45	5.4×10^{14}	0.106 ± 0.010

Figure 1.31: The PY per incident photon for the different as-received samples studied. In the second and third columns the sample drain currents and the last refocusing mirror drain currents are reported, respectively. In the fourth column the estimated photon flux is given for details. In the last column the PY is reported with its absolute error. [24]

Finally, in [83] we can find Reflectivity and Photo Yield (see fig.1.32) measurements as functions of Photon energy. The investigated energy range presented here is between 130 eV and 1600 eV and the measurements are performed at BESSY II. The most grazing incident angle was 1.5°. Here we can see the presence of air contaminants on the surface, in particular Oxygen and Carbon. These effects will be discussed more in details in the next chapters.

The main evidence of this experimental excursus is the lack of data at high energy (except for the last case) and at grazing angles. The aim of this Ph.D work is to provide a comprehensive systematic dataset useful for the accelerator community, in particular for e^-cloud effect simulations.

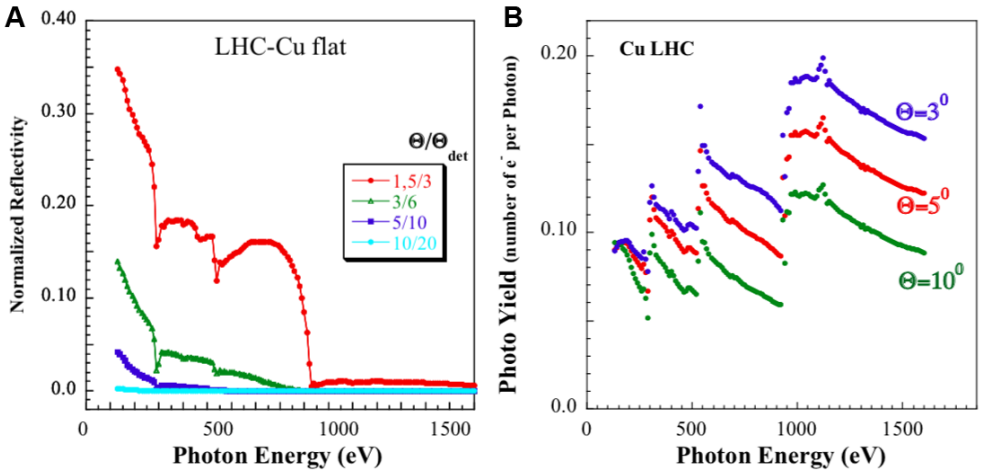

Figure 1.32: Reflectivity (panel A) and Photo yield (panel B) of LHC-Cu sample representative of the flat part of the beam screen, as function of photon energy for various incidence angles θ and emission angle θ_{det} [83].

Chapter 2

Reflectivity, Photo Yield and Surface treatments

X-Ray Reflectivity and, consequently, absorption depend on a limited number of parameters:

- Photon energy and light polarization,
- Angle of incidence,
- Surface roughness,
- Material

In the previous chapter we have seen the main problems related to the production of synchrotron radiation in accelerators. In this chapter we will see in more detail the importance of an experimental study of reflectivity and PY of technical surfaces.

2.1 Photon Matter Interaction

In general, an electromagnetic wave is described in a convenient coordinate system by its amplitude $E_{s,p}$ and its phase $\phi_{s,p}$:

$$E_{s,p}(\vec{r},t) = E^0_{s,p} e^{i\omega t - \vec{k}\cdot\vec{r} - \phi_{s,p}} \tag{2.1}$$

where: r and t are position and time, s and p are referred to light polarization[1], ω is the frequency and $\vec{k}$ is wave vector. The average intensity associated to this wave is:

$$I_0 = \frac{|E^0|^2}{2Z} \tag{2.2}$$

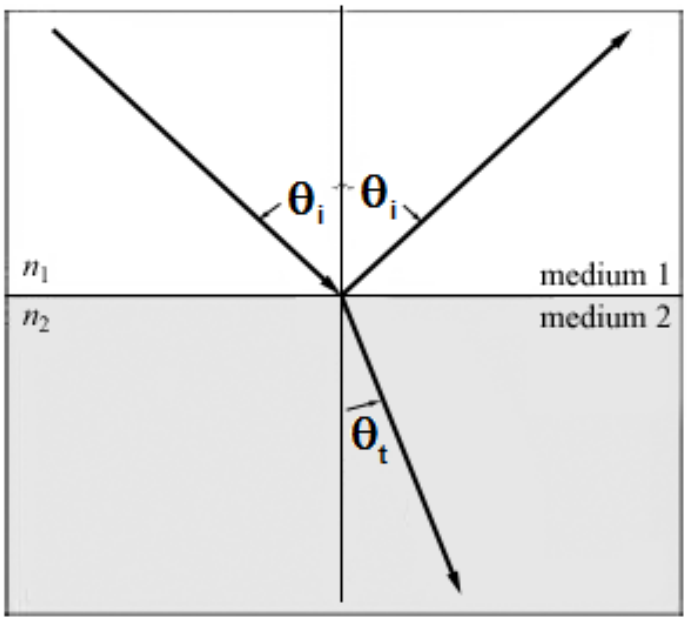

Figure 2.1: Reflection and refraction of light at the interface between two media of different refractive indices, with $n_2 > n_1$. Since the velocity is lower in the second medium ($v_2 < v_1$), the angle of refraction θ_2 is less than the angle of incidence θ_1; that is, the ray in the higher-index medium is closer to the normal.

where $Z = \sqrt{\mu/\varepsilon}$ is the characteristic impedance of the mean. At the boundary of two media, described by the refractive index n_1 and n_2, the incident wave is split into a reflected and a refracted wave (see fig. 2.1).

We call the fraction of the incident power that is reflected from the interface the reflectance (or *reflectivity*, or power reflection coefficient R, and the fraction that is refracted into the second medium is called the transmittance (or *transmissivity*, or power transmission coefficient) T. Note that these are what would be measured right at each side of an interface and do not account for attenuation of a wave in an absorbing medium following transmission or reflection [49].

The reflectance for s-polarized light is

$$R_{\mathrm{s}} = \left| \frac{Z_2 \cos\theta_{\mathrm{i}} - Z_1 \cos\theta_{\mathrm{t}}}{Z_2 \cos\theta_{\mathrm{i}} + Z_1 \cos\theta_{\mathrm{t}}} \right|^2 , \tag{2.3}$$

while the reflectance for p-polarized light is

$$R_{\mathrm{p}} = \left| \frac{Z_2 \cos\theta_{\mathrm{t}} - Z_1 \cos\theta_{\mathrm{i}}}{Z_2 \cos\theta_{\mathrm{t}} + Z_1 \cos\theta_{\mathrm{i}}} \right|^2 , \tag{2.4}$$

where Z_1 and Z_2 are the wave impedances of media 1 and 2, respectively.

[1] P-polarized light is parallel to the plane of incidence, instead S-polarized light has polarization perpendicular to the plane of incidence.

We assume that the media are non-magnetic (i.e. $\mu_1 = \mu_2 = \mu_0$), which is typically a good approximation at optical frequencies (and for transparent media at other frequencies). Then the wave impedances are determined solely by the refractive indices n_1 and n_2:

$$Z_i = \frac{Z_0}{n_i} \tag{2.5}$$

where Z_0 is the impedance of free space and $i = 1, 2$. Making this substitution, we obtain equations using the refractive indices:

$$R_\mathrm{s} = \left| \frac{n_1 \cos\theta_\mathrm{i} - n_2 \cos\theta_\mathrm{t}}{n_1 \cos\theta_\mathrm{i} + n_2 \cos\theta_\mathrm{t}} \right|^2, \tag{2.6}$$

$$R_\mathrm{p} = \left| \frac{n_1 \cos\theta_\mathrm{t} - n_2 \cos\theta_\mathrm{i}}{n_1 \cos\theta_\mathrm{t} + n_2 \cos\theta_\mathrm{i}} \right|^2. \tag{2.7}$$

As a consequence of conservation of energy, one can find the transmitted power simply as the portion of the incident power that is not reflected:

$$T_\mathrm{s} = 1 - R_\mathrm{s} \tag{2.8}$$

and

$$T_\mathrm{p} = 1 - R_\mathrm{p} \tag{2.9}$$

the reflection coefficient r is the ratio of the reflected wave's complex electric field amplitude to that of the incident wave. The transmission coefficient t is the ratio of the transmitted wave's electric field amplitude to that of the incident wave.

The reflected and transmitted power can be written as:

$$R_{s,p} = |r_{s,p}|^2 \qquad T_{s,p} = |t_{s,p}|^2 \tag{2.10}$$

where the reflection coefficient $r_{s,p}$ is the ratio of the reflected wave's complex electric field amplitude to that of the incident wave. The transmission coefficient $t_{s,p}$ is the ratio of the transmitted wave's electric field amplitude to that of the incident wave.

Combing equations 2.6, 2.7, 2.8 and 2.9 we can write [17]:

$$\begin{aligned}
r_\mathrm{s} &= \frac{n_1 \cos\theta_\mathrm{i} - n_2 \cos\theta_\mathrm{t}}{n_1 \cos\theta_\mathrm{i} + n_2 \cos\theta_\mathrm{t}}, \\
t_\mathrm{s} &= \frac{2 n_1 \cos\theta_\mathrm{i}}{n_1 \cos\theta_\mathrm{i} + n_2 \cos\theta_\mathrm{t}}, \\
r_\mathrm{p} &= \frac{n_2 \cos\theta_\mathrm{i} - n_1 \cos\theta_\mathrm{t}}{n_2 \cos\theta_\mathrm{i} + n_1 \cos\theta_\mathrm{t}}, \\
t_\mathrm{p} &= \frac{2 n_1 \cos\theta_\mathrm{i}}{n_2 \cos\theta_\mathrm{i} + n_1 \cos\theta_\mathrm{t}}.
\end{aligned} \tag{2.11}$$

Until now we have neglected the electromagnetic wave attenuation when it passes trough a medium. This can be conveniently taken into account by defining a complex refractive index:

$$\tilde{n} = n + ik$$

. For X-ray and extreme ultraviolet radiation the complex refractive index deviates only slightly from unity and usually has a real part smaller than 1. It is wavelength dependent and it is normally written as:

$$n(\lambda) = 1 - \delta - ik \tag{2.12}$$

Here, the real part δ is the refractive index and indicates the phase velocity, while the imaginary part k is called the extinction coefficient and indicates the amount of attenuation when the electromagnetic wave propagates through the material.

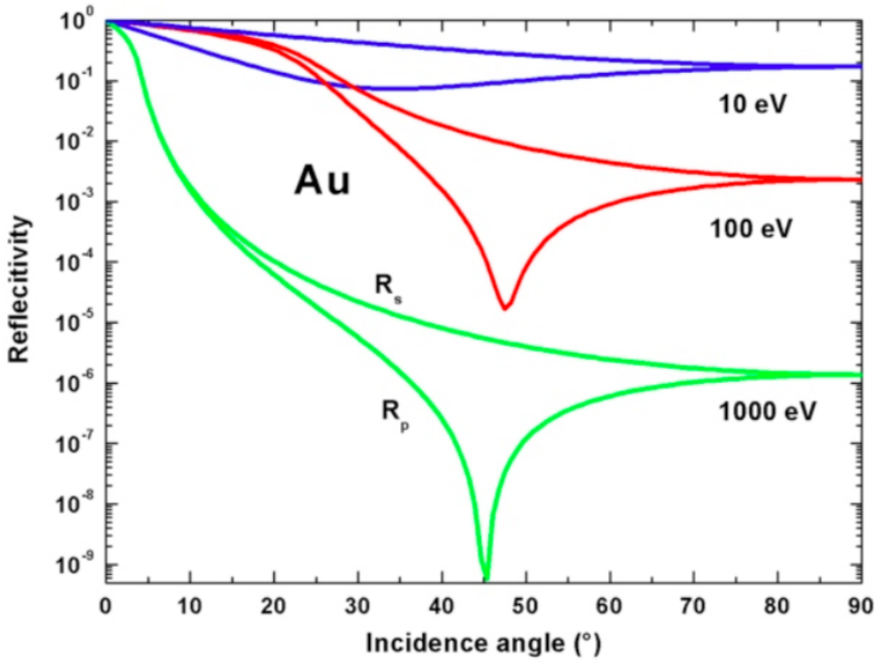

Figure 2.2: REFLEC simulation of reflectivity R_s and R_p of a perfect Au-coating as function of incidence angle in the UV and soft X-ray range [83].

The values of complex refractive index are tabulated for the whole electromagnetic range [30, 50, 51, 77]. It is, therefore, possible to evaluate the reflectivity of a material by combining these parameters. The optical constants, from the visible to the X-ray range, are incorporated in open access reflectivity programs such as REFLEC [83, 84].

An example of reflectivity calculation done with REFLEC is shown in fig. 2.2 Reflectivity of a ideal Au-surface at three photon energies of 10 eV ,

100 eV and 1000 eV is plotted for both reflectivity components R_s and R_p. At small angles, in the total external reflection regime, all light is reflected. Note that R_s decreases gradually, while R_p goes through a Brewster minimum, which is at around 45° in the x-ray range ($\theta_B = \arctan(1/n)$). Significant normal incidence reflectivity ($\theta_i = 90°$) is available only in the visible and the UV spectral range. This is the case for all materials [83].

2.2 Roughness: from mirrors to accelerator walls

All the discussion done until now is valid for ideal mirror. In real surfaces and, in particular, in accelerator walls there are further components to consider. Let's consider the surface to be composed of individual facets, with each surface normal having an individual angle $\Delta\alpha_i$ with respect to the mean surface plane. Parallel incident beams will then be deflected by $2 \cdot \Delta\alpha_i$ (see fig. 2.3). The rms-value of the angular distribution of the surface facets $\Delta\alpha_i$, assuming a Gaussian probability distribution of the facets orientation, is usually called the *slope error* of the surface. The slope errors gives rise to a blurring of the reflected beam, distortion of wave-front and in general this effect influences the imaging properties, but without significant reduction of intensity. In this case the facets have a much larger size than the wavelength.

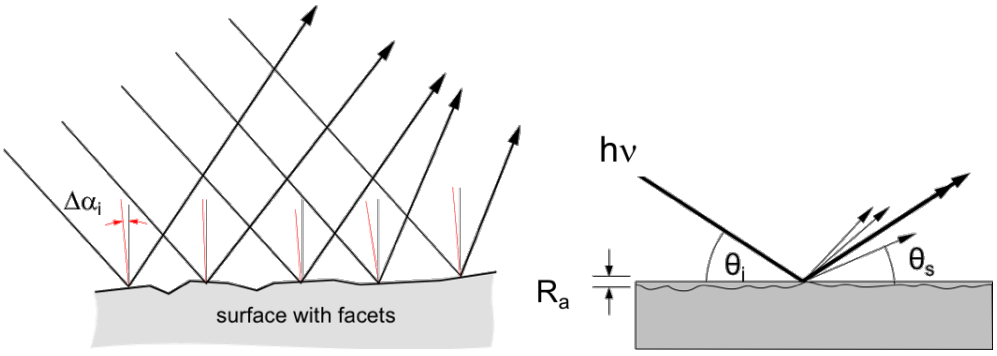

Figure 2.3: Slope error (left panel) and surface roughness (right panel) [83].

Surface roughness R_a causes a reduction of the intensity specular (Fresnel like) reflectivity R_0 and scattering. In this case surface roughness is characterized by a typical dimension comparable to wavelength. The correction to R_0 is given by a Debye-Waller factor according to:

$$R = R_0 e^{-\left(\frac{4\pi R_a \sin\theta_i}{\lambda}\right)^2} \tag{2.13}$$

the surface roughness R_a can be interpreted as the rms-value of the height deviation, λ is the wavelength. The impact on the optical properties depends strongly on the frequency. Long wavelengths are more sensitive to

slope error, while small wavelengths are roughness dominated. Obviously the concepts of slope error of a surface and roughness can be regarded as one and the same [83, 85].

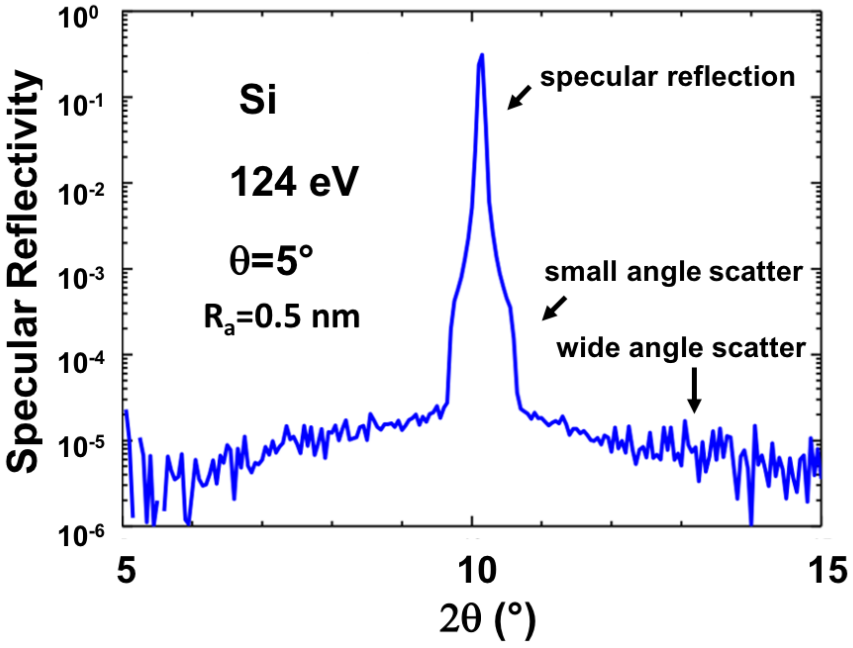

Figure 2.4: Scattering from a quasi-perfect Si mirror surface taken at 5° incidence angle and at 124 eV (10 nm). Data taken with a 4×4mm^2 photodiode masked by a 0.25 mm pinhole [83].

The surface roughness can be measured using an interferometric microscope or atomic force microscope (AFM). To inspect the slope error, a different measuring technique is used: interferometry or various types of surface profilers [85].

To understand the effect of roughness in reflectivity let's consider data reported in fig. 2.4 and fig. 2.5. In the first case we can see how in a quasi-mirror of Silicon (R_a is 0.5 nm) the reflected signal is included, for many orders of magnitude (we are using a logarithmic scale), in a limited angular width, it is, therefore, possible to distinguish specular component by small and wide angle scattering. This sharpness in the Specular REflectivity is immediately lost when we study technical surfaces, which are far to be af optical quality.

The angular distribution of Reflectivity as a function of reflection angle of LHC BS flat zone is reported in fig. 2.5. In this case the roughness is 30 times higher than Si mirror and it is hard to separate scattering components by specular (Fresnel like) reflectivity. This is true even for the best surface, with minimal roughness and slope error. This is the

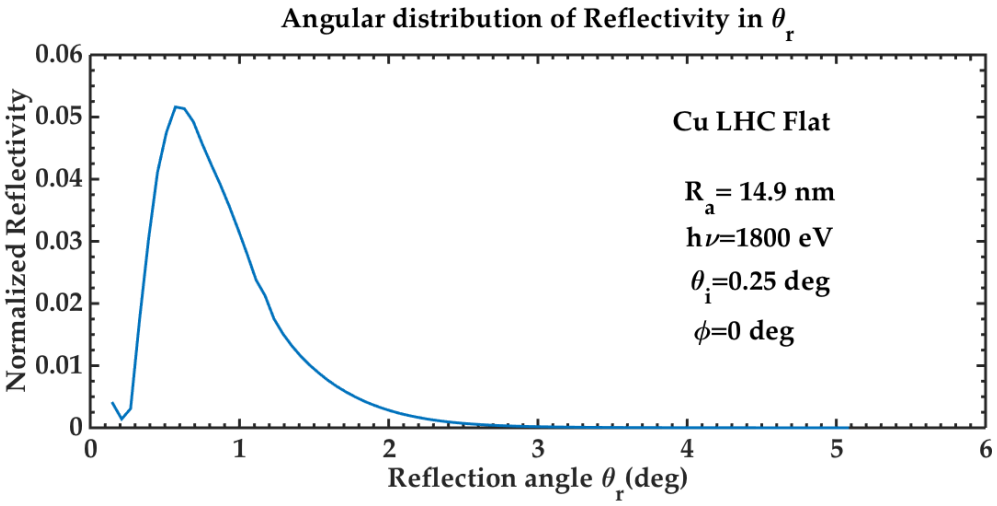

Figure 2.5: Angular distribution of Reflectivity as a function of reflection angle of LHC BS flat zone at 0.25° incidence angle and at 1800 eV (0.69 nm). Data acquired with a 4×4mm photodiode masked by a 0.1 mm of aperture slit.

reason why we, as will be described in the next chapter, artificially define as Specular Reflectivity all the light entering in the used photodiode, once it is centred at the geometrical reflection position.

It is important to underline that in simple simulations calculated by tabulated data, as REFLEC, the roughness is just an attenuation parameter of reflected intensity component (Debye-Waller factor, in REFLEC integrated with the Nevot-Croce formalism [70]). In real life scattering occurs and this means that in the vacuum chamber will be more light than we will expect.

2.3 Heat Load and Carbon coating

In the previous section we have seen the dependence of reflectivity by incidence angle, photon energy, light polarization and surface roughness. We did not yet talk about material dependence.

For each material there are absorption thresholds due to its atomic structure and electronic configuration. An absorption edge, i.e. a discontinuity in the absorption spectrum of a substance, occurs at wavelengths where the energy of an absorbed photon corresponds to an electronic transition or ionization potential. When the energy of the incident radiation becomes smaller than the work required to eject an electron from one or other quantum states in the constituent absorbing atom, the incident radiation ceases to be absorbed by that state. Obviously the reflectivity of a material increases moving away from such thresholds.

In fig 2.6 we can see calculated specular reflectivity at fixed roughness

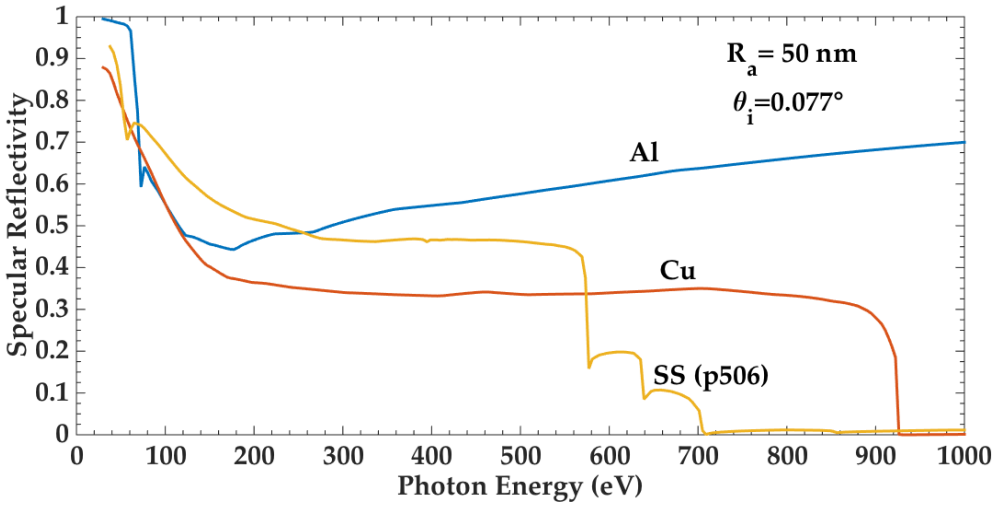

Figure 2.6: Reflectivity calculation at 0.077°(1.35 mrad) angle of incidence and R_a= 50 nm for typical technical bulk materials.

(R_a= 50 nm, a reasonable value for technical surfaces) and incidence angle (θ_i is FCC-hh incidence angle) for three typical technical bulk materials, such as aluminium, copper and stainless steel. We can see all the drops are due to the existence of absorption edges in materials.

In correspondence of absorption edges a higher number of photoelectrons are generated and photo yield (PY) presents peaks (see chapter 4).

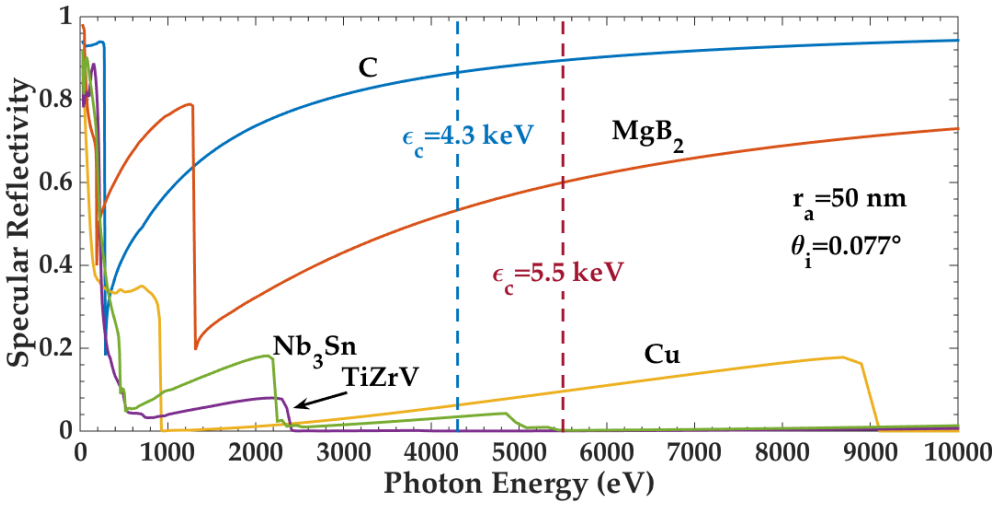

Figure 2.7: Reflectivity calculation at 0.077°(1.35 mrad) angle of incidence and R_a= 50 nm for different materials in the photon energy range of interest [25].

In sections 1.2 and 1.3 we have seen how crucial the problem of heat load in FCC is. Greater absorption, and therefore less reflectivity, leads

to a greater heat load. The value and position of absorption edge depends on material atomic structure and composition. So ideally if you want to obtain a high reflectivity in X-ray regime you should find a material which has no absorption energy in the same range. This is the Carbon case, how we can see in fig. 2.7.

The materials used to calculate the reflectivity are all potential candidates to be the final surface of the Beam Screen. Cu and TiZrV are the final coatings used in LHC, while Nb_3Sn and MgB_2 are part of a superconductor coatings family which could be used in FCC-hh to reduce detrimental impedance effects. It can be clearly observed that, even at very grazing angles, the reflectivity is very poor in the X-ray energy range due to the presence of adsorption edges with the exception of carbon. Because of the absence, above its C 1s edge at around 280 eV, of deeper absorption edges, the reflectivity of C is extremely high even for the roughness proposed in the calculation reported in fig. 2.7 [25]. It is, therefore, possible to evaluate the idea of exploiting the high reflectivity of carbon to shift the high heat load carried by Synchrotron Radiation from colder areas (ie superconducting magnets) to warmer areas of the machine. In this way it is possible to reduce the enormous quantity of power at the plug necessary for the cooling system (see 1.3). In order to calculate the minimum amount of Carbon necessary as coating , it is necessary to evaluate the attenuation depth in the radiation energy range of interest. The attenuation length, or absorption length, is the distance λ into a material when the probability has dropped to $1/e$ that a particle has not been absorbed. Alternatively, if there is a beam of particles incident on the material, the attenuation length is the distance where the intensity of the beam has dropped to 1/e, or about 63 % of the particles have been stopped.

Mathematically, the probability of finding a particle at depth x into the material is calculated by Beer-Lambert law:

$$P(x) = \frac{1}{\lambda} e^{-x/\lambda}. \tag{2.14}$$

In general λ is material and energy dependent. If we calculate the attenuation depth of the X-ray at the incidence angle of FCC we find out that $\lambda(C) \sim 3.5$ nm in X-ray range, so 20 nm of Carbon are enough to reflect all photons at such grazing angle. So it is possible to think of solutions with accommodating impedance issues.

2.4 FCC-hh Beam screen

The latest FCC-hh beam screen cross section design can be seen in fig. 2.8, where the chamber layout and surface treatments have been

highlighted.

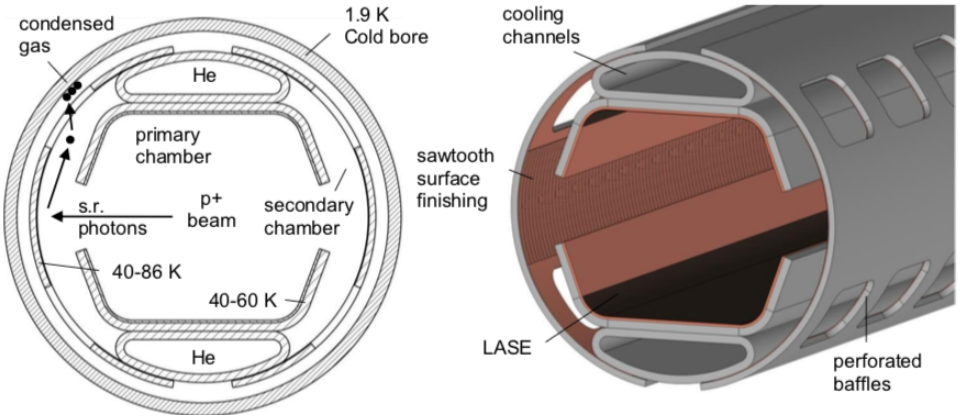

Figure 2.8: FCC-hh beam screen aimed for bending magnets, showing the LASE treatment of the upper and lower flat areas of the inner chamber [75].

The beam screen has been divided in two chambers, being the most characteristic feature of this new design. The inner chamber, where the proton beam circulates, has a 0.3 mm thick Cu co-lamination. It is kept cold by being in direct contact with the cooling channel and without receiving direct heat load from the SR [41, 76].

The secondary chamber surface is modulated with a sawtooth profile, similar to LHC BS. The aim is to minimize the amount of reflected radiation. Higher SR absorption corresponds the lower e-cloud density (see sec. 1.5) and lower outgassing due to the photon stimulated desorption (see sec. 1.4) because SR is concentrated in areas already conditioned. A 0.1 mm thick Cu layer has been chosen for the secondary chamber, also to provide enough thermal conductivity in the BS in order to transfer the SR power to the cooling tubes. The LHC's sawtooth geometry(see 2.5) must be adapted for the new collider parameters.

In order to mitigate SEY and then the e-cloud build-up, the laser treated (LASE, made by the Science & Technology Facility Council (STFC), see 2.6) copper has been at the moment chosen because of the possibility of applying it directly in the series manufacturing under atmospheric pressure and for its very low SEY values. LASE presents, however, poor properties regarding surface impedance, due also to the high surface aspect ratio left by the treatment [75]. There is, also, evidence that may suggest a critical dependence of vacuum stability on surface morphology (in particular in such characteristic structures like LASE), gas species and dose, thus requiring further investigation [88].

2.5 LHC Saw-tooth

As said before, the LHC provides two counter-circulating proton beams with colliding energies of 14 TeV in the centre of mass, requiring superconducting bending magnets operating in super-fluid helium at 1.9 K. The LHC dipoles have the functions to bend the particles on quasi-circular paths around the 27 km vacuum channels (see fig. 2.9).

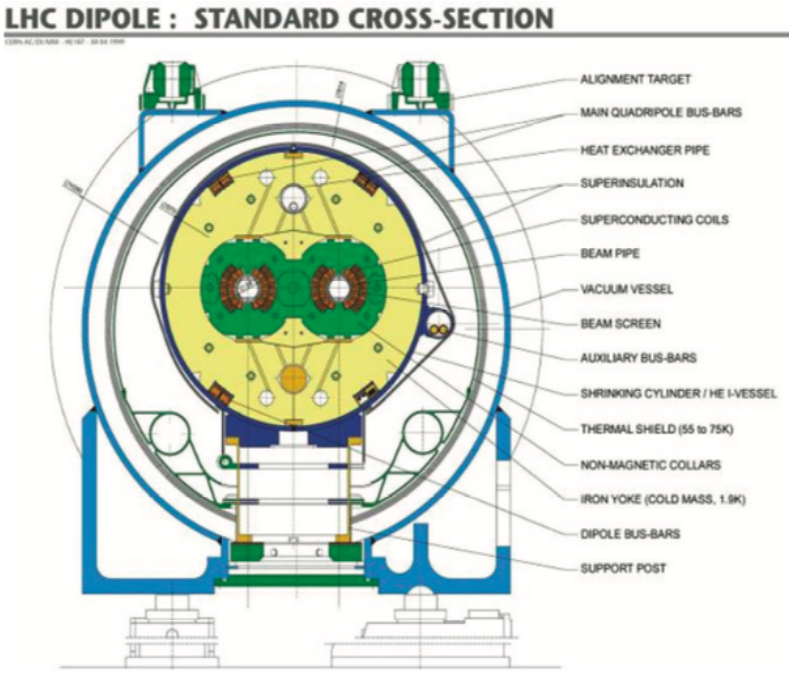

Figure 2.9: Dipole magnet standard cross section [69].

In order to reduce the cryogenic power consumption at 1.9 K in the arcs, the heat load induced by the beam will be intercepted on a beam screen, which operates between 5 and 20 K. In the arcs of the machine, desorbed molecules will be pumped through the pumping slots, distributed along the length of the beam screen, onto the surrounding cold bore held at 1.9 K, see fig. 2.10.

This beam screen is made of steel with a surface of co-laminated copper. It is thermally isolated from the cold mass and kept at a temperature between 4.6 and 20 K, which allows for more efficient cooling compared to 1.9 K, the temperature of the superconducting coils of the magnets. The beam screen is cooled by a flow of weakly supercritical helium through two small attached tubes (see fig. 2.10) and is perforated to enable the vacuum pumping of the volume inside. The pumping slots are covered by shields that intercept electrons before they can reach the cold bore, since otherwise they would greatly reduce the effectiveness of the beam screen

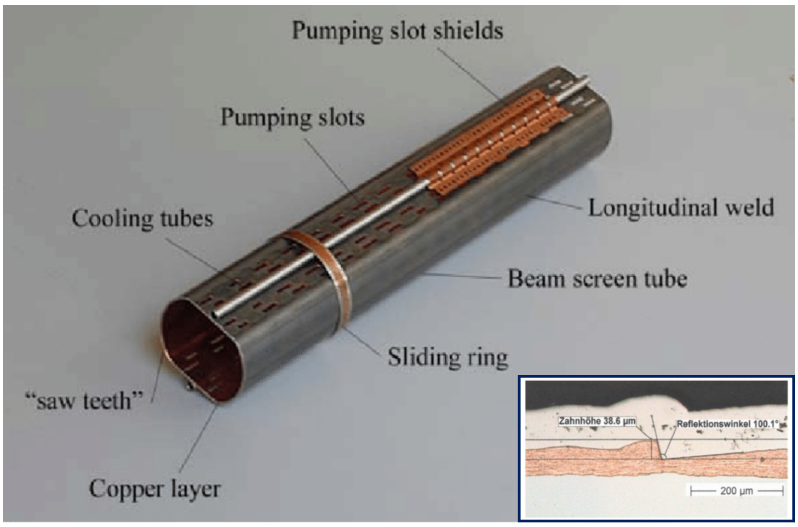

Figure 2.10: The LHC beam screen (horizontal diameter 46 mm) and Sawtooth design(insert) optimized to reduce e-cloud effect [12, 29, 101].

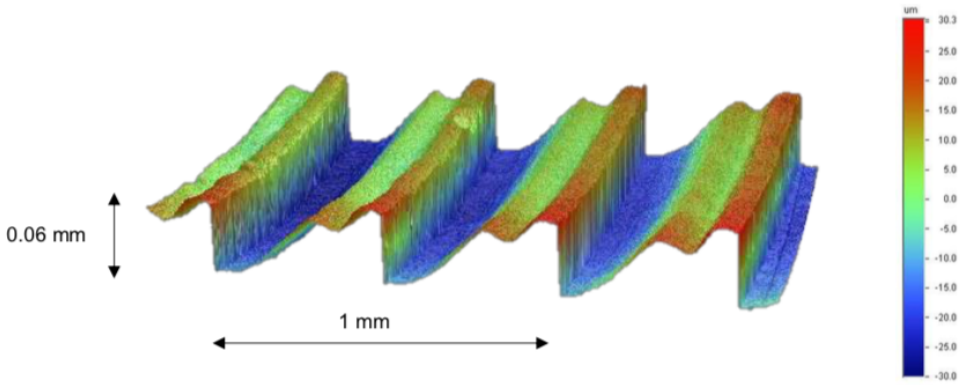

Figure 2.11: LHC Cu Sawtooth design optimized to reduce e-cloud effect and the surface has measured at CERN's metrology lab with an optical profilometer [75].

as heat-load absorber.

The LHC beam pipe has been designed and produced with a "saw-tooth" structure on the equator where the photons first impinge, so as to move from a grazing incident SR close to normal incidence impact, hence reducing its reflectivity. Avoiding a grazing impact of the photons and provides a smaller probability of reflection, with the effect that a large fraction of photoelectrons is generated at the side of the chamber and only a very limited fraction is generated elsewhere. Figure 2.11 shows the teeth profile of a LHC's BS analysed at CERN's metrology lab, showing the valley-peak structure, aimed at intercepting the radiation with perpendicular incidence. Owing to the optical properties of light,

the absorption is higher the higher the grazing angle of incidence is. This effect is specially accentuated in the case of X rays [75].

2.6 Laser Ablation Surface Engineering

As seen above, laser treated surfaces are candidate of Beam Screen in FCC-hh because of their low Secondary Electron Yield (SEY).

The mechanism of laser ablation depends on material properties, laser properties, the environment and various experimental parameters like pulse duration, repetition rate and spot size [98]. For short laser pulses in micro and nanosecond range, like in the studied samples, the ablation process is dominated by heat conduction, melting, evaporation and plasma formation (see fig. 2.12 (a)). The energy of the laser pulse is absorbed on the surface of the workpiece and heat conduction leads to the formation of a temperature field. Depending on the achieved temperature the material is molten up, evaporates or is transferred to a plasma state. Ablation is determined by both evaporation and melt expulsion. It depends on which mechanism is dominant between pulse duration and pulse energy.[64]

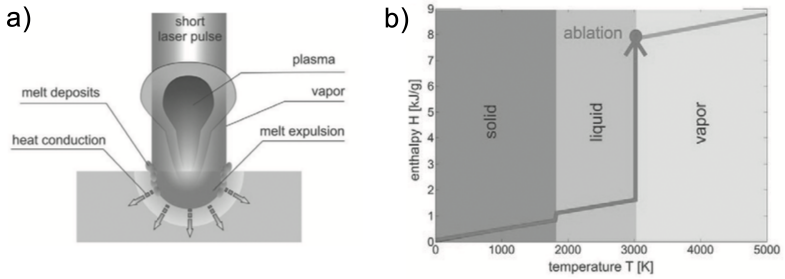

Figure 2.12: Ablation model: (a) Beam-Matter interaction, (b) temperature enthaply diagram [64]

To estimate ablation rate from energy conservation it is possible to assume that all the energy of the laser pulse leads to material evaporation. Looking at the temperature enthaply diagram, fig. 2.12 (b), we can say that the energy of the laser pulse is applied in order to heat up the surface to evaporation temperature and to overcome the latent heat of melting and evaporation. Material in a vapor state is ablated.

The LASE candidate is made by STFC starting by commercially available rolled, electro-polished oxygen-free copper with high purity. It was irradiated by pulses of Nd:YAG laser with $\lambda = 355nm$, $3W$ average power and with a 25 nm pulse duration at repetition rate of 40 kHz ($75\mu J$ per pulse). This results in fluence of 42 Jcm^{-1} for a spot diameter of 15 μm at $1/e^2$ intensity [20, 98].

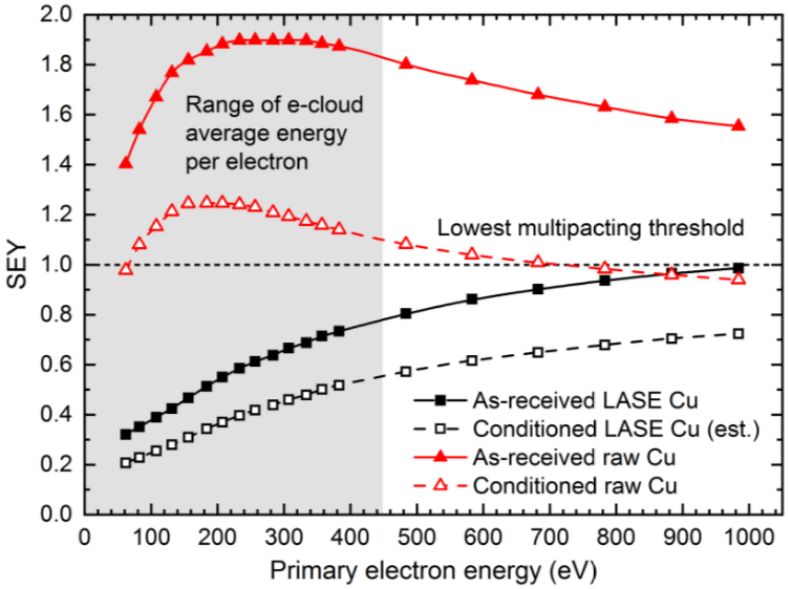

Figure 2.13: Comparison of FCC-hh baseline LASE's SEY [98] and raw Cu [97] SEY, conditioned and unconditioned. The range of most common electron energies is also shown for SEY curves Cu-like [75].

In accelerator physics laser ablation is a new approach for the creation of surfaces with topographically reduced SEY (see fig. 2.13). In fact, the metal surface modification by the laser irradiation leads to the formation of three different scales of organised surface structures: microstructure grooves ranging from 8 to 100 μn deep, coral-like submicron particles superimposed on the grooves which are made of agglomeration of nanosphere (see fig.2.14 (b) and (c)). The laser irradiation can transform highly reflective metals, like copper, to black or dark coloured metal. It is for this reason that laser ablation treatment is also known as blackening process [97].

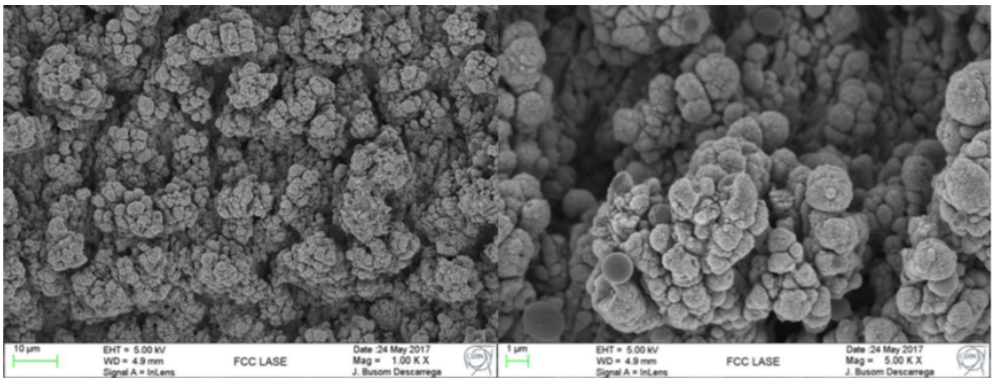

Figure 2.14: 1.00 K and 5.00 K SEM magnification, (left panel) and (right panel) respectively, of a Cu baseline LASE sample, showing the high roughness of the surface, measured at CERN [75].

2.7 The samples

In light of what has been said so far, to understand the role of the roughness, we first select four copper samples, with different surface treatments. The samples named Cu 1A, Cu 1B, Cu 2A, differ only for treatment and roughness and we compare them with LHC flat sample, i.e. the flat zone on top and bottom of LHC BS. We studied all these flat samples with 50nm of amorphous Carbon coverage (realized via magneto-sputtering) to understand the effect of a coating on Reflectivity and Photo Yield. Finally we studied accelerator peculiar surface like LHC Saw-Tooth and LASE. Summarizing, the samples that have been studied (see fig. 2.15) are:

- two copper sample polished, Cu 1A and Cu 2A (10 cm long), with and without a-C coating;
- one copper sample lapped, Cu 1B (10 cm long, with and without a-C coating);
- LHC Beam Screen (BS), flat zone (30 cm long), with and without a-C coating;
- LHC Beam Screen (BS), Saw-Tooth zone (30 cm long);
- Cu sample treated by Laser Ablation Surface Engineering (LASE, made by the Science & Technology Facility Council (STFC))(30 cm long).

The details about the sample roughness and the experimental results are shown and discussed in chapter 4.

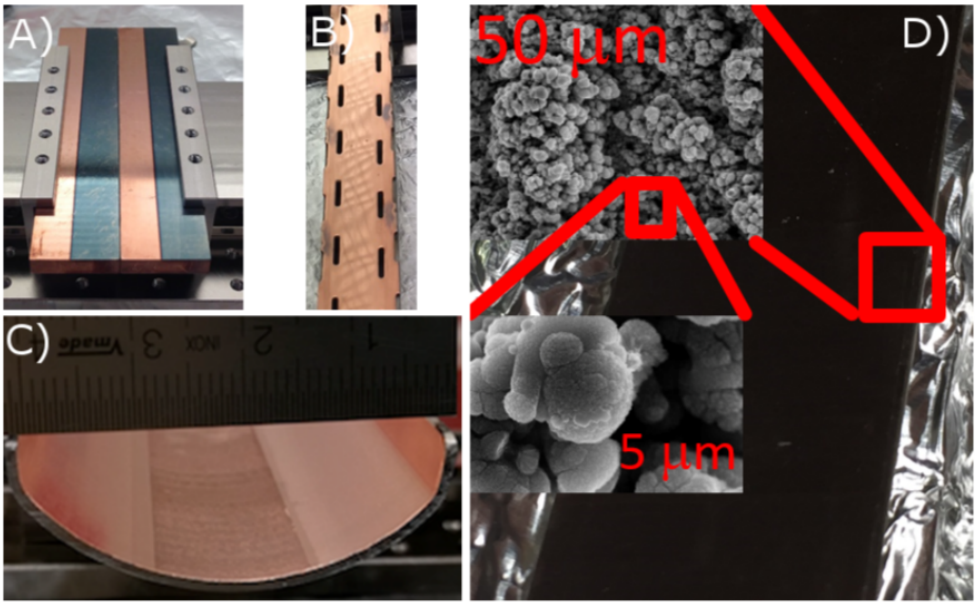

Figure 2.15: Pictures of the investigated samples: A) Flat Copper (Cu1A 1nd 2A) with and without carbon coating, B) LHC Copper (Cu LHC) with and without carbon coating, C) LHC Copper Saw Tooth (ST), D) Laser Treated Copper (LASE)

Chapter 3

Experimental Set-up

The experimental measurements are performed at Bessy II, in Berlin. They have been done during five different beam-times that took place over the three years of the Ph.D. BESSY II employs an electron gun to generate a 70 kV electron beam. Before injection in the main storage-ring the beam is accelerated by a microtron and a synchrotron to its final energy of 1.7 GeV. The accelerating process takes 50 ms and the repetition rate is 10 Hz. The total current in the storage ring is around 200 mA. The ring works in the so called *Topping up* mode. The accumulated electron beam current is maintained quasi constant by continuous injections.

Some storage ring parameters are summarized in the table 3.1 [2].

Table 3.1

Storage ring specifications
Year: 1998 BESSY II operation begins
Storage ring: circumference 240 m
Deflecting magnets: 32
Pulse duration: approximately 20 picoseconds
Electron energy: 1.7 GeV
Nominal beam current: 300 mA
Energy range of emitted radiation: from coherent THz radiation up to 150 keV
Total number of beamlines or end stations: 43

3.1 The optical beam line at Bessy II

The optical layout of the beamline used to perform our experiments is presented in Figure 3.1.

The beam delivered by BESSY II is collected by the collimating mirror M1 that focusses the incident beam horizontally and collimates vertically. The monochromator equipped with a plane grating (PG) monochromator with two blazed gratings (600 l/mm and 1200 l/mm) and with a rotatable

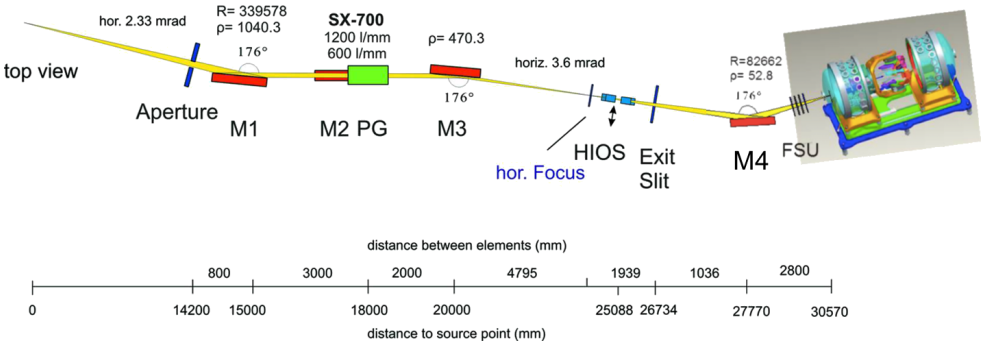

Figure 3.1: BESSY II Optical layout of the Optics Beamline reflectometer end station (top view) [86, 87]

.

plane mirror M2. The beam is then vertically focused by the cylindrical mirror M3 onto the exit slit (SL). The refocusing toroidal mirror M4 focuses the light onto the sample position. In this way a quasi collimated beam on the sample can be obtained, which is a fundamental request for our experiments with grazing incidence angle in conditions as close as possible to the real "life" in new accelerator machines. In the beam path there are also an High order suppressor (HiOS) and a filter and slit unit (FSU), a double set of aperture and absorption filters [87]. At this point the photons arrive into the experimental chamber equipped with the 4-circle UHV-Reflectometer. The details of the beam-line are reported in tab.3.2 [2].

The 4-circle UHV-Reflectometer is an instrument for at-wavelength metrology and calibration of XUV optical elements. This Reflectometer provides the possibility to incorporate large samples (up to 4 kg and 360 mm in length) into the UHV-chamber. Samples are adjustable in all the six degrees of freedom by an UHV compact tripod system. The reflectivity can be measured between $-175°$ and $+175°$ incidence angle (at a mechanical level the detectors can move in the range $(-180° \div 180°)$, however the measurements are limited to 175° because of the shadow given by the detector and its support) for both s- and p-polarisation geometry by azimuthal rotation of the sample around the beam direction. The Reflectometer is located in a moderate clean-room hutch at the experimental floor of BESSY II and is permanently attached to the Optics Beamline PM1 at Dipole 1.1. The optical design was matched to reflectometry requirements: high spectral and stray light purity, large working energy range, low divergence of incident beam and energy resolution.

Some relevant Reflectometer parameters are summarized in tab.3.3. A large stainless steel base plate of 700 mm diameter rigidly attached to

Table 3.2

Instrumental data

Location	section DIP 1.1
Source	Dipole
Monochromator (gratings)	SX700 (600 l/mm, 1200 l/mm)
Energy range	10 eV - 2000 eV
Energy resolution	$E/\Delta E$ = 1000 - 10000
Flux	$10^{10} - 10^{11}$ photons/s/100 mA
Polarization	Horizontal-linear, elliptical
Divergence horizontal	3.5 mrad
Divergence vertical	0.5 mrad
Focus size (hor. x vert.)	0.3x0.2 mm^2
Distance Focus/ last valve	1290 mm
Height Focus/ floor level	1430 mm
Free photons beam available	No
Fixed end station	4-circle UHV-Reflectometer
Absorption filters	Mg, Al, Be, B, C_6H_8, Ti, Cr, Fe, Cu
HiOS mirrors coatings	Si, AlF3, C
Experiment in vacuum	operative pressure: 10^{-9} mbar
Max. sample size	360 x 60 x 60 mm^3
Max. sample size for LoadLock	50 x 50 x 10 mm^3
Maximum sample weight	4 kg
Sample surface scan	15 x 15 mm
Incidence angle scan range	$-180° \leq \theta \leq 180°$
Azimuthal angle scan range	$0° \leq \beta \leq 360°$
Detector scan range (in plane)	$-180° \leq \theta \leq 180°$
Detector scan range (off plane)	$4° \leq \Theta_D \leq 4°$
Min. step size for all motors	0.001°
Sample – Detector Distance	310 mm
Detector	GaAsP-photodiodes
Detectors size	4 x 4 mm^2, slits or pinholes: 0.14 – 4 mm

Table 3.3: Reflectometer parameters

Axis	**Hardware**	**Range**	**Pos. accuracy**
Azimuth angle φ	HUBER 430	$-180° \div 180°$	$3.6''$
Sample angle θ	HUBER 411	$-90° \div 270°$	$3.6''$
Detector angle 2θ	HUBER 411	$-180° \div 180°$	$3.6''$
Detector off-plane ϕ	ceramic motors	-20mm $\div 20$mm ($-4° \div 4°$)	50 nm
Sample adjust. T_x, T_y, T_z	ceramic motors	-20mm$\div 20$mm (not simul.)	500 nm
Sample adjust. R_x, R_y, R_z	ceramic motors	$-10° \div 10°$ (not simul.)	$1''$

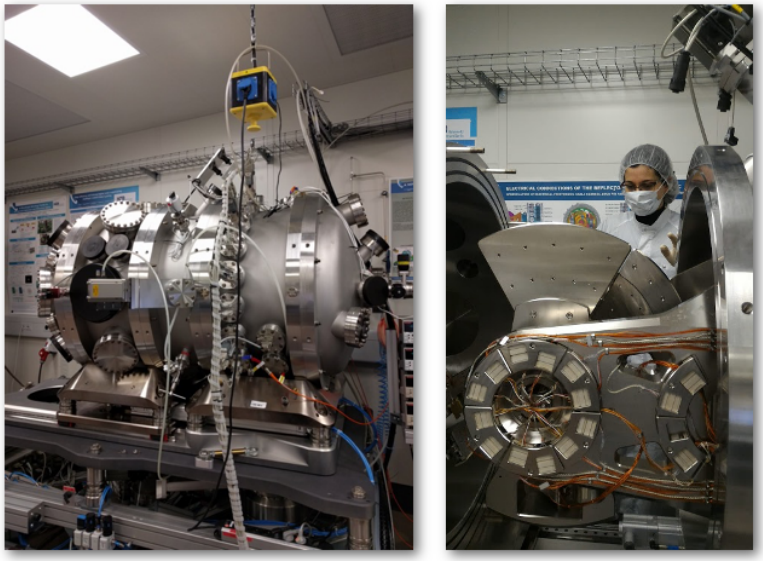

Figure 3.2: Reflectometer in Optics Beam-line at Bessy II.

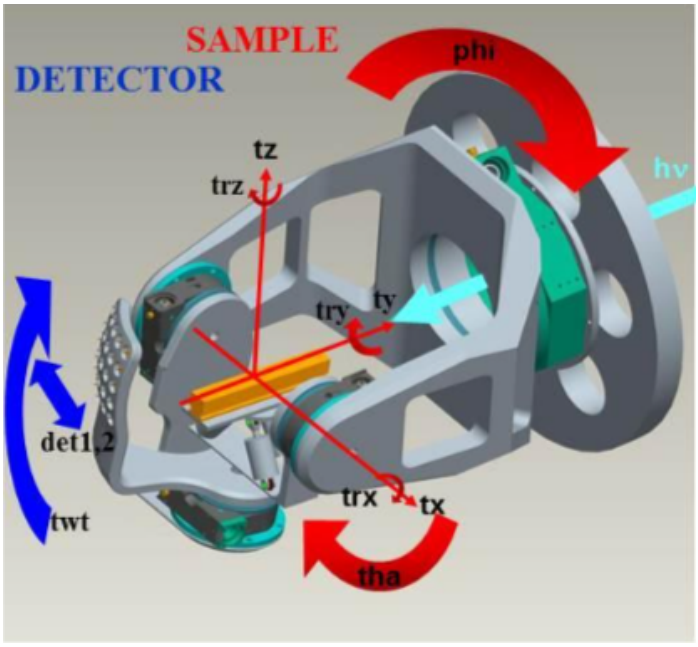

Figure 3.3: Artistic view of the reflectometer inside.

the chamber wall holds a large goniometer (Huber model 430) for the azimuthal (respect to beam) rotation (φ angle) and the tripod unit allows adjustment of the sample base plate in six degrees of freedom: translations T_x, T_y and T_z and rotations R_x, R_y, R_z. The detector position is given by 2θ and ϕ, while θ is the incidence angle of the beam on the sample. In fig.

3.3 an artistic view of the Reflectometer inside is reported. The sample translation movements are indicated by tx, ty and tz; rotations by trx, try and trz. The incidence angle is $tha = \theta$. The detector coordinates are $twt = 2\theta$ and $det1 = \phi$ and the azimuthal (respect to beam) rotation $phi = \varphi$ angle.

			TRIPOD							Gon					SCAN					
file #	mple short na	Sample info	ttx	tty	ttz	trx	try	trz	en	phi	tha	twt	det1	dety	can mo	Scan m. 1	Start	Stop	Step	Steps
12504	Io		0	0	-3	0	0	0	1060.5	0	0	0	0	0	ascan	en	1221	900	6	53.5
12505	Cu ST	Cu LHC- saw tooth	0	0	0	0	0	-0.1	1060.5	0	0.25	0.5	0	0	ascan	en	1221	900	6	53.5
12506	Cu ST	Cu LHC- saw tooth	0	0	0	0	0	-0.1	1060.5	0	0.5	1	0	0	ascan	en	1221	900	6	53.5
12507	Cu ST	Cu LHC- saw tooth	0	0	0	0	0	-0.1	1060.5	0	1	2	0	0	ascan	en	1221	900	6	53.5
12508	Io		0	0	-3	0	0	0	795	0	0	0	0	0	ascan	en	920	670	1	250
12509	Cu ST	Cu LHC- saw tooth	0	0	0	0	0	-0.1	795	0	0.25	0.5	0	0	ascan	en	920	670	1	250
12510	Cu ST	Cu LHC- saw tooth	0	0	0	0	0	-0.1	795	0	0.5	1	0	0	ascan	en	920	670	1	250
12511	Cu ST	Cu LHC- saw tooth	0	0	0	0	0	-0.1	795	0	1	2	0	0	ascan	en	920	670	1	250
12512	Io		0	0	-3	0	0	0	560	0	0	0	0	0	ascan	en	680	440	2	120
12513	Cu ST	Cu LHC- saw tooth	0	0	0	0	0	-0.1	560	0	0.25	0.5	0	0	ascan	en	680	440	2	120
12514	Cu ST	Cu LHC- saw tooth	0	0	0	0	0	-0.1	560	0	0.5	1	0	0	ascan	en	680	440	2	120
12515	Cu ST	Cu LHC- saw tooth	0	0	0	0	0	-0.1	560	0	1	2	0	0	ascan	en	680	440	2	120
12516	Io		0	0	-3	0	0	0	355	0	0	0	0	0	ascan	en	450	260	2	95
12517	Cu ST	Cu LHC- saw tooth	0	0	0	0	0	-0.1	355	0	0.25	0.5	0	0	ascan	en	450	260	2	95
12518	Cu ST	Cu LHC- saw tooth	0	0	0	0	0	-0.1	355	0	0.5	1	0	0	ascan	en	450	260	2	95
12519	Cu ST	Cu LHC- saw tooth	0	0	0	0	0	-0.1	355	0	1	2	0	0	ascan	en	450	260	2	95
12520	Io		0	0	-3	0	0	0	220	0	0	0	0	0	ascan	en	265	175	1.5	60
12521	Cu ST	Cu LHC- saw tooth	0	0	0	0	0	-0.1	220	0	0.25	0.5	0	0	ascan	en	265	175	1.5	60
12522	Cu ST	Cu LHC- saw tooth	0	0	0	0	0	-0.1	220	0	0.5	1	0	0	ascan	en	265	175	1.5	60
12523	Cu ST	Cu LHC- saw tooth	0	0	0	0	0	-0.1	220	0	1	2	0	0	ascan	en	265	175	1.5	60
12524	Io		0	0	-3	0	0	0	137.5	0	0	0	0	0	ascan	en	180	95	1	85
12525	Cu ST	Cu LHC- saw tooth	0	0	0	0	0	-0.1	137.5	0	0.25	0.5	0	0	ascan	en	180	95	1	85
12526	Cu ST	Cu LHC- saw tooth	0	0	0	0	0	-0.1	137.5	0	0.5	1	0	0	ascan	en	180	95	1	85
12527	Cu ST	Cu LHC- saw tooth	0	0	0	0	0	-0.1	137.5	0	1	2	0	0	ascan	en	180	95	1	85

Figure 3.4: An example of user macro. These settings are referred to Cu LHC flat sample Reflectivity scan as a function of photon energy.

The signals arriving from the detectors and sample holder are collected by Keithely Electrometers. The sample holder is electrically insulated to measure photo yield and no bias is applied.

The instrument, together with the beamline is operated with SPEC-program (trade name by Certified Scientific Software Corp.). This allows full flexibility of positioning and calibrating all motors individually and performing measuring scans as a function of all individual involved motors or a combination of motors. The SPEC program can be operated by user friendly macros (see 3.4). All parameters are setted in the user macro as sample position, monochromator energy, incidence and reflection angle, starting and ending points of scans and step size. Furthermore, there are all beamline parameters (these values are outside of 3.4 picture for size reasons).

The following code is the commands set enclosed in the first row of the user macro shown in fig. 3.4.

```
print("# File: 12504 -- Sample: Io -- Scan: ascan en -- energy:
    1060.5eV -- theta: 0 -- Region:  -- Filters: no-and-no")
Sample "Io"
%we are acquiring primary beam
Comment "Sample:_Io-file:_Region:_filters:no-and-no_comments:"
Filter1 0
 % no filter inserted
Filter2 0
% no filter inserted
```

```
Slit1 0
 % no slit inserted
Slit2 9
delay = 0.5
%delay between two acquisition
keithleyconfig 1 0 0.3 5
 % keithley disabled
keithleyconfig 2 1 0.3 5
 % keithley enabled connected to the detector
keithleyconfig 3 1 0.3 5
 % keithley enabled connected to the sample holder
keithleyconfig 4 0 0.3 5
 % keithley disabled
#
setcff 2.5
%  c-factor of monochromator
umv htr Auto%  High order suppressor activated in automatic mode

A[top] = 3; A[bot] = 3; A[left] = 6; A[right] = 6
 %referred to WAU aperture
A[rx] = -18.8; A[slit] = 200; A[en] = 1060.5; A[phi] = 0;  %
    monochromator settings
A[tha] = 0; A[twt] =0; A[det1] =0;% goniometer settings
A[hm2] =0; A[hm1] =0% high order suppressor mirrors angle
A[ttz] = -3; A[tty] = 0; A[ttx] = 0; A[trz] = 0; A[try] =0; A[trx
    ] =0;  % sample holder settings
A[en] =1221 % starting energy value
scan_move
% command to monchromator to move

wa
 % print positions of detector
print("now sleep time before measurements for 15sec")
do_sleep 15 % sleep 15 sec before starting data acquisition
ascan en 1221 900 54 1
% start hte scan, from 1221 eV to 900 eV, 54 steps, 1 sec of
    delay before read value on keithley
```

The reflectometer control uses Labview program with controllers and drivers for the piezo-motors (Nanomotion) of the tripod and stepping motors (Phytron) for the goniometers. The Cartesian coordinates of the tripod and the goniometer angles are provided as EPICS-variables for the SPEC data acquisition program [36].

3.2 Measurements

A realistic evaluation of the Reflectivity for technical surfaces must be given, necessarily, by two different type of measures. They are schematized in fig.3.5. In our experiment we used only 1200 l/mm grating because it is more sensitive to the high energies we are interested in (FCC-hh critical energy is 4.4 keV).

The beam hight, p-polarized, was 0.3 mm. The measurements were done with two GaAsP-photodiodes, one 4mm x 4mm size (detector 1) and one 0.1 mm x 4 mm size (detector 2), and normalized to incident beam and BESSY II ring current.

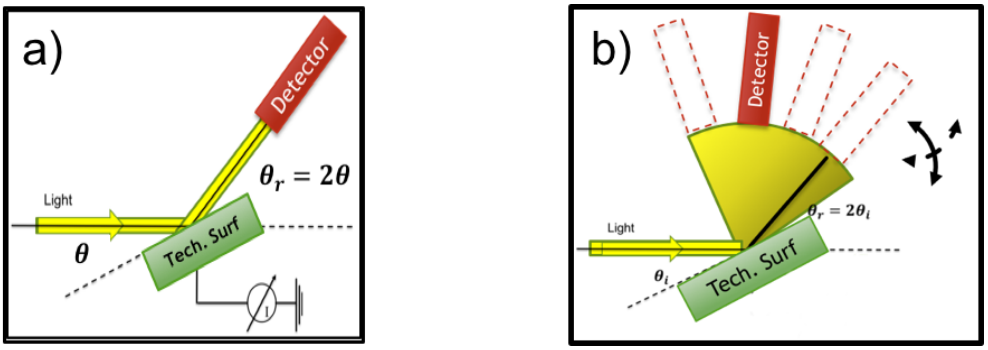

Figure 3.5: Artistic view of experimental set-up. We show in panel a) the experimental set-up for Specular Reflectivity measurements, in panel b) the experimental set-up for Scattered light measurements.

The first configuration (see fig. 3.5 panel (a)) is optimised to measure the Specular Reflectivity, where we used the detector 1 placed at the geometrical $\theta/2\theta$ position (Figure 3.5, (a)). This means that we consider as specular component all the light collected by this detector in this configuration, i.e. the light reflected in $2\theta \pm 0.35°$ and $\phi = 0 \pm 0.35°$ in altitude and azimuthal plane respectively (0.35° is the acceptance of the detector 1 in both direction). In this set-up configuration we studied the variation of Specular Reflectivity as a function of the incidence photon energy from 35 eV to 1800 eV (1200 l/mm grating's energy limits). The measurements are performed at grazing angles of 0.25, 0.5 and 1 degree. We also studied Specular Reflectivity Vs incidence angles at seven photon energies (1800, 1200, 600, 400, 150, 80 and 50 eV).

Total Reflectivity measurements are acquired using the second set-up configuration (Figure 3.5, (b)) i.e. we fixed incidence angle and photon energy and then we scanned the reflected signal while varying the detector angle position. We used detector 2,(detector 2 size $4mm \times 0.1mm$, i.e. $0.018° \times 0.035°$) for these measurements because we were also interested in having information on the reflected beam profile. The incidence angles were, also in this case, 0.25, 0.5 and 1 degree. To study Total Reflectivity it is important to consider all the scattered light, not only in the reflection plane, but also outside the beam plane. Therefore, we considered a portion of solid angle given by $3.5° \times 5°$ for flat surfaces and $3.5° \times 175°$ for very rough samples. We have seen that, also for very rough surface like LASE, photons scattered outside of 3.5° in horizontal plane are negligible. For flat samples we have cut off the vertical scan at 5° after observing that

even in this range no appreciable signal had been left out. In fact, photons outside of this cone are limited in number. Neglecting them, for reducing measuring time and to avoid summing any artificially background, may affect the measured total reflectivity within the quoted errorbar. In this way we can consider the measured Total Reflectivity (R_t) a close but lower estimate of the real (R_t) that will be obtained by full solid angle integration.

In all cases we simultaneously measured the Photo Yield (PY). PY is the number of photoelectrons generated divided by the number of impinging photons.

During the experiment the sample under study was electrically insulated and connected to the ground through a Keithely pico-ammeter. The number of photoelectrons is obtained by measuring the drain current from the electrical insulated sample. No bias was applied not to add unwanted noise to the measurements. This may have caused a reduced PY signal due to eventual space charge effects. Due to the low current emitted by the studied surfaces this reduction could be considered negligible and distributed along the surface. The number of the impinging photons is calculated multiplying the photodiode drain current by its quantum efficiency (GaAsP from Hamamatsu, [3]), which is a tabulated value function of photon energy, as shown in fig.3.6.

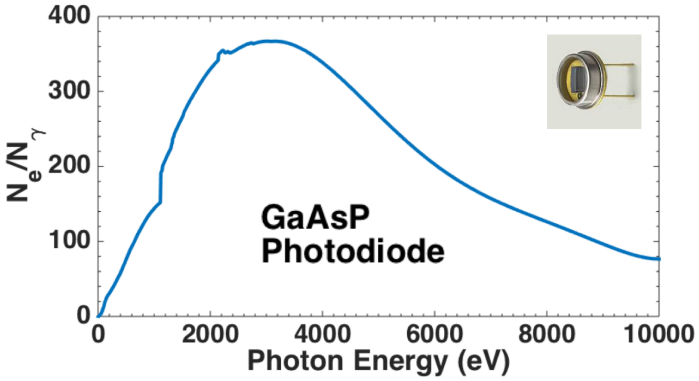

Figure 3.6: Quantum efficiency VS Photon Energy of the GaAsP photodiode [3].

3.3 AFM measurements of roughness

The values of roughness of Copper flat samples, with and without Carbon are obtained by $20 \times 20 \mu m^2$ Atomic Force Microscope (AFM) analysis (see fig.3.7). These measurements are performed twice: the first time at HZB Optical in Berlin, the second time in Rome, at the Centro di Ricerca per le Nanotecnologie applicate all'Ingegneria (CNIS). The AFM

measurements at CNIS are done with Veeco ICON. The acquisition data software was Nanoscope V. The measurements are done in tapping mode and the tip (manufactured by Bruker) parameters are:

- Model:RTESP-300;
- Material 0.01-0.025 Ohm-cm Antimony (n) doped Si;
- Cantilever: $T = 3.4\mu m, \quad L = 125\mu m\ , \quad W = 40\mu m,$ $f_0 = 300kHz, \quad k = 40N/m.$

We recorded scans information on amplitude, height and phase. The AFM pictures are aquired with 512 $\times$ 512 pixels resolution and processed with Gwyddion 2.50 [4]

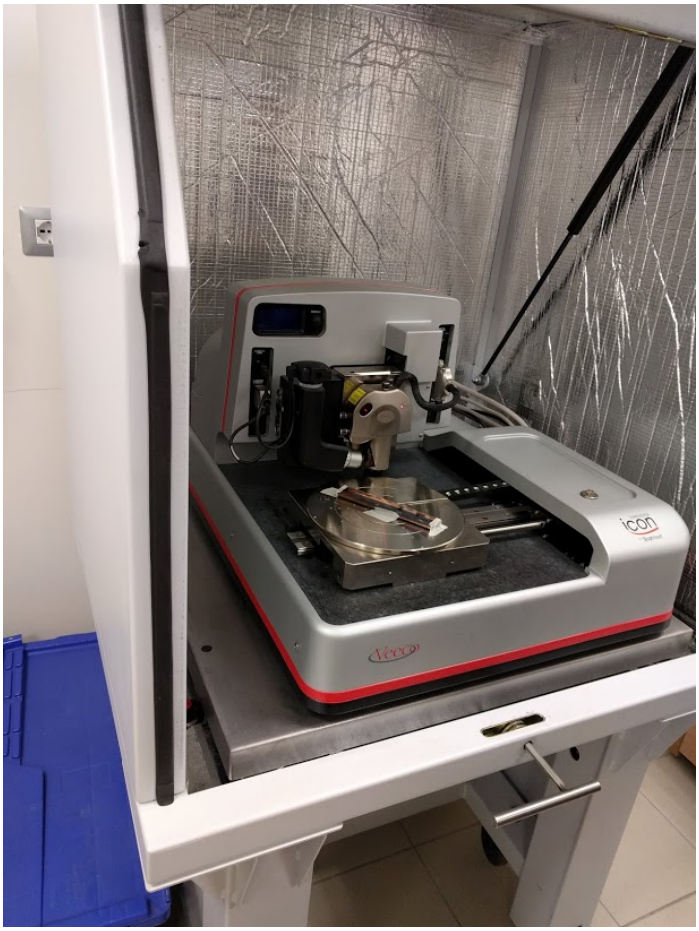

Figure 3.7: Atomic Force Microscope at CNIS.

Chapter 4

Results and discussion

The experimental data about Reflectivity and Photo Yield (PY) measurements are presented in this chapter. The results were also presented in international workshops [47, 61, 62, 65, 66] and will be published in [60].

4.1 Flat Copper Samples

The starting point of our analysis is the study of samples with the simplest morphology, i.e. the four flat Copper samples with a different surface treatment and roughness (R_a). As mentioned in the previous chapter we evaluated R_a by ($20 \times 20 \mu m^2$) AFM measurements (see fig.4.1). We performed these analyses at three different points to check the homogeneity of the samples. The results are consistent with each other.

Samples details are summarized in tab. 4.1.

Table 4.1: The flat copper samples, surface treatments and roughness

Sample	**Material**	**Surface treatment**	**Roughness (nm)**
Cu LHC	Cu co-laminated on p506 SS	–	15
Cu 1A	Cu	electro-polished	10
Cu 2A			27
Cu 1B	Cu	lapped	25

In order to get an idea of what we expect to find, i.e. to evaluate the behaviour of Specular Reflectivity VS Photon Energy, we simulated the Reflectivity with REFLEC [5], considering a clean copper surface with the roughness reported in tab. 4.1 for the three incidence angles used during the experiment ($\theta_i = 0.25°, 0.5°, 1°$). The results are reported in fig. 4.2.

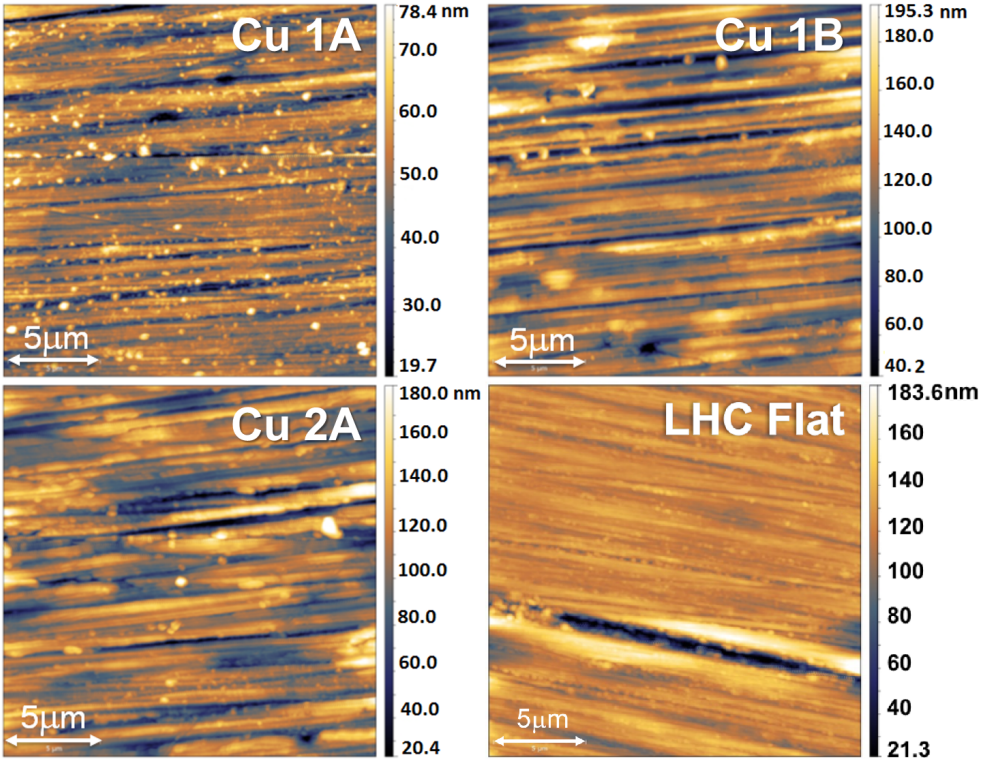

Figure 4.1: AFM measurements of Cu 1A, Cu 1B, Cu 1B and LHC-Flat samples, clockwise direction.

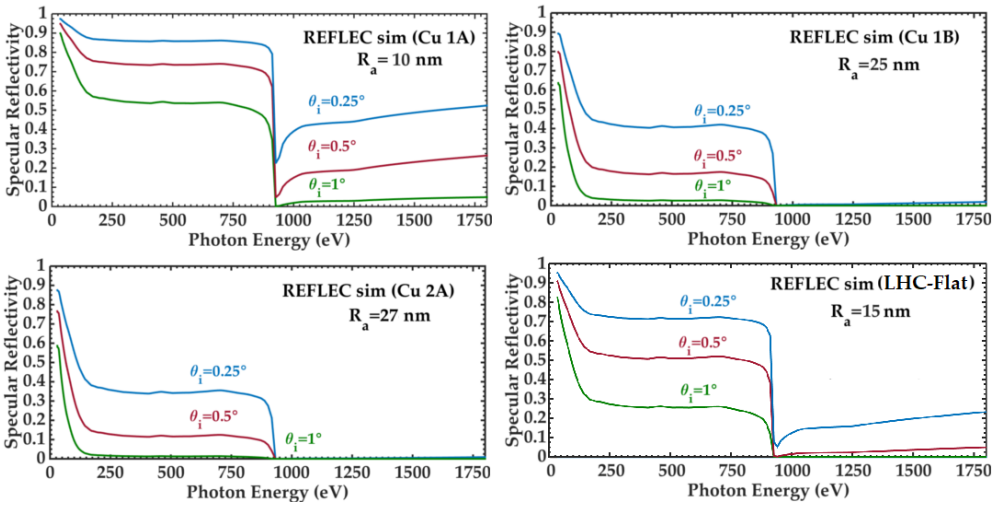

Figure 4.2: REFLEC simulations of Specular reflectivity VS Photon Energy at three incidence angle for a pure copper surface with the Cu 1A, Cu 1B, Cu 2A and LHC-Flat roughness, clockwise direction.

The simulations results are dominated by the Cu-L_{2-3} absorption edge. It produces the drop in reflectivity at ∼930-950 eV recognizable in every plot.

4.1.1 Specular Reflectivity and Photon Yield

In fig. 4.3 the experimental results of the reflectivity are reported as a function of impinging photon energy for the same three different incidence angles ($\theta_i = 0.25°, 0.5°, 1°$). Looking at these data we can do some general considerations:

i. In all cases, Specular Reflectivity is higher at lower photon energies.

ii. In all cases, Specular Reflectivity is higher at lower incidence angles θ_i.

iii. High energy reflectivity (above Cu-L_{2-3}, i.e. above ∼930-950 eV) is greater than predicted by simulations.

iv. Low energy reflectivity (below Cu-L_{2-3}, i.e. below ∼930-950 eV) is lower than the simulations had predicted.

v. In all spectra, in addition to the Copper absorption threshold, we can recognize two other absorption edges due to surface contaminants.

vi. Roughness, as expected, plays a major role in determining the ability of a Surface to reflect impinging photons. For similar roughness (Cu 1B and Cu 2A) the type of surface treatment does not seem to significantly affect the reflectivity.

The points iii), iv) and v) are attributable to the present contaminants on the surface. In fig. 4.4 a comparison of REFLEC simulations and experimental data for Specular Reflectivity VS Photon Energy of Cu LHC sample is shown. Looking at it we can recognize at 280 eV and 530 eV the K-edges of Oxygen and Carbon. The contaminants are responsible of high energy increasing, mainly because of Carbon, and of low energy profile modification, because of the presence of absorption edges, of R. The effect of air contaminants on Reflectivity is larger as the incidence angle is lower. The effect of air contaminants on Reflectivity is greater the smaller the angle of incidence due to the lower penetration of the beam into the bulk material. The dominance of such contaminats layer is therfore expected to be ehanced in FCC-hh, where the incidence angle is only 0.07°.

In simulations, it is very difficult to correctly consider the presence of contaminants and their effects, since the knowledge of the thickness and the composition can not be given. Contaminants contribution at Reflectivity, in particular at very grazing incidence angle, like in accelerators, can be

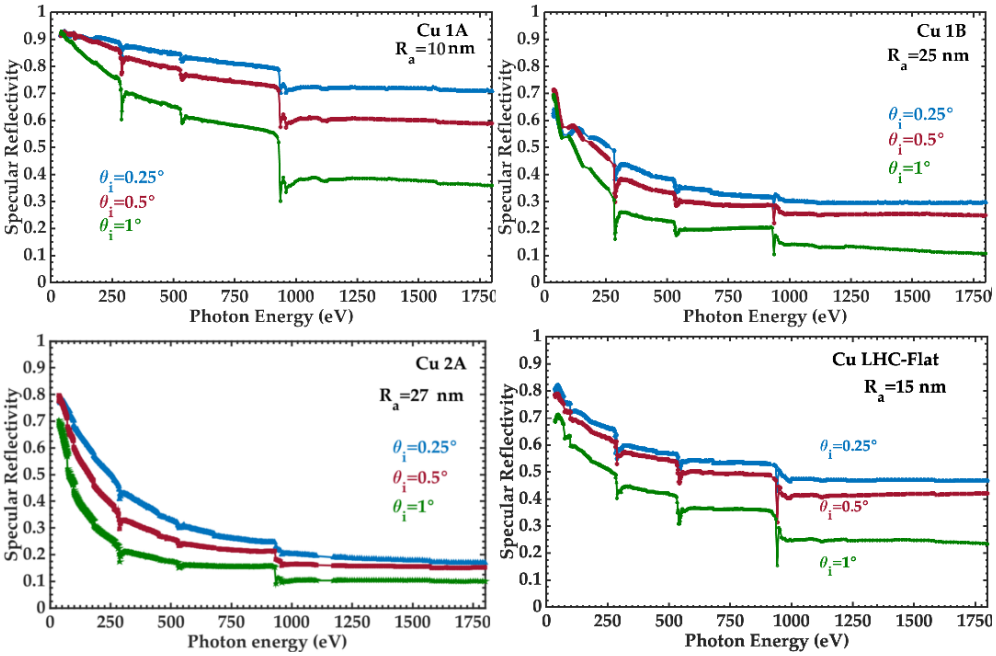

Figure 4.3: Specular Reflectivity VS Photon Energy at three different incidence angles of Cu 1A, Cu 1B, LHC-Flat and Cu 2A sample, clockwise direction.

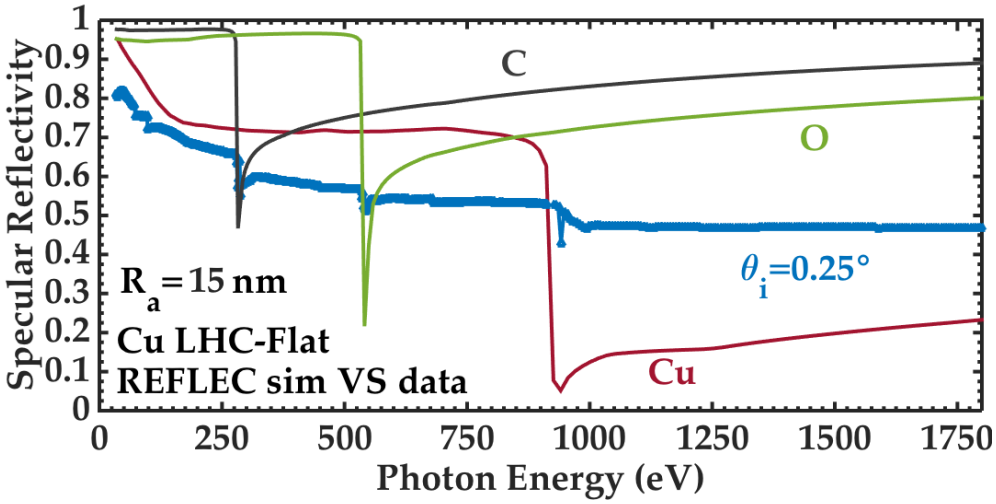

Figure 4.4: Comparison of REFLEC simulations and experimental data of Specular Reflectivity VS Photon Energy of Cu LHC sample ($\theta_i = 0.25°$). To understand the role of air contaminants simulations for Carbon and Oxygen are also reported.

estimated only by a best fit of experimental data. Furthermore, as said in chapter 2, REFLEC considers the roughness as an attenuation parameter (Debye-Waller factor), but such approximation is not really valid for high R_a values of technical surfaces, in particular at high photon energy.

In all measurements we contemporaneously measured the Photo Yield (PY): in fig. 4.5 data acquired Vs Photon Energy are shown.

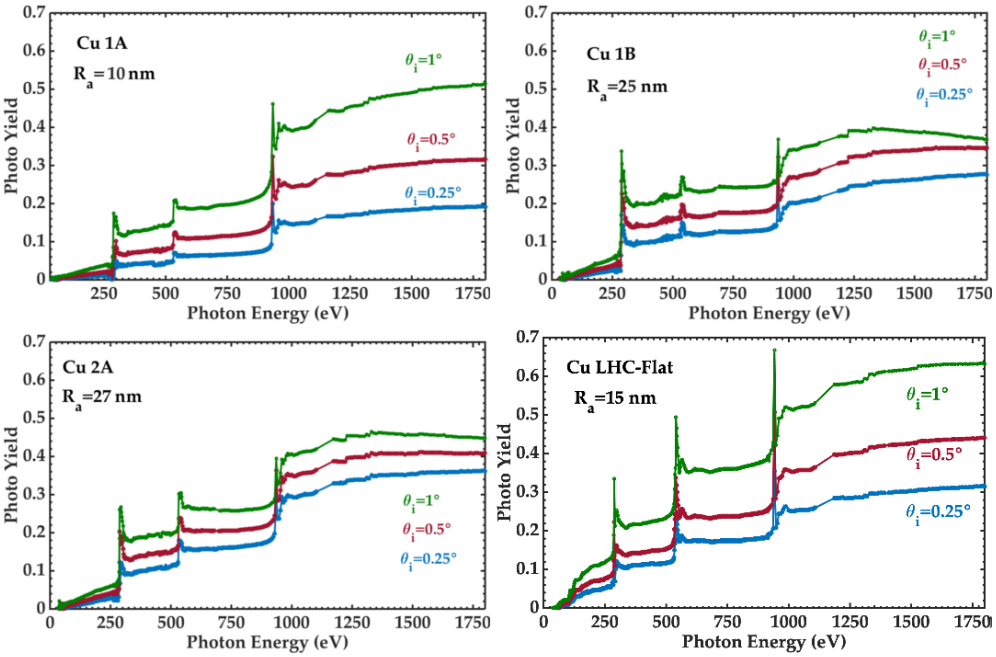

Figure 4.5: Photo Yield VS Photon Energy at three different incidence angles of Cu 1A, Cu 1B, Cu 2B and LHC-Flat sample, clockwise direction.

Looking at these data we see six main general aspects:

i. In all cases, PY is higher at higher photon energies.

ii. In all cases, PY is lower at lower incidence angles θ_i.

iii. The PY dependence of θ_i decreases, until it disappears, with roughness increasing.

iv. In all cases, the Cu-L_{2-3} absorption edge at ∼930-950 eV is recognizable because of an increase in the measured PY at such energies.

v. In all spectra, in addition to the Copper absorption threshold, we can recognize two other absorption edges due to the C K-edge at ∼280 eV end O K-edge at ∼530 eV. They are due to contaminants.

vi. Roughness influences also PY. The lower R_a the higher is PY.

As said before, PY is lower at lower θ_i, this is due to the fact that Reflectivity is higher and, consequently, the number of photons absorbed is reduced. This conclusion is valid at angle of incidence lower than 1-2°: for higher angles more photons are absorbed inside the bulk producing

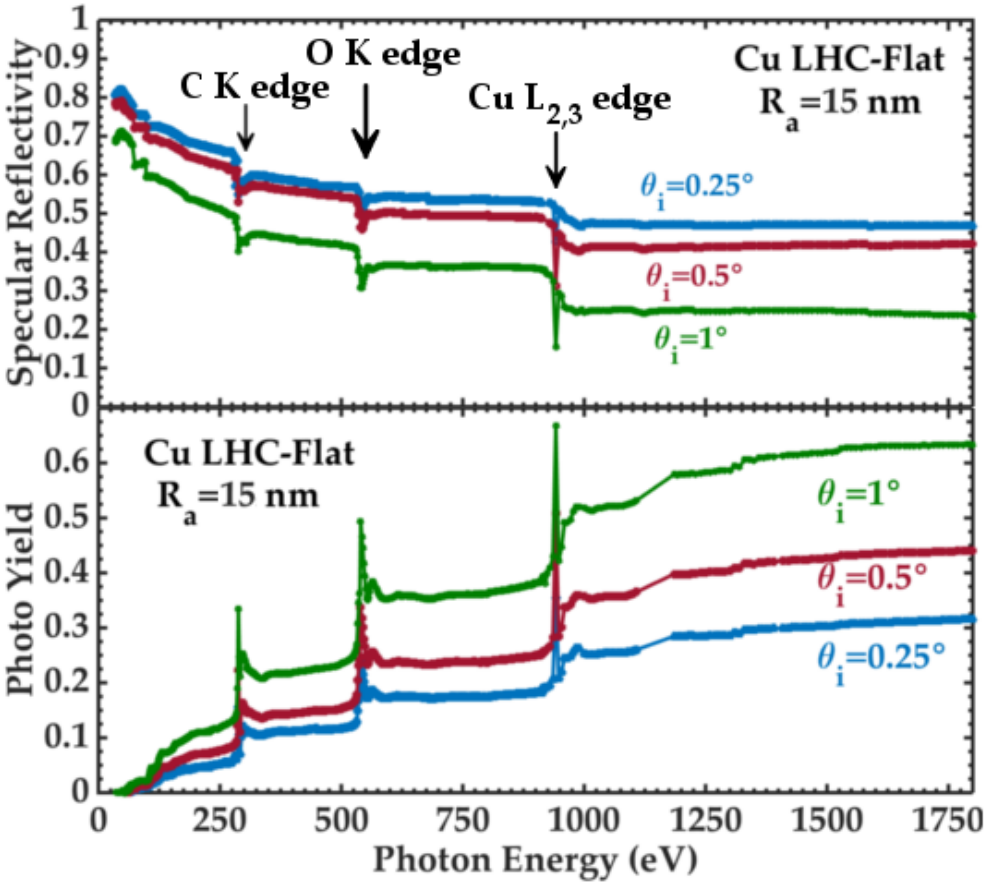

Figure 4.6: Specular Reflectivity (top panel) and Photo Yield (bottom panel) VS Photon Energy of Cu LHC sample.

photoelectrons too far from the surface. This aspect is more evident in fig.4.8 and will be described later.

In order to better understand the PY behaviour we can look at fig.4.6 where Specular Reflectivity (top panel) has also been added for greater clarity. We can see a correspondence between absorption edges, due to copper and contaminants, in Specular Reflectivity and photo yield peaks (bottom panel). Another interesting point is that the diminution of PY in correspondence of an increasing of R_a is not linear. High energy PY of LHC-Flat sample is higher than that measured in the sample Cu1A.

It is important here to remind that PY has been observed to decrease during photon irradiation (as discussed in [24], see chapter 1) with a mechanism similar to the SEY reduction observed during electron bombarding. Indeed SEY and PY differ in irradiation geometry (near to normal incidence in the first case, close to very grazing incidence, in the other one). However, once the excitation particle (electron or photon) has

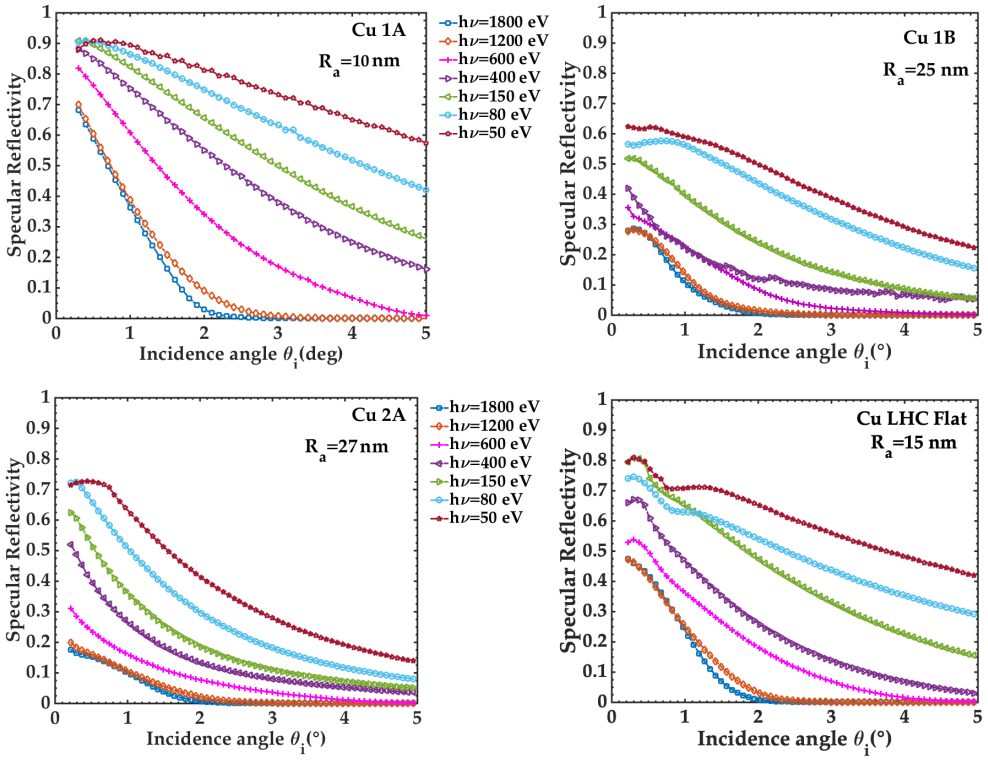

Figure 4.7: Specular Reflectivity VS Incidence angle at seven different photon energies of Cu 1A, Cu 1B, LHC-Flat and Cu 2A sample, clockwise direction.

interacted with the solid, the two processes are very similar, so photon and electron scrubbing are mutually expected to act on PY and SEY in a similar way.

Another type of measurements is shown in fig. 4.7. In this case Specular Reflectivity is studied as a function of incidence angle at seven photon energies: 1800, 1200, 600, 400, 150, 80, 50 eV. In this case we see how high-energy photons (above 500 eV), regardless of sample roughness, are completely absorbed at incidence angles higher than two degrees. Those of low energy are reflected in a good percentage, almost 60% for 50 eV, up to higher angles of incidence. This aspect highlights how many reflections low-energy photons can perform before being finally absorbed by the surface to create photoelectrons.

Also in this case we recorded the photo yield. The data are reported in fig. 4.8. These figures show the effects of two competing processes already discussed. In order to be generated photoelectrons need to absorb energy enough to exceed the work function. This explains the initial increase in PY as the angle increases. However, when the incidence angle becomes too large the photons penetrate very deeply in the solid and the photo-generated electrons are too far from the surface to be able to escape

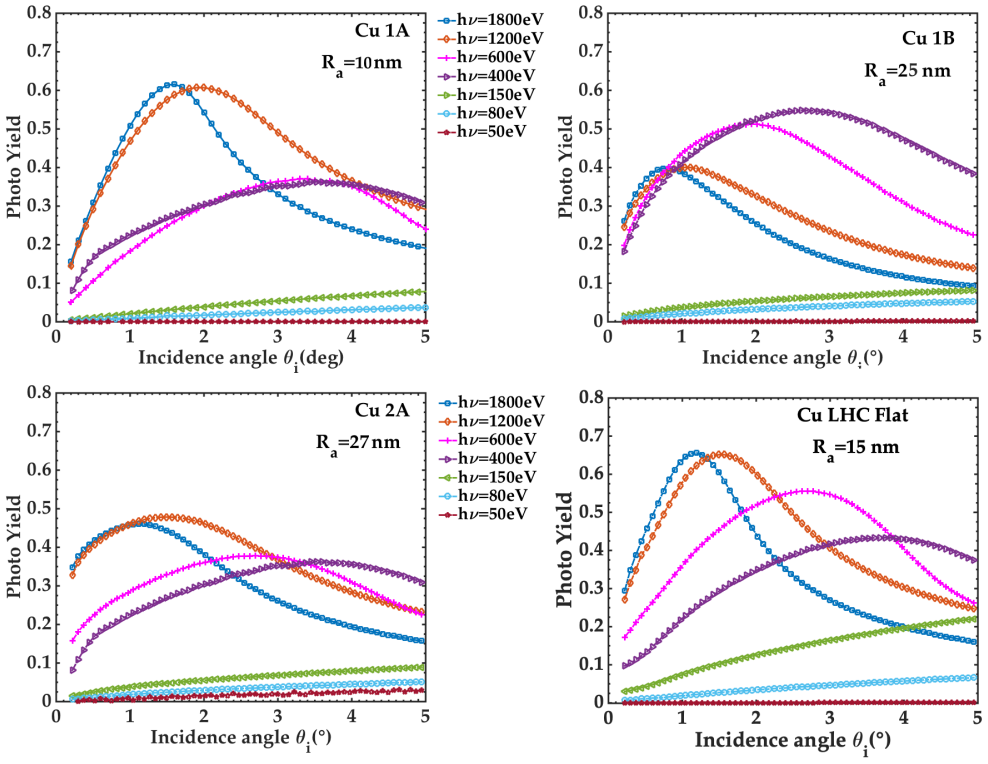

Figure 4.8: Photo Yield VS Incidence angle at seven different photon energies of Cu 1A, Cu 1B, LHC-Flat and Cu 2A sample, clockwise direction.

from it into the vacuum chamber. This effect is clearly caused by the very different mean free path of a photon and of an electron in a solid. The angle at which the trade off between this two competing effects occurs, decreases with photon energy increase.

Moreover, the data confirm that low energy photons are significantly better reflected, in fact at 50 eV, were the reflected component is considerable (for Cu1A sample is 90% ÷ 58%), the number of photoelectrons is not appreciable.

4.1.2 Total Reflectivity

In section 3.2 we described the set-up used to collect data about the R_t. As said before, we consider as specular component all the light collected by the detector placed at $\theta/2\theta$ configuration. It coincides with the light reflected in $2\theta \pm 0.35°$ and $\phi = 0 \pm 0.35°$ in altitude and azimuthal plane respectively ($0.35°$ is the acceptance of the detector 1 in both direction).

In order to understand and evaluate the reflected and scattered light, that is what we define as Total Reflectivity, we scan $3.5° \times 5°$ with the detector 2 (acceptance $0.018° \times 0.35°$). In this type of measurements

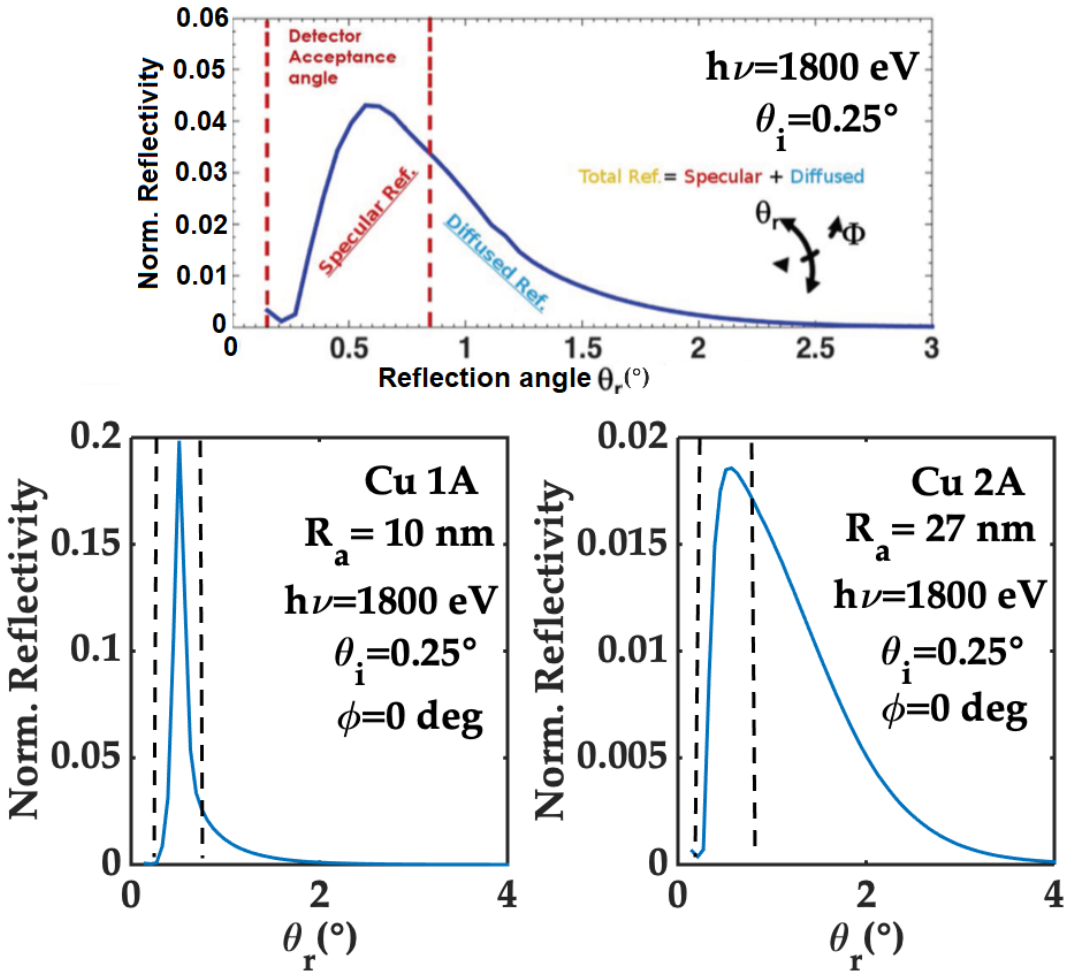

Figure 4.9: Comparison between Specular and Total Reflectivity:(Top Panel) Reflected intensity as a function of θ_r for the case of LHC-Cu at 1800 eV and at fixed $\theta_i = 0.25°$. The detector 1 (4x4mm^2 size) acceptance angle is shown. Specular and diffused and Reflectivity regions are indicated. Cu 1A (Bottom left panel) and Cu2A (bottom right panel) Normalized Reflectivity VS Reflection angle at 1800 eV and incidence angle $\theta_i = 0.25°$. Dotted lines indicate the acceptance of diode used in Specular Reflectivity measurements.

the detector is smaller than beam in vertical direction, and the Total Reflectivity is calculated by integration. This procedure is illustrated in fig. 4.9 where the measured reflected intensity as a function of θ_r for the case of LHC-Flat at 1800 eV and at fixed $\theta_i = 0.25°$ is shown. The detector 1 (4x4mm^2 size) acceptance angle is shown in fig.4.9, in particular in the top panel. Integration in this region will give the measured Specular Reflectivity R, while integration over the full range of θ_i and ϕ will measure the total reflectivity R_t. With this procedure to measure and calculate R_t we could proceed to extract realistic estimates of total reflectivity in

all geometries and photon energy under study. In the bottom panel of fig.4.9 other two curves are shown, i.e. Cu 1A (left panel) and Cu2A (right panel) Normalized Reflectivity VS the reflection angle at 1800 eV and incidence angle $\theta_i = 0.25°$. Also in this case two vertical lines correspond to detector 1 acceptance, so they indicate what we have defined as Specular component. Even in a smooth sample (Cu1A) these two quantities do not coincide, this effect increases with roughness.

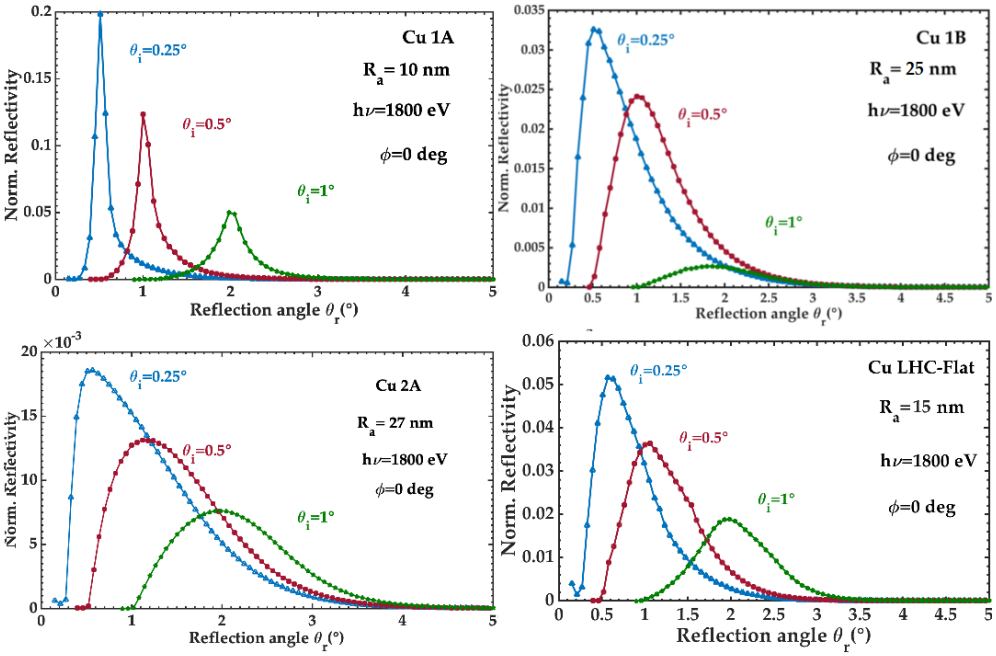

Figure 4.10: Normalized Reflectivity VS Reflection angle at 1800 eV for three different incidence angle. Sample Cu 1A, Cu 1B, LHC-Flat sample and Cu 2A , clockwise direction.

Examples of these data are reported in fig.4.10. Here we can see the angular distribution of reflectivity as a function of reflection angle θ_r, for the three incidence angles at 1800 eV of photon energy. We are looking at the in plane profile ($\phi = 0$). The ordinate axis scale is different for each graph to emphasize the difference in the beam profile. It is possible to recognize the roughness effect on reflected beam profile in its widening. When roughness increases, the distribution in θ_r of the reflected signal broadens and decrease in intensity.

The specular reflectivity R, in those cases, is not a valuable parameter to represent and measure the number of reflected photons from a technical surface and the already discussed decrease, with R_a, of the measured R may not only correspond to real effect but also to the increased production, at larger angles, of diffused photons from the surface. Only measurements obtained by integration of all photons in θ_r and ϕ can then give realistic

input parameters for the total reflectivity from accelerator surfaces.

The variation of Specular and Total Reflectivity as a function of roughness is reported in fig.4.11. For smooth surfaces, like Cu1A, the gap between R and R_t is smaller and then increases with increasing roughness. The same data are reported also in tab. 4.2.

Roughness R_a (nm) (1800 eV)	**Total Reflec.** $\theta_i = 0.25°$ (±5%)	**Specular Reflec.** $\theta_i = 0.25°$ (±2%)	**Total Reflec.** $\theta_i = 0.5°$ (±5%)	**Specular Reflec.** $\theta_i = 0.5°$ (±2%)	**Total Reflec.** $\theta_i = 1°$ (±5%)	**Specular Reflec.** $\theta_i = 1°$ (±2%)
10	0.74	0.61	0.67	0.57	0.47	0.34
15	0.72	0.47	0.63	0.42	0.38	0.24
25	0.55	0.27	0.48	0.24	0.29	0.11
27	0.54	0.18	0.44	0.17	0.26	0.10

Table 4.2: Comparison between Specular and Total Reflectivity of the four samples for three different incidence angle (Photon energy 1800 eV).

The experimental process to measure total Reflectivity is too time consuming to allow us to perform this study with the desired details. A viable solution, for the most relevant case of the LHC-flat surface, is shown in fig.4.12 , where, on top of the curves measuring the Specular reflectivity R as a function of photon energy in the entire energy range available, R_t values, obtained at selected photon energies are plotted for the three different incidence angle studied. The same data are reported also in tab. 4.3.

Photon energy hν(eV)	**Total Reflec.** $\theta_i = 0.25°$ (±5%)	**Specular Reflec.** $\theta_i = 0.25°$ (±2%)	**Total Reflec.** $\theta_i = 0.5°$ (±5%)	**Specular Reflec.** $\theta_i = 0.5°$ (±2%)	**Total Reflec.** $\theta_i = 1°$ (±5%)	**Specular Reflec.** $\theta_i = 1°$ (±2%)
1800	0.72	0.47	0.63	0.42	0.38	0.24
1200	0.71	0.47	0.61	0.41	0.42	0.25
800	0.80	0.54	0.76	0.49	0.66	0.36
600	0.76	0.54	0.74	0.50	0.64	0.37
400	0.79	0.59	0.79	0.56	0.72	0.44
150	0.95	0.71	0.93	0.678	0.78	0.57
80	0.92	0.76	0.92	0.73	0.85	0.63
50	0.96	0.82	0.94	0.79	0.92	0.71

Table 4.3: Comparison between Specular and Total Reflectivity of LHC Flat sample at eight different values of photon energy.

We show here, for the first time in this context, that, increasing R_a, the geometrical reflectivity nearly vanish (as seen from fig. 4.10). We observe Specular Reflectivity, i.e. all the scattered light within a cone of

$\pm 0.37°$ centred around the geometrical reflection decrease significantly while R_t remains significant even at high photon energies. The comparison between specular and total reflectivity for the case of the LHC-Flat sample shown in fig. 4.12 and the data reported in tab. 4.2 and tab. 4.3 confirms the importance of considering R_t as the relevant quantity to be used in simulations when studying reflectivity related properties at very grazing angle of incidence.

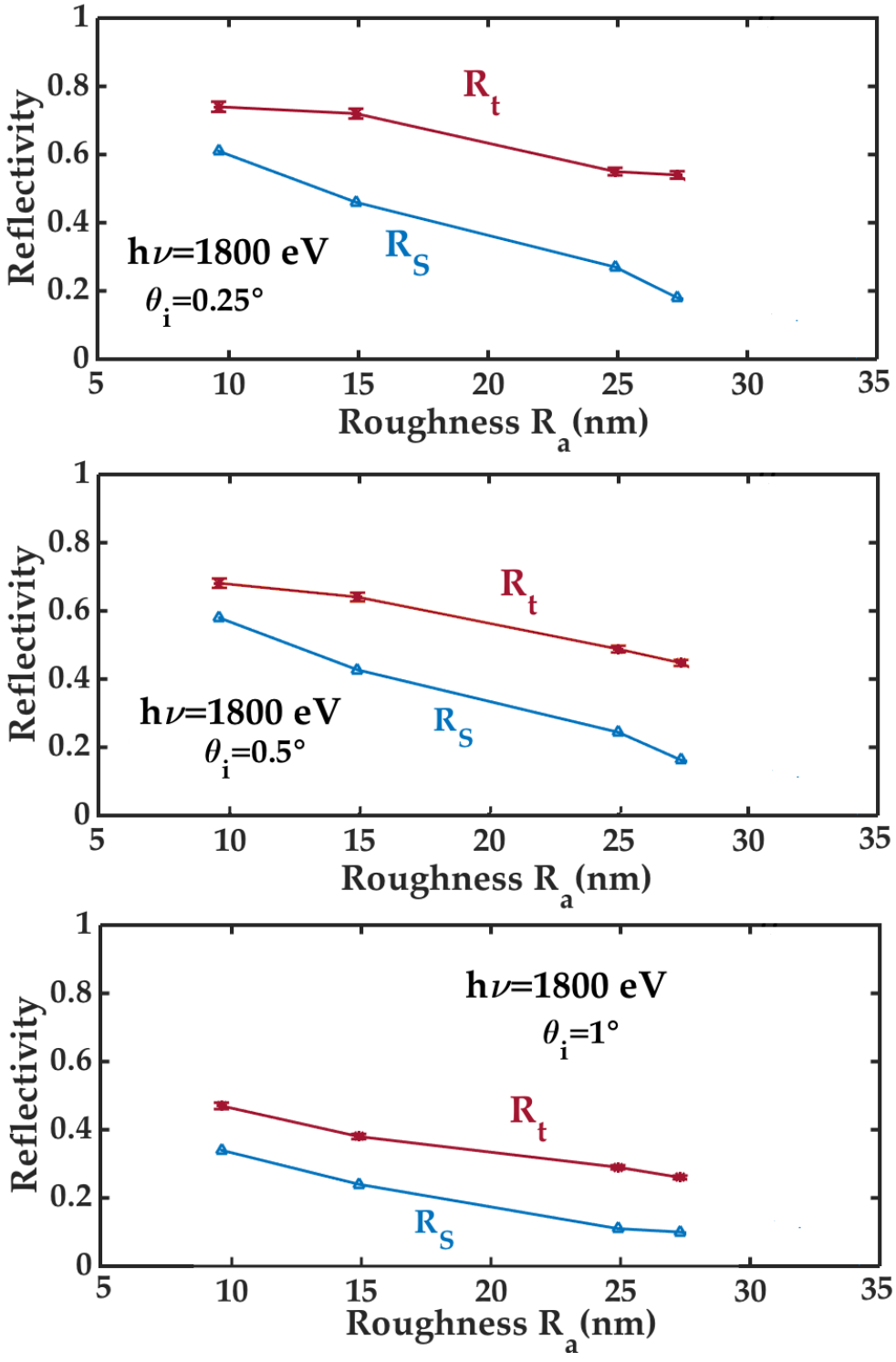

Figure 4.11: Comparison between Specular and Total Reflectivity as functions of roughness: at 1800 eV and incidence angle $\theta_i = 0.25°$ (top), $\theta_i = 0.5°$ (middle) and $\theta_i = 1°$.

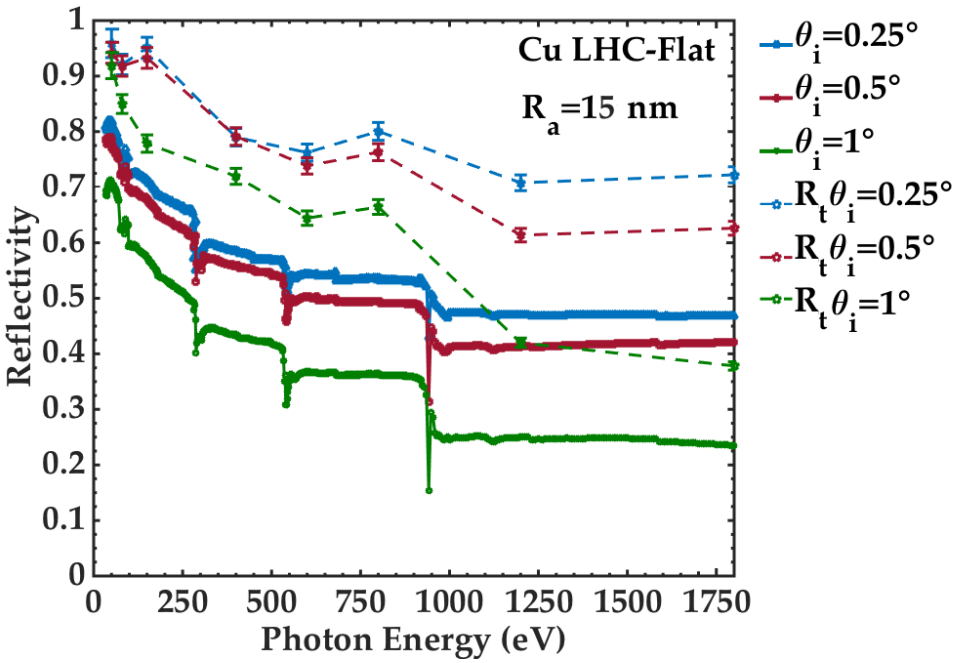

Figure 4.12: Specular and Total Reflectivity VS Photon Energy of LHC-Flat sample.

4.2 Flat Copper Samples with Carbon Coating

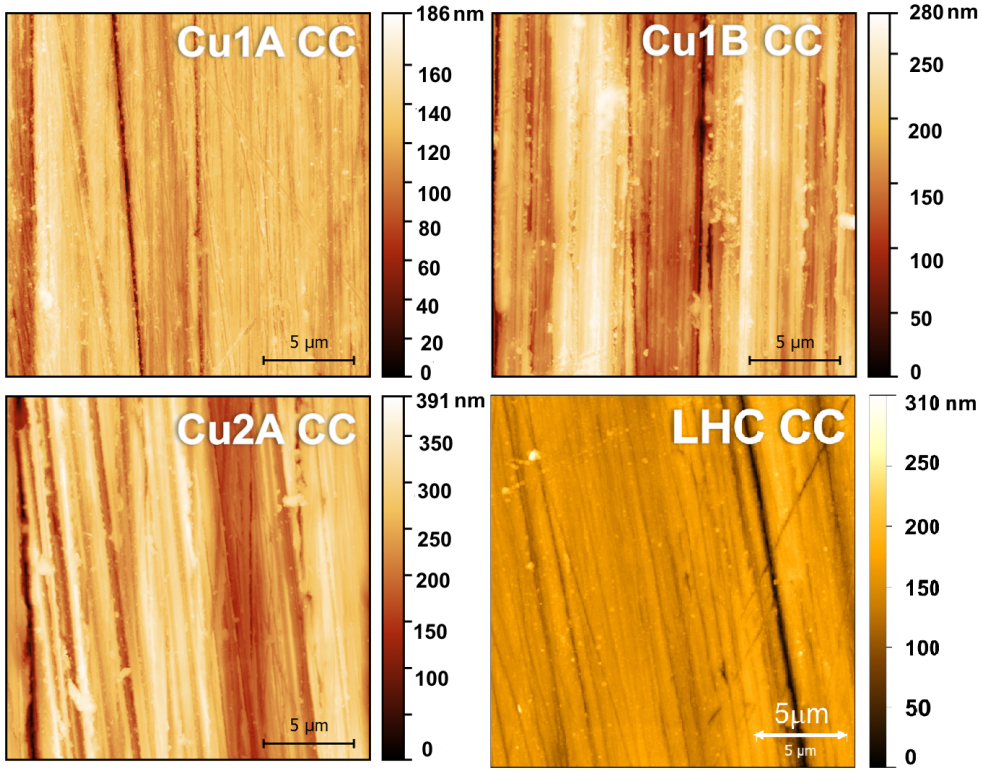

Figure 4.13: AFM measurements of Cu1A CC, Cu1B CC, LHC CC and Cu2A CC samples, clockwise direction.

As said before, Carbon coating (CC) of smooth vacuum chamber surfaces was suggested as a means to reduce the heat load in cold part of the machine, by forward reflecting most SR and its deposited power towards ad hoc designed room temperature absorbers [25]. For this reason we decided to study the same samples seen above, i.e. Cu 1A, 2A, 1B and the LHC-Flat samples, with a 50nm thick Carbon coating. The coating was done by magneto-sputtering.

Even in this case, we evaluate the roughness via AFM measurements at CNIS in Rome. The acquired data are shown in fig. 4.13. The edge profile between Carbon, on the left, and Copper, on the right, is reported in figure 4.14. Here we can see a quite homogeneous profile with a net step of ∼50 nm between the two materials. These data concern the LHC-Flat sample.

The measured values of roughness are reported in tab. 4.4. The coating process increased the roughness for each sample.

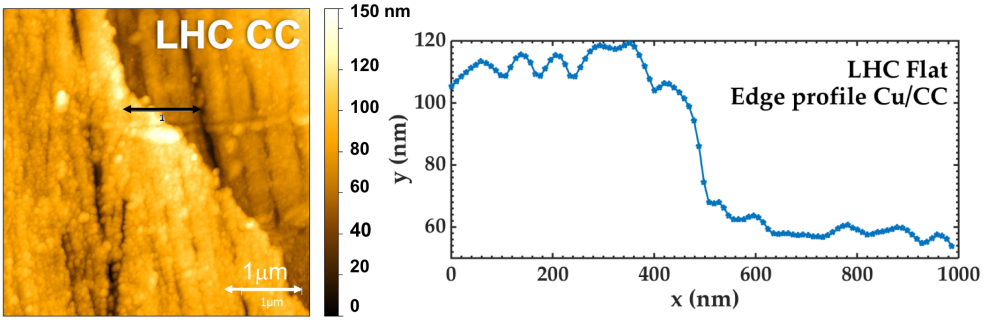

Figure 4.14: AFM measurement of CC/Cu edge of LHC-Flat sample with carbon coating.

.

Table 4.4: The flat copper samples with carbon coating, surface treatments and roughness

Sample	Material	Surface treatment	Roughness (nm)
LHC CC	C on Cu	magneto-sputtering coating	20
Cu1A CC	C on Cu	magneto-sputtering coating	13
Cu2A CC	C on Cu	magneto-sputtering coating	31
Cu1B CC	C on Cu	magneto-sputtering coating	29

Also in this case we performed Reflectivity simulations with REFLEC. The calculations are shown in fig. 4.15. The simulations show that we expect an high reflectivity above K-edge of Carbon (at 280 eV), as discussed in previous chapter. There will be also a clear decreasing of reflectivity at incidence angle $\theta_i = 1°$. This effect is due to the achievement of the critical angle.

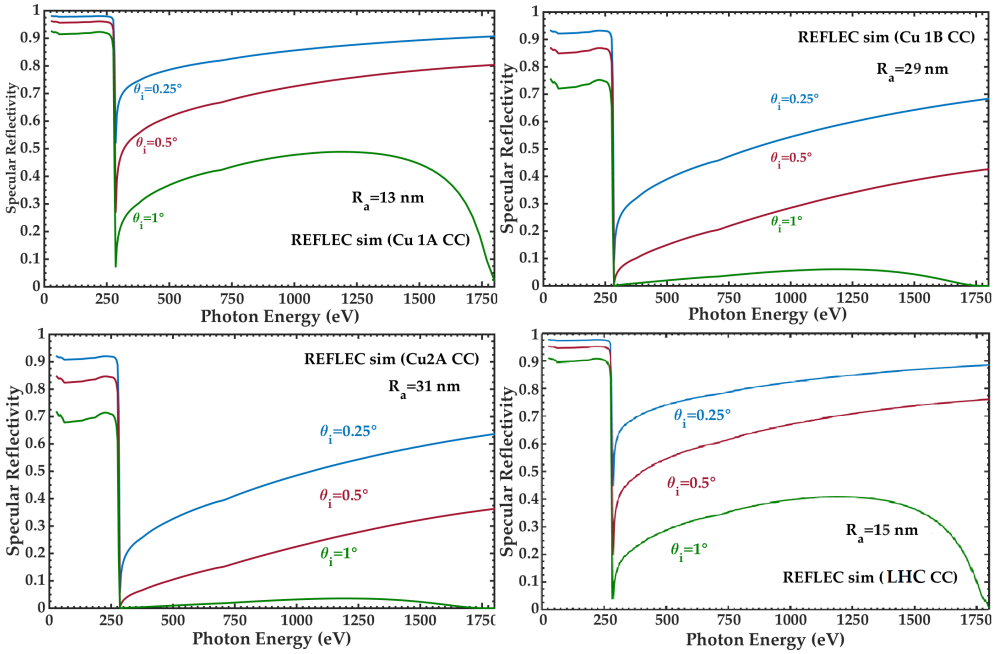

Figure 4.15: REFLEC simulations of Specular reflectivity VS Photon Energy at three incidence angle for a Carbon mirror with the Cu 1A CC, Cu 1B CC, LHC CC and Cu 2A CC roughness, clockwise direction.

In chapter 2, we have seen that X-ray refractive index is slightly lower than one and it is usually written like: $n(\lambda) = 1 - \delta - ik$. Far above the atomic resonance frequency, delta, i.e. the real part of refractive index, can be given by:

$$\delta = \frac{r_0 \lambda^2 n_e}{2\pi} \tag{4.1}$$

where r_0 is the classical electron radius, λ is the X-ray wavelength, and n_e is the electron density.

The critical angle θ_c is defined as the angle such that for all incidence angles below its value the incident wave is reflected and the transmitted wave exponentially decays. In X-ray range critical angle is defined as [31]:

$$\theta_c = \sqrt{2\delta} = \sqrt{\frac{r_0}{\pi}} \times \lambda \times \sqrt{\rho} \tag{4.2}$$

Typically $\theta_c \sim 0.1 \div 0.5$, it depends on λ's value and material. In our case for $\theta_i = 1°$ the reflected component decreases and the light penetrates mostly in the sample. For C and the very low angle of incidence in FCC-hh ($\theta_i = 0.07°$), it occurs at photon energies higher than 24 keV, which are well above the machine critical energy.

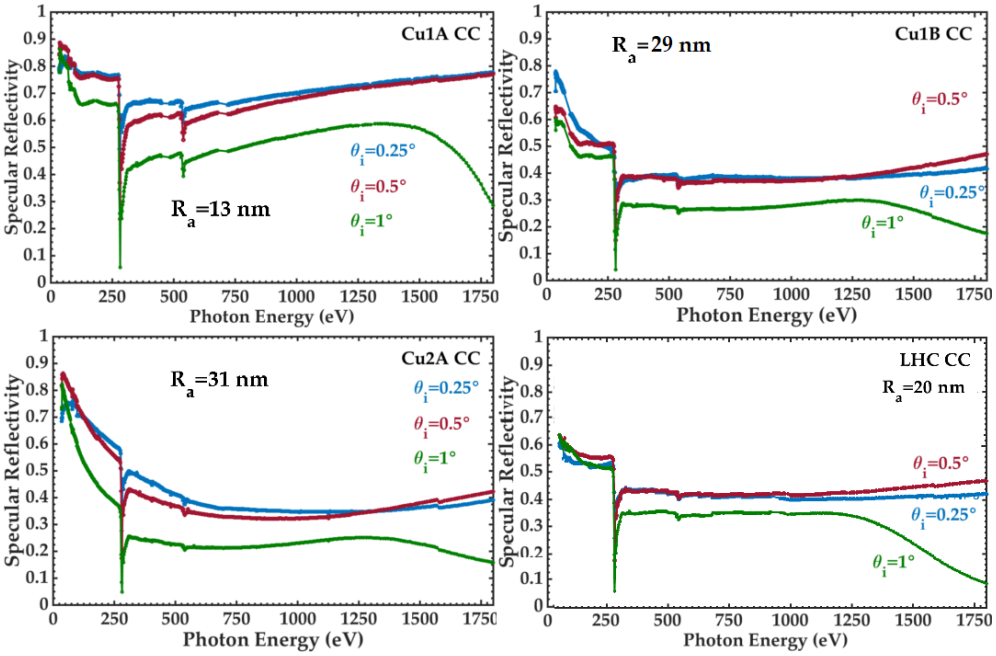

Figure 4.16: Specular Reflectivity VS Photon Energy at three different incidence angles of Cu1A CC, Cu1B CC, LHC CC and Cu2A CC sample, clockwise direction.

In fig. 4.16 the experimental data are shown. Looking at these data we make the following considerations:

- all samples increase high energy Specular Reflectivity;
- in $\theta_i = 1°$ data Reflectivity drops down;
- O-K absorption edge, i.e. Oxygen presence;
- all samples do not show the Cu-L_{2-3} absorption edge;
- for all samples the Specular Reflectivity profiles become very similar for the $\theta_i = 0.25°$ and $\theta_i = 0.5°$.

The first point confirms the possibility to increase reflectivity in order to optimize the heat load dissipation process, how proposed in [25]; this is true provided that avoiding an excessive increase in roughness through the coating process. For identical experimental conditions, in fact, the Specular Reflectivity is enhanced for the coated samples; however, this behaviour can be somehow compensated by an increase in roughness. In fig. 4.17 we can see an example of what has been said, i.e. the profile variation of Specular Reflectivity before and after the coating process for two different samples. After the coating process roughness has increased both in LHC-Flat and in Cu1B. In the case of Cu1B the increase in roughness after the coating process is lower than LHC-Flat case, and this

implies an increase in Specular Reflectivity at high energies (above 1500 eV). In any case the carbon coating increase the Total Reflectivity.

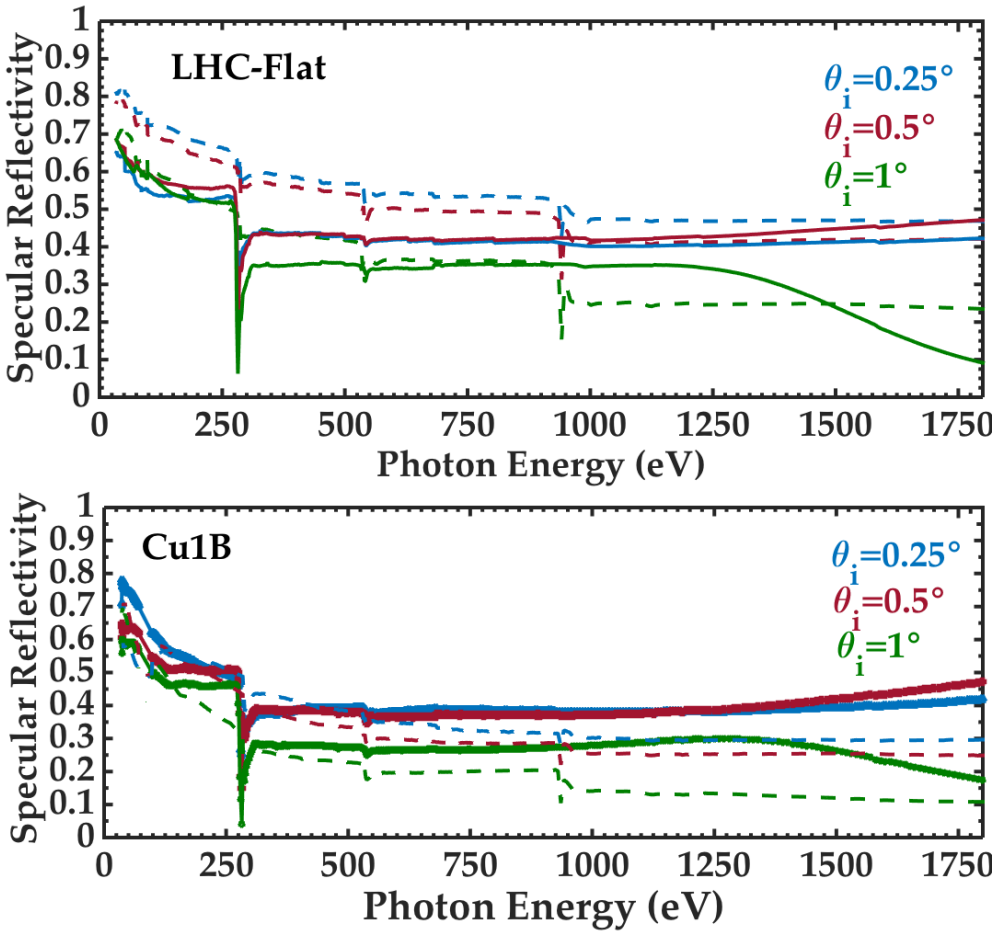

Figure 4.17: Specular Reflectivity VS Photon Energy of LHC-Flat (top panel) and Cu1B (bottom panel) samples, with (full lines) and without (dashed lines) Carbon coating at three incidence angle.

In fig.4.18 we can see Specular and Total Reflectivity VS Reflection angle θ_r at 1800 eV and $\theta_i = 0.25°$. Data concern LHC-Flat (left panel) and Cu1B (right panel) samples, with (full lines) and without (dashed lines) Carbon coating at three incidence angle. Dotted lines indicate the acceptance of diode used in Specular Reflectivity measurements. The values of Total Reflectivity can be calculated by integration.

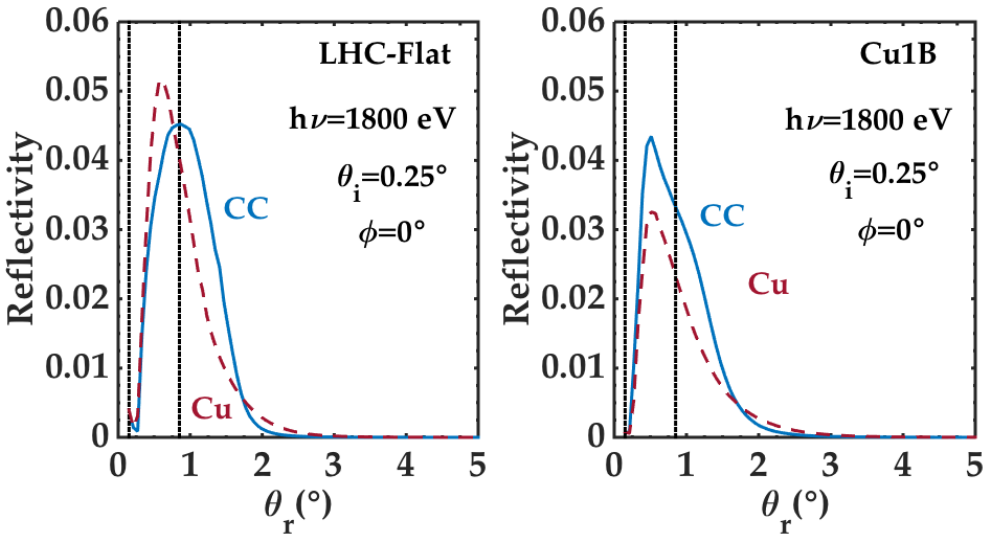

Figure 4.18: Specular and Total Reflectivity VS Reflection angle at 1800 eV and $\theta_i = 0.25°$. Data concern LHC-Flat (left panel) and Cu1B (right panel) samples, with (full lines) and without (dashed lines) Carbon coating at three incidence angle. Dotted lines indicate the acceptance of diode used in Specular Reflectivity measurements.

In fig. 4.19 Photo Yield data VS photon energy are shown. In fig. 4.20 the comparison between PY before and after CC is reported. The Carbon coating significantly reduces the PY, and this is a consequence of Reflectivity increase. Also the disappearance of Cu-L_{2-3} absorption edge, due to the coverage, reduce the photoelectrons production. The further reduction for $\theta_i = 1°$ measurements at high energies can be ascribed to a greater penetration of the radiation inside the material and, consequently, to the generation of photoelectrons far from the interface.

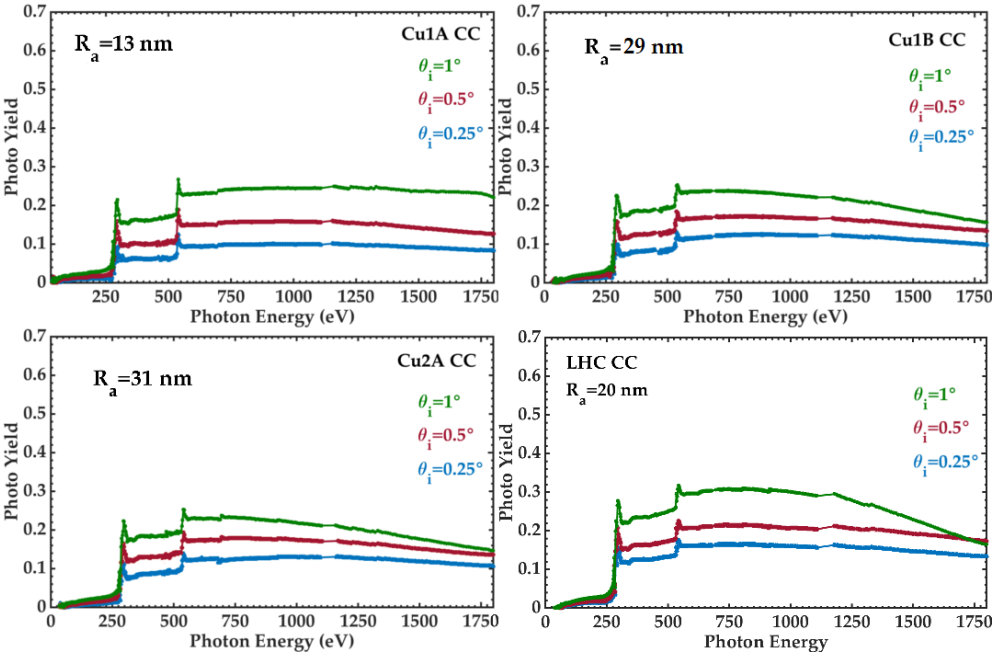

Figure 4.19: Photo Yield VS Photon Energy at three different incidence angles of Cu1A CC, Cu1B CC, LHC CC and LHC-Flat CC sample, clockwise direction.

In fig. 4.21 Specular Reflectivity as a function of incidence angle at seven photon energies is shown. Peculiarity of these samples is the behaviour of 1200 eV measurements. The faster drop down, with respect to other energies, is due to critical angle achievement. In fig. 4.22 Photo Yield VS incidence angle at seven photon energies is shown.

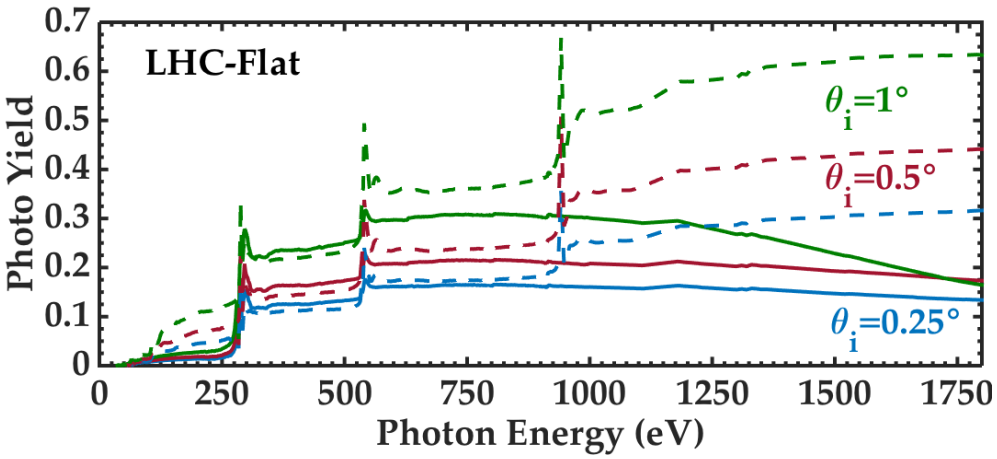

Figure 4.20: Photo Yield VS Photon Energy of LHC-Flat sample, with (full lines) and without (dashed lines) Carbon coating at three incidence angle.

The total Reflectivity of LHC CC sample evaluated at eight photon energies is reported in tab. 4.5. The same data and Specular Reflectivity values are shown in fig. 4.23 for the comparison. Although Specular Reflectivity at $\theta_i = 0.5°$, at high energy, is higher than $\theta_i = 0.25°$ data, this is not valid for Total Reflectivity measurements. In this case the usual trend is re-established.

Photon energy hν(eV)	**Total Reflec.** $\theta_i = 0.25°$ ($\pm$5%)	**Specular Reflec.** $\theta_i = 0.25°$ ($\pm$2%)	**Total Reflec.** $\theta_i = 0.5°$ ($\pm$5%)	**Specular Reflec.** $\theta_i = 0.5°$ ($\pm$2%)	**Total Reflec.** $\theta_i = 1°$ ($\pm$5%)	**Specular Reflec.** $\theta_i = 1°$ ($\pm$2%)
1800	0.79	0.42	0.67	0.47	0.45	0.09
1200	0.80	0.43	0.75	0.41	0.51	0.35
800	0.80	0.42	0.76	0.42	0.65	0.35
600	0.78	0.42	0.74	0.42	0.64	0.34
400	0.80	0.44	0.71	0.43	0.63	0.35
150	0.95	0.54	0.91	0.54	0.88	0.54
80	0.93	0.56	0.93	0.61	0.88	0.61
50	0.98	0.64	0.93	0.66	0.91	0.64

Table 4.5: Comparison between Specular and Total Reflectivity of LHC CC sample at eight different values of photon energy.

Lastly, in fig. 4.24 there is the comparison between Specular and Total Reflectivity as functions of roughness for Carbon coated samples: at 1800 eV and incidence angle $\theta_i = 0.25°$ (top), $\theta_i = 0.5°$ (middle) and $\theta_i = 1°$. Also in this case, like for pure Copper samples, the gap between R and R_t increases with increasing roughness. The same data are reported also in tab. 4.6.

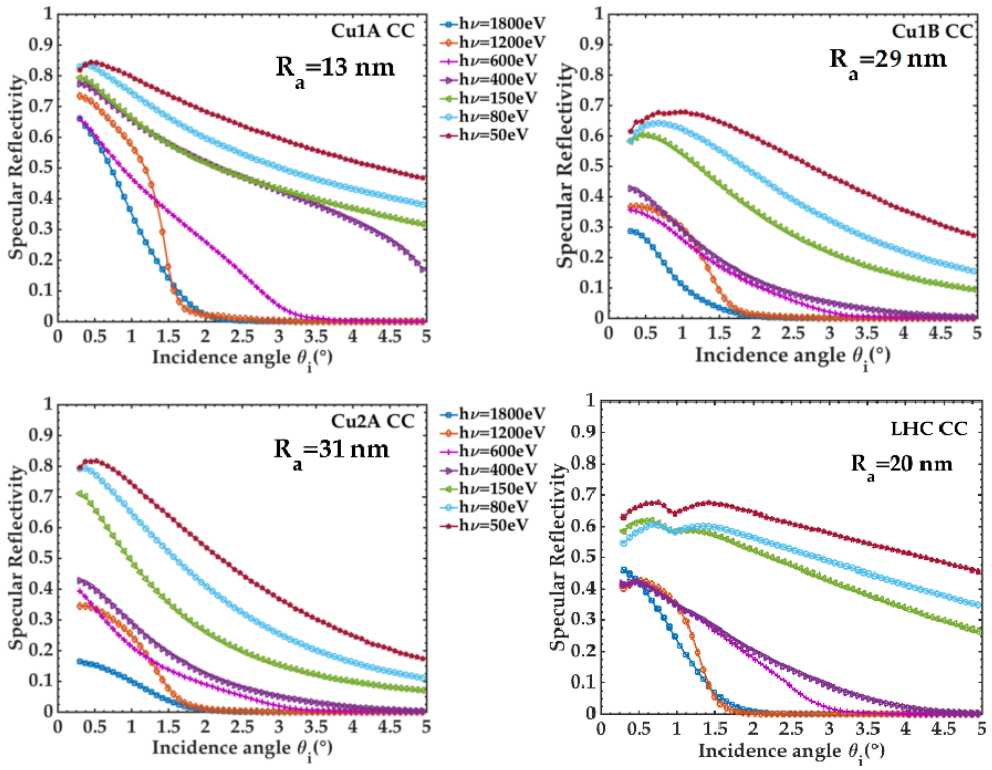

Figure 4.21: Specular Reflectivity VS incidence at seven different photon energies of Cu1A CC, Cu1B CC, LHC CC and Cu2A CC sample, clockwise direction.

Roughness R_a (nm) (1800 eV) Carbon Coated	**Total Reflec.** $\theta_i = 0.25°$ (±5%)	**Specular Reflec.** $\theta_i = 0.25°$ (±2%)	**Total Reflec.** $\theta_i = 0.5°$ (±5%)	**Specular Reflec.** $\theta_i = 0.5°$ (±2%)	**Total Reflec.** $\theta_i = 1°$ (±5%)	**Specular Reflec.** $\theta_i = 1°$ (±2%)
13	0.92	0.77	0.90	0.70	0.70	0.59
20	0.79	0.422	0.67	0.47	0.45	0.09
29	0.71	0.33	0.68	0.42	0.34	0.18
31	0.71	0.31	0.68	0.42	0.29	0.16

Table 4.6: Comparison between Specular and Total Reflectivity of the four samples for three different incidence angle (Photon energy 1800 eV).

However, Total Reflectivity in coated samples is always higher than in uncoated samples (see fig. 4.25). The increasing of R_t after the coating process is somewhat partially reduced by an increase in the surface roughness, that is due to the coating process itself. With the aim of maximizing the increase in reflectivity, the coating process should be optimized in order to limit as much as possible the increase in roughness.

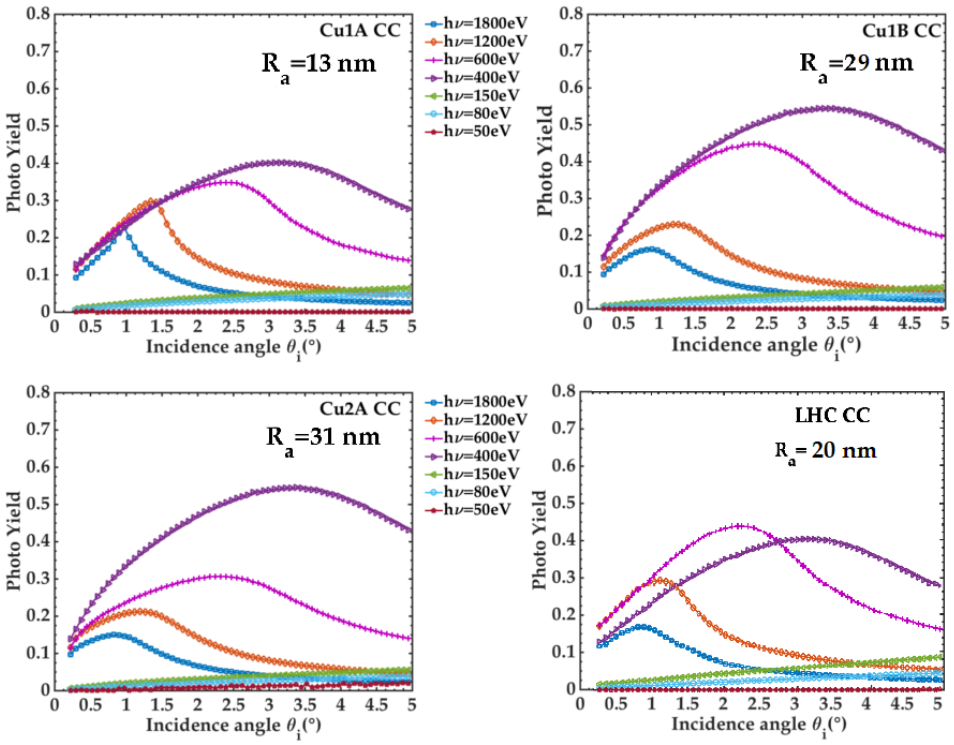

Figure 4.22: Photo Yield VS incidence at seven different photon energies of Cu1A CC, Cu1B CC, LHC CC and Cu 2A CC sample, clockwise direction.

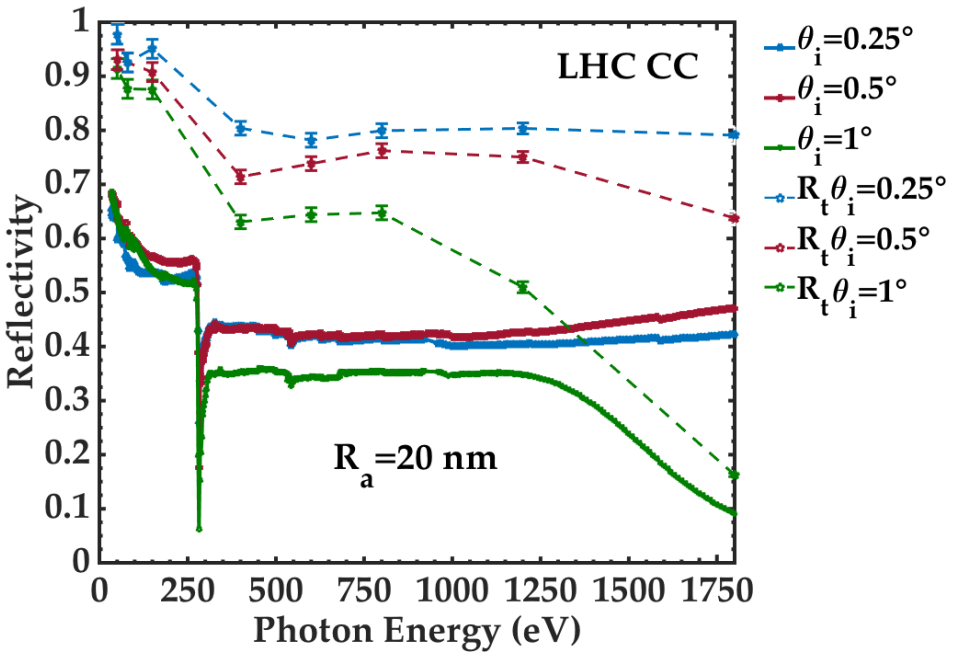

Figure 4.23: Specular and Total Reflectivity VS Photon Energy of LHC-Flat sample.

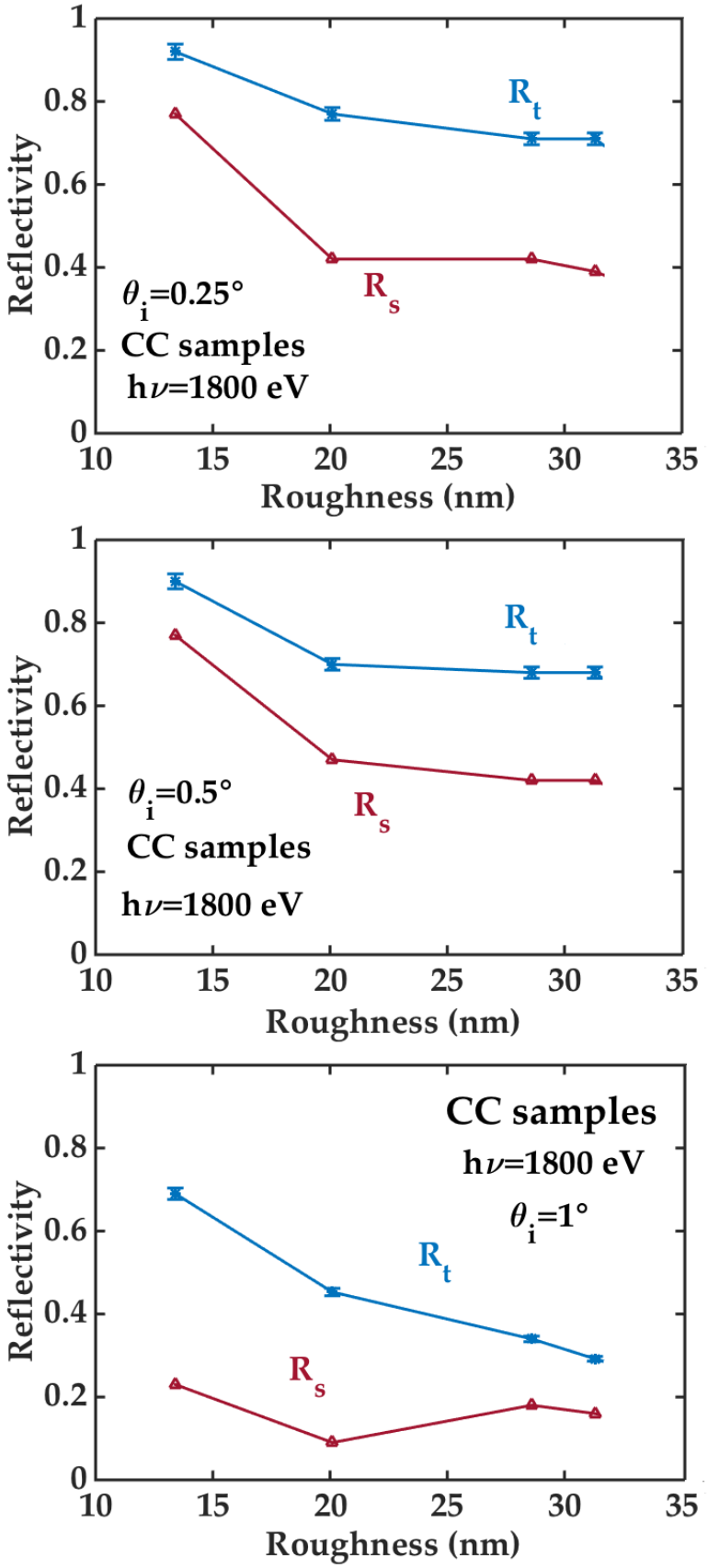

Figure 4.24: Comparison between Specular and Total Reflectivity as functions of roughness for Carbon coated samples: at 1800 eV and incidence angle $\theta_i = 0.25^\circ$ (top), $\theta_i = 0.5^\circ$ (middle) and $\theta_i = 1^\circ$.

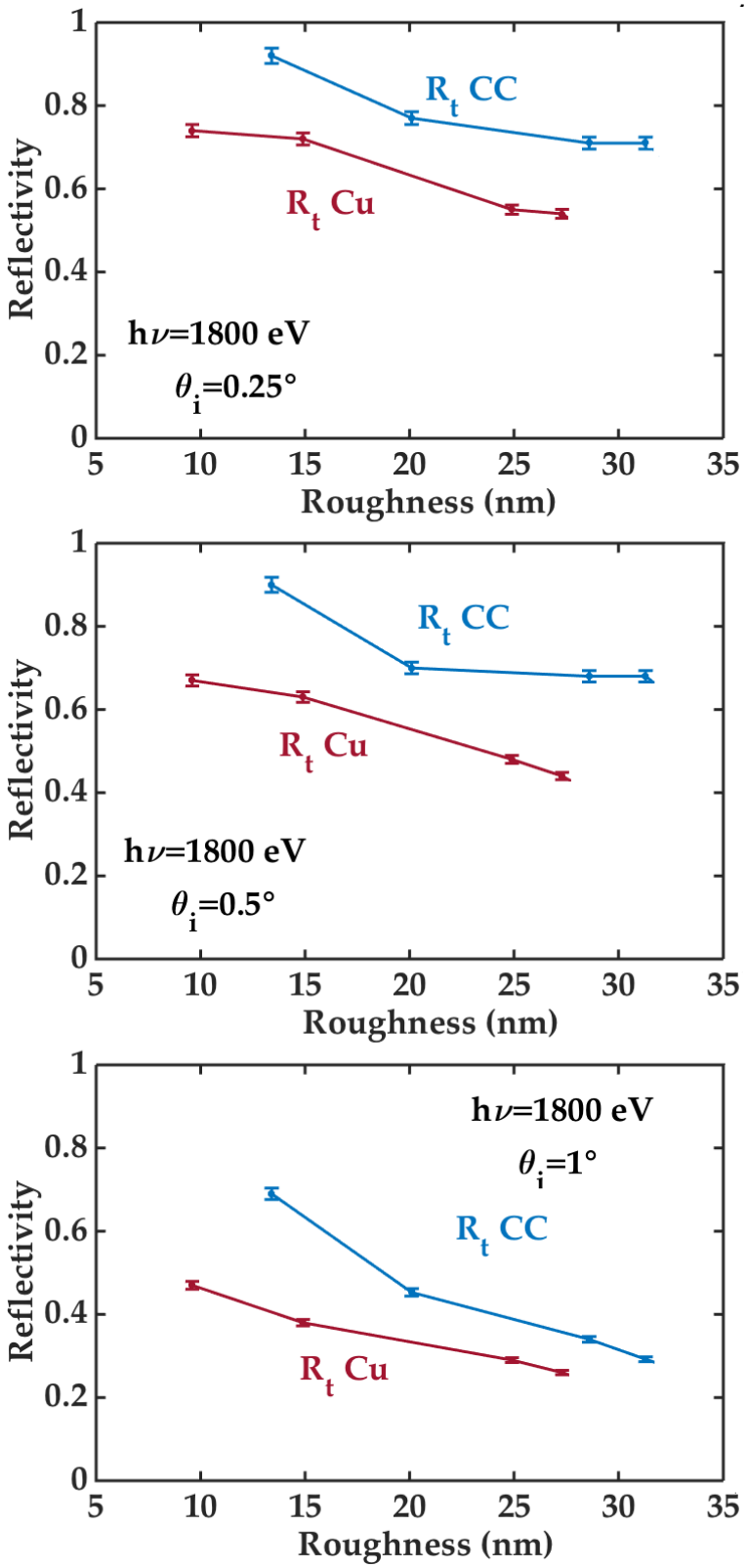

Figure 4.25: Comparison between Total Reflectivity with and without Carbon coating as functions of roughness: at 1800 eV and incidence angle $\theta_i = 0.25°$ (top), $\theta_i = 0.5°$ (middle) and $\theta_i = 1°$.

4.3 LHC Beam Screen: Saw-Tooth

The Beam Screen of LHC is equipped with Saw-Tooth structure to reduce the SR Reflectivity and, consequently, electron cloud effect, as described in chapter 2. In fig.4.26 a picture of LHC BS (panel (a)), Saw-Tooth SAM image (panel (b)) and measured sample on the set-up holder (panel (c)) are shown.

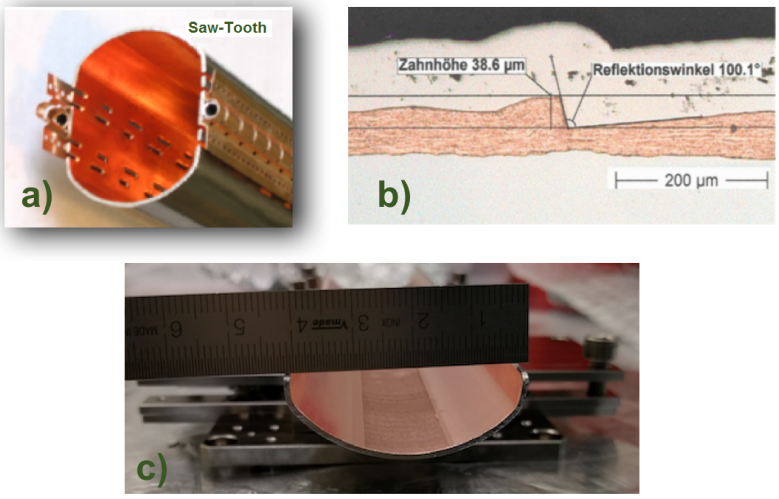

Figure 4.26: (a)LHC Beam Screen, the Saw-Tooth surface in this picture is on the top, (b)Saw-Tooth design optimized to reduce the e-cloud effect, (c) measured sample on the holder.

Specular Reflectivity data VS Photon Energy measured for LHC Saw-Tooth are reported in fig.4.27. Photo Yield behaviour VS Photon Energy is shown in fig.4.28. We can see only a drop in reflectivity and three peaks in photo yield. These correspond to the Cu-L_{2-3} absorption edge (930-950 eV). Comparing these two figures with data reported in fig.4.6, where we have the analogous graphs for LHC Flat sample, we can see how the ST structure drastically reduces reflectivity by more than two order of magnitude. This phenomenon could be expected extrapolating the reduction of Specular Reflectivity with R_a measured from the flat Cu surfaces. In fact, the ST-LHC sample could be certainly considered as a sample with a significant ($\approx 40\mu m$) roughness. At very grazing incidence angles the residual Specular Reflectivity may be attributed to the "saw tooth" crests which are rounded by production process.

Also the PY is reduced, but only by a factor 10, and shows the same peaks of the flat samples, that we have seen are due to C, O and Cu absorption edges. In fact, although in Specular Reflectivity behaviour of LHC-ST sample contaminants edges are difficult to see 4.27; however, their presence is confirmed by photo yield peaks (see fig.4.28).

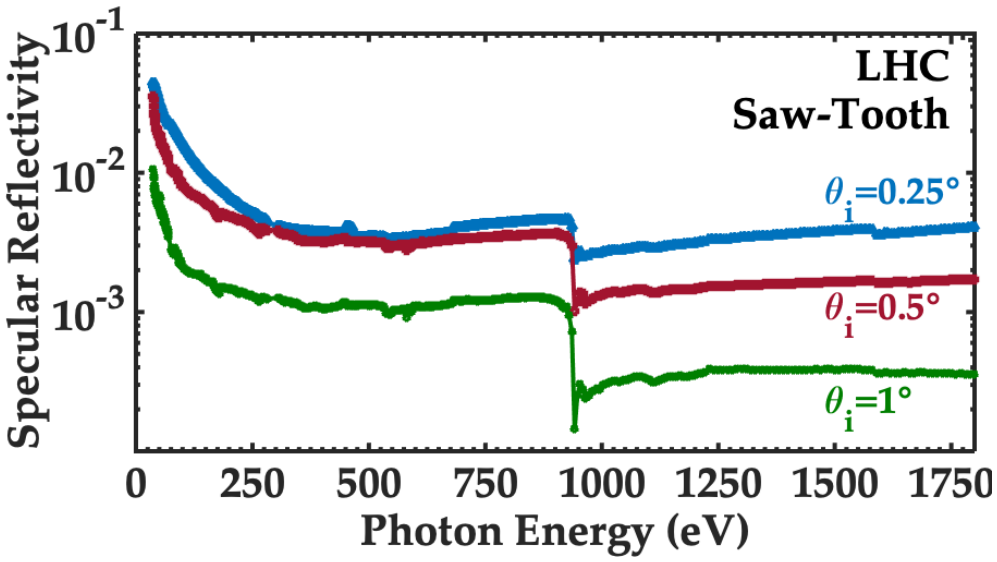

Figure 4.27: Specular Reflectivity Vs Photon Energy (eV) of LHC-ST copper sample.

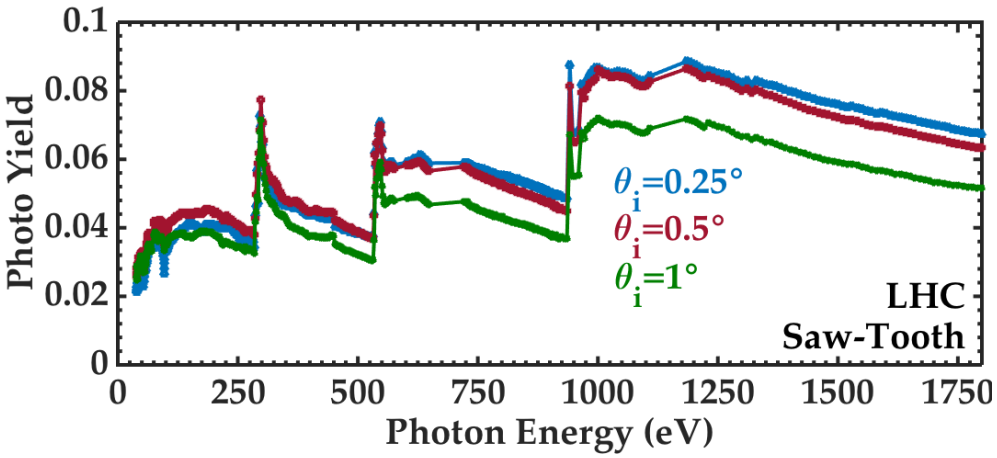

Figure 4.28: Photo Yield Vs Photon Energy (eV) of LHC ST sample.

For geometrically modified surface samples, like LHC Saw-Tooth and LASE, we decided to study the Specular Reflectivity and Photo Yield VS incidence angle in a larger range: $0 \div 50°$. The data are reported in fig. 4.29 and fig. 4.30, respectively. In this case Specular Reflectivity is very low, as expected. The PY behaviour is very interesting because of the presence of a double peak. This effect can be ascribed to the different penetration of photons inside the sample because of the teeth.

Comparison between Specular and Total Reflectivity data of LHC Saw-Tooth sample at eight different values of photon energy are reported in tab. 4.7 and fig. 4.31. The significant presence of scattered light at

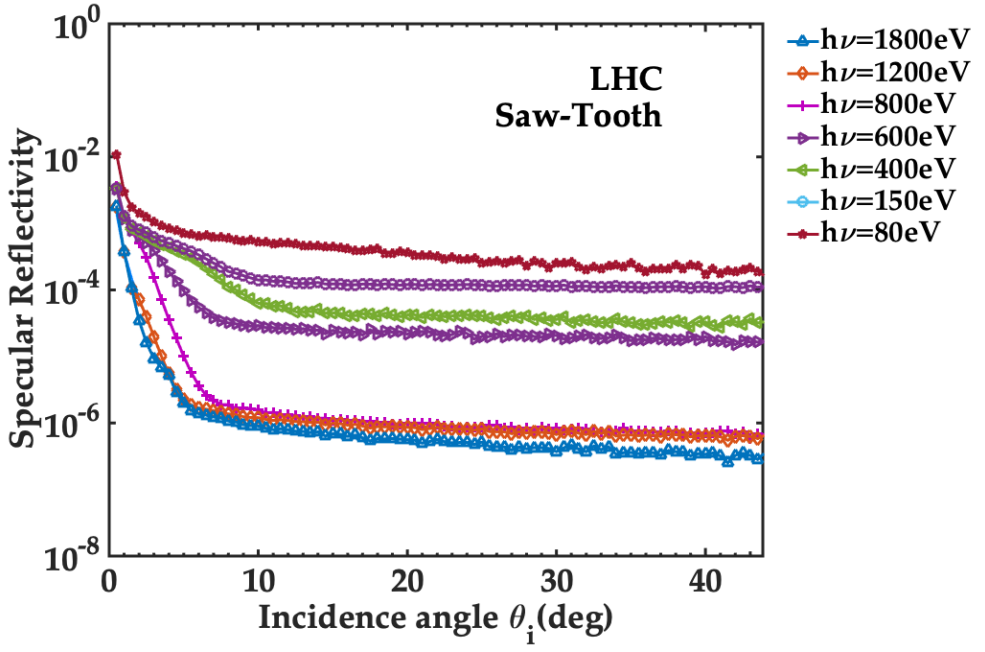

Figure 4.29: Specular and Total Reflectivity Vs incidence angle of LHC ST sample.

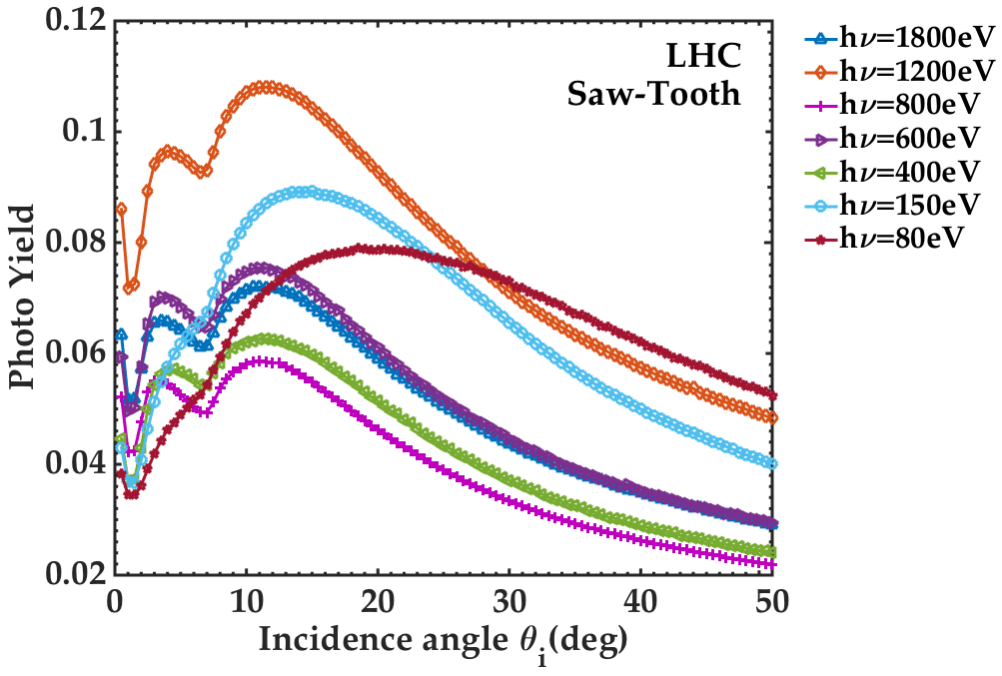

Figure 4.30: Photo Yield Vs incidence angle of LASE sample.

high angles and our limited solid angle ($3.5° \times 175°$) suggest to consider the measured R_t with an increased error bar with respect to the one assigned for the flat Cu samples. It has to be noticed here, that the intrinsic design and structure of the saw tooth is macroscopically modified only in the direction perpendicular to the scattering plane $\theta_i \cdot \theta_r$. Our detector can cover most of this region in its quasi-complete θ_r angular scans with the noticeable exception of the quasi-normal reflection angles around $170° < \theta_r < 180°$. Such near normal reflectivity should occur when light hits the quasi-perpendicular tooth and cannot be measured since, if we push the detector over $\theta_r = 175°$, the diode support frame would block the direct beam impinging on the surface. Other experiments [67] and basic optical considerations show that quasi normal reflectivity may be of importance at very low photon energies, below 35 eV. Such a low energy is below the energy range used to perform the measurements shown here. For these reasons, we conservatively estimate the relative error on the LHC-ST total Reflectivity to be $\sim 10\%$.

Photon energy hν(eV)	**Total Reflec.** $\theta_i = 0.25°$ ($\pm$10%)	**Specular Reflec.** $\theta_i = 0.25°$ ($\pm$2%)	**Total Reflec.** $\theta_i = 0.5°$ ($\pm$10%)	**Specular Reflec.** $\theta_i = 0.5°$ ($\pm$2%)	**Total Reflec.** $\theta_i = 1°$ ($\pm$10%)	**Specular Reflec.** $\theta_i = 1°$ ($\pm$2%)
1800	0.054	0.0040	0.007	0.0017	0.001	0.0003
1200	0.050	0.0030	0.006	0.0015	0.002	0.0003
800	0.068	0.0044	0.017	0.0035	0.009	0.0013
600	0.085	0.0035	0.031	0.003	0.014	0.0011
400	0.094	0.0038	0.026	0.003	0.013	0.0014
150	0.102	0.0096	0.047	0.006	0.029	0.0017
80	0.108	0.021	0.030	0.010	0.016	0.0026
50	0.102	0.032	0.034	0.019	0.015	0.006

Table 4.7: Comparison between Specular and Total Reflectivity of LHC Saw-Tooth sample at eight different values of photon energy.

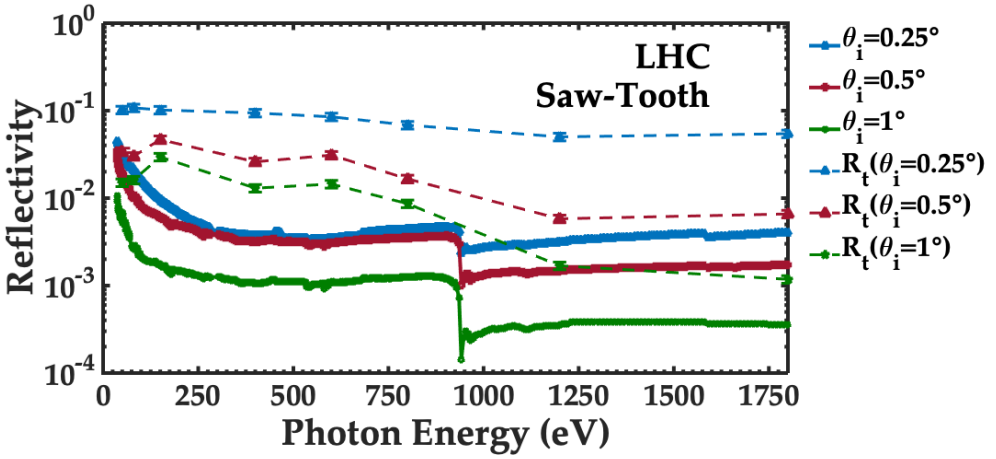

Figure 4.31: Comparison between Specular and Total Reflectivity Vs Photon Energy (eV) of LHC-ST sample.

4.4 Laser Treated sample

The last copper sample studied was made by the Science & Technology Facility Council (STFC) and it was obtained by Laser Ablation Surface Engineering (LASE). This sample is a candidate of the Beam Screen in FCC-hh because of its low Secondary Electron Yield (SEY) due to its structure.

Specular Reflectivity Vs Photon Energy measured for LASE is reported in fig.4.32. Photo Yield behaviour Vs Photon Energy is shown in fig.4.33. As expected the Laser treatment drastically reduces both reflectivity and photo yield.

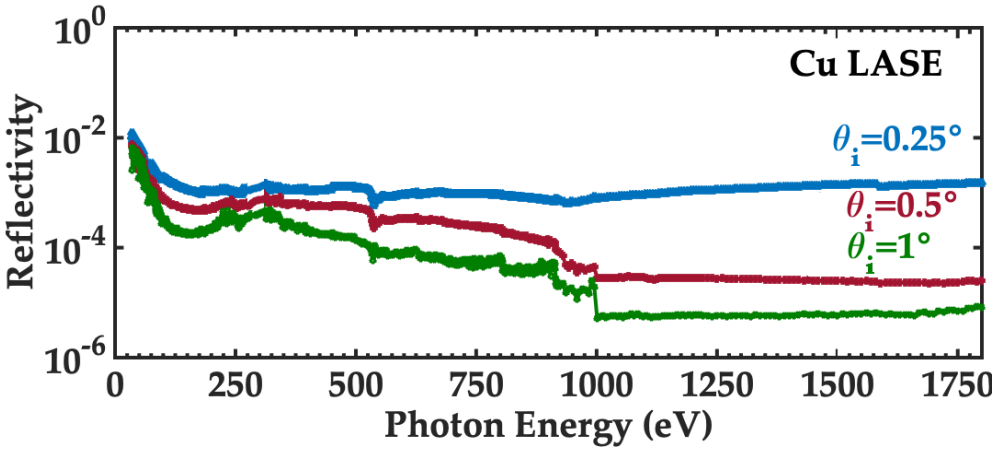

Figure 4.32: Specular Reflectivity Vs Photon Energy (eV) of laser treated copper sample.

In the LASE sample we see only Oxygen K edge as surface contaminant

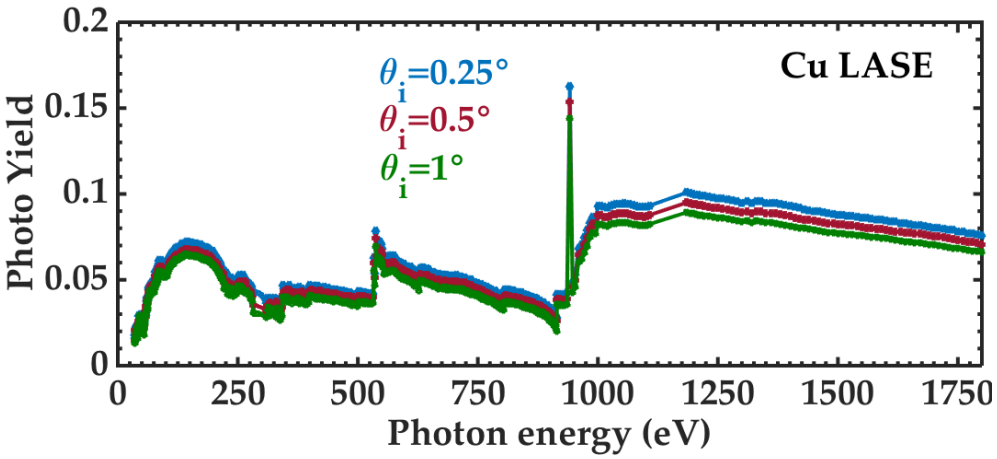

Figure 4.33: Photo Yield Vs Photon Energy (eV) of laser treated copper sample.

(fig. 4.32), indicating no presence of Carbon on the surface, as it was seen by XPS spectra previously [98]. Specular Reflectivity and Photo Yield

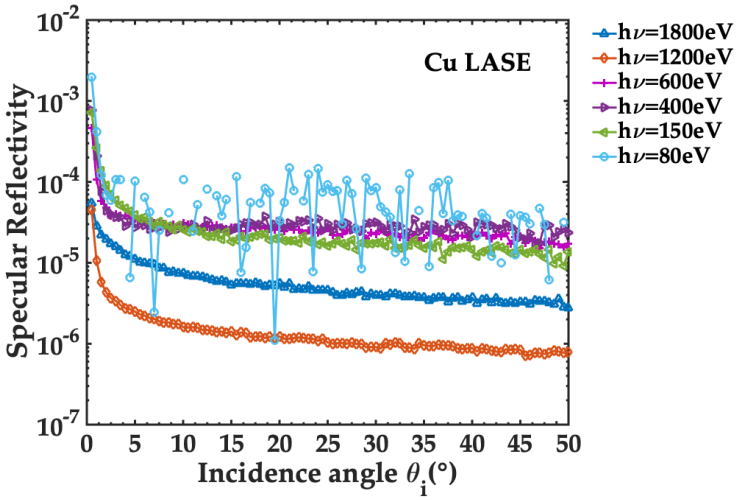

Figure 4.34: Specular and Total Reflectivity Vs incidence angle of LASE sample.

Vs incidence angle are reported in fig.4.34 and fig.4.35, respectively. In these cases, we can see no significant variations in Specular Reflectivity for incidence angle greater than 2 degrees. Photo Yield is quite constant too. This effect can be explained considering the peculiarity of the sample surface.

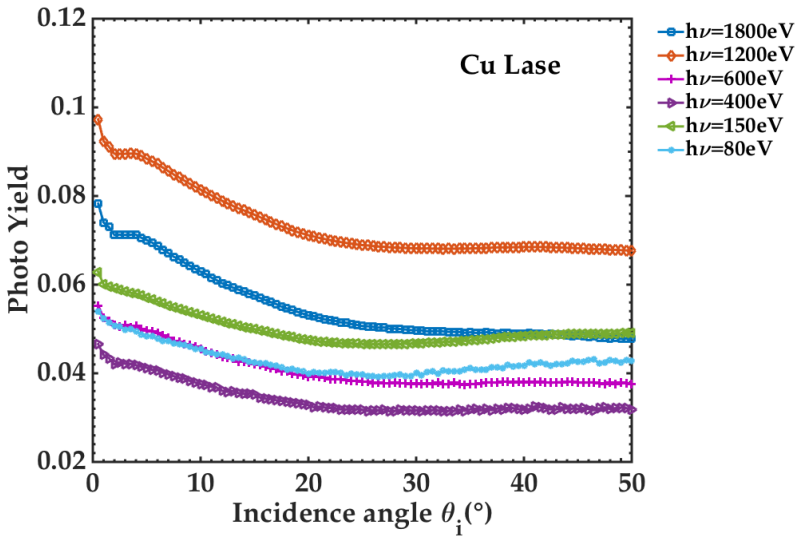

Figure 4.35: Photo Yield Vs incidence angle of LASE sample.

The Cu-L_{2-3} absorption is hard to see in Reflectivity, but it is evident in PY. The Carbon lack is also confirmed by the absence of C peak in the photo yield (fig. 4.33). The data in this range ($280 \div 308$ eV) are removed because there were some problems with the normalization due to the effect of the impinging flux from absorption of the Carbon layers present on beam line optics.

It is interesting to notice how the intrinsic nature of the surface structure significantly wash out most of the dependence on the angle of incidence θ_i both from the R signal and from the PY one, which stays nearly constant for the 3 small angle of incidence reported in fig.4.33. This feature is confirmed by the data reported in fig.4.35, where the LASE-Cu PY is reported at some selected photon energies and in a much wider θ_i interval.

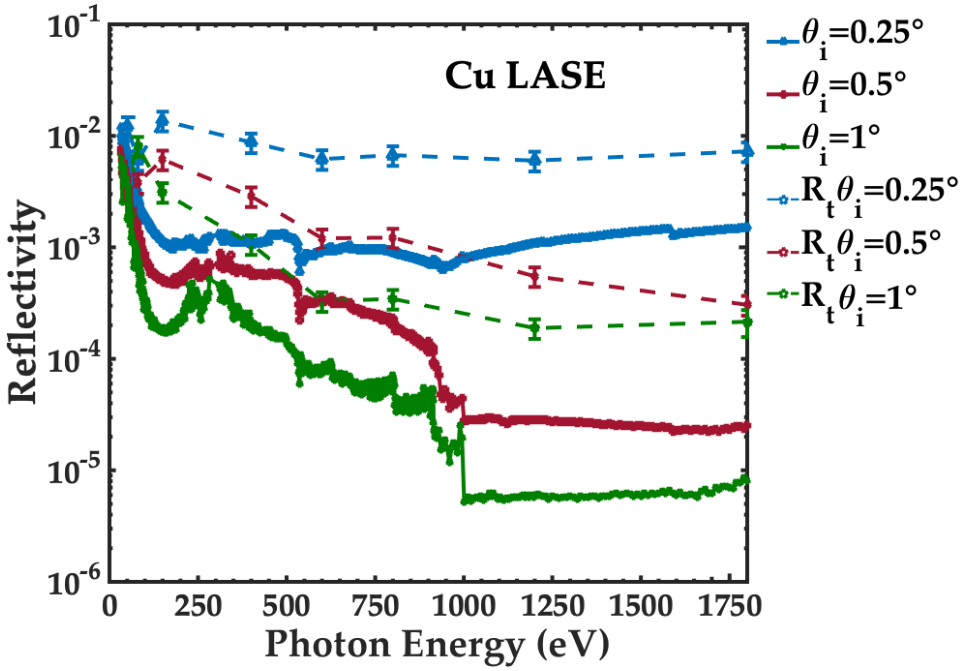

Figure 4.36: Comparison between Specular and Total Reflectivity Vs Photon Energy (eV) of LASE sample.

The values of Total Reflectivity for eight different photon energies of the sample are shown in the tab.4.8.

Photon energy hν(eV)	**Total Reflec.** $\theta_i = 0.25°$ ($\pm$20%)	**Specular Reflec.** $\theta_i = 0.25°$ ($\pm$2%)	**Total Reflec.** $\theta_i = 0.5°$ ($\pm$20%)	**Specular Reflec.** $\theta_i = 0.5°$ ($\pm$2%)	**Total Reflec.** $\theta_i = 1°$ ($\pm$20%)	**Specular Reflec.** $\theta_i = 1°$ ($\pm$2%)
1800	0.007	0.0015	0.0003	$2.5 \cdot 10^{-5}$	0.0003	$8.1 \cdot 10^{-6}$
1200	0.006	0.0011	0.0005	$2.8 \cdot 10^{-5}$	0.0002	$6.1 \cdot 10^{-6}$
800	0.007	0.0009	0.001	0.0002	0.0003	$5.3 \cdot 10^{-5}$
600	0.006	0.0009	0.001	0.0003	0.0003	$7.6 \cdot 10^{-5}$
400	0.009	0.001	0.003	0.0005	0.001	0.0002
150	0.014	0.001	0.006	0.0005	0.002	0.0002
80	0.011	0.003	0.004	0.001	0.008	0.0008
50	0.012	0.006	0.005	0.004	0.004	0.003

Table 4.8: Comparison between Specular and Total Reflectivity of LASE sample at eight different values of photon energy.

LASE intrinsic structure suggests that photons scattered at high angles from the geometrical reflection, may also be significantly distributed in the perpendicular direction to the scattering plane, i.e. at ϕ significantly

different from zero. As said, we can only scan over 3.5°. Therefore we could expect, for this class of samples, to loose a more significant contribution to R_t. For these reasons we estimate to have systematically underestimated Rt. We therefore assign a relative error on the Cu-LASE total reflectivity to be 20%. A comparison between Specular and Total Reflectivity for LASE sample is shown fig. 4.36. Also for this sample, R_t can be more than one order of magnitude larger than the measured Specular Reflectivity R and has to be carefully considered when analysing LASE behaviour under SR illumination.

The figures 4.37 and 4.38 can help to estimate the effects of geometrical modification on Specular Reflectivity and Photo Yield. Here we can see how, from Reflectivity point of view, the best choice seems to be LASE. However, if we see the Photo Yield there is no difference in Photo Yield between LHC-ST and LASE, excluding the absorption peak at 280 eV, due to the presence of carbon on LHC beam screen.

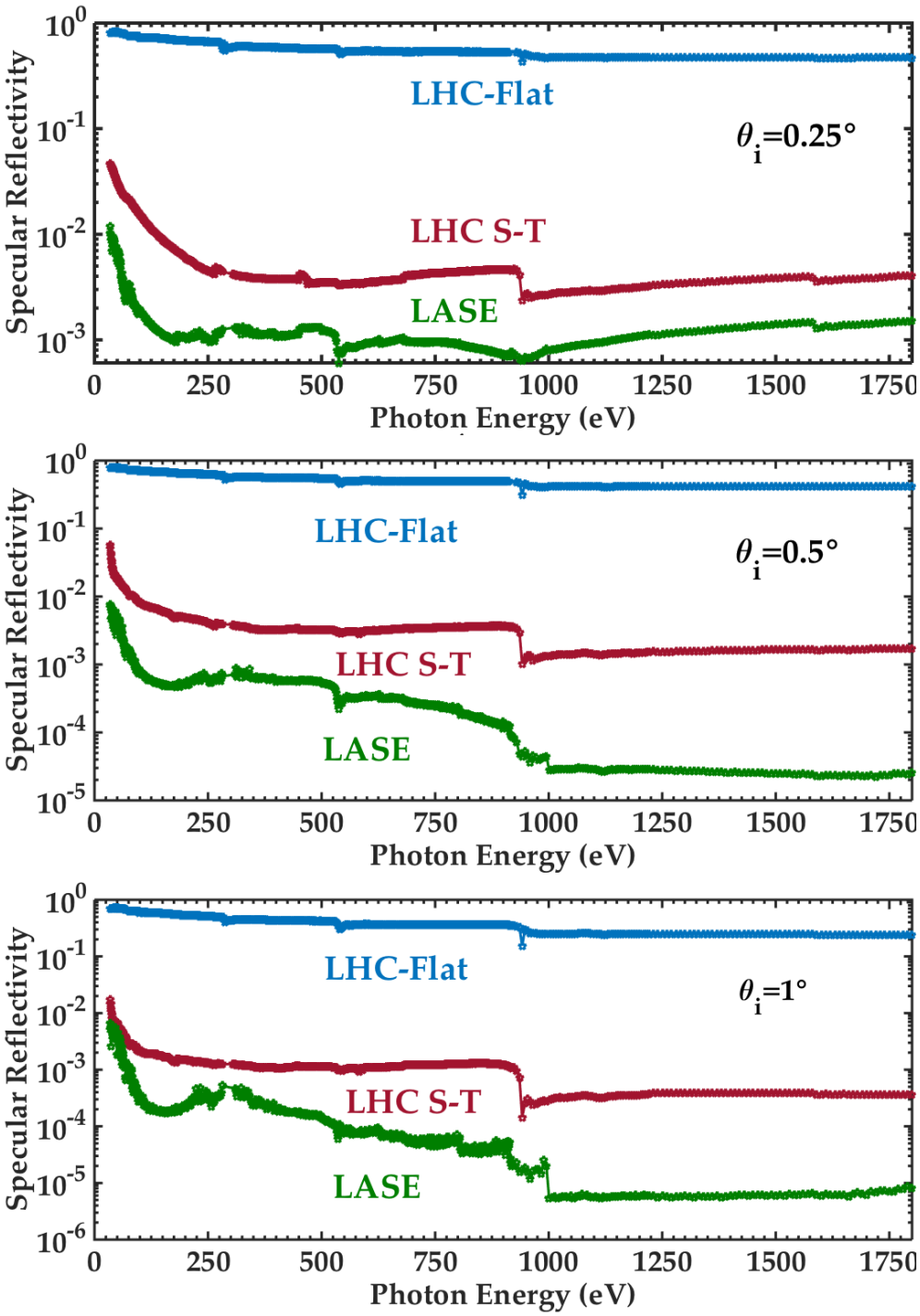

Figure 4.37: Specular Reflectivity Vs Photon Energy of LHC-Flat, LHC-ST and LASE samples for $\theta_i = 0.25°$ (top panel), $\theta_i = 0.5°$ (middle panel), and $\theta_i = 1°$ (bottom panel) incidence angle.

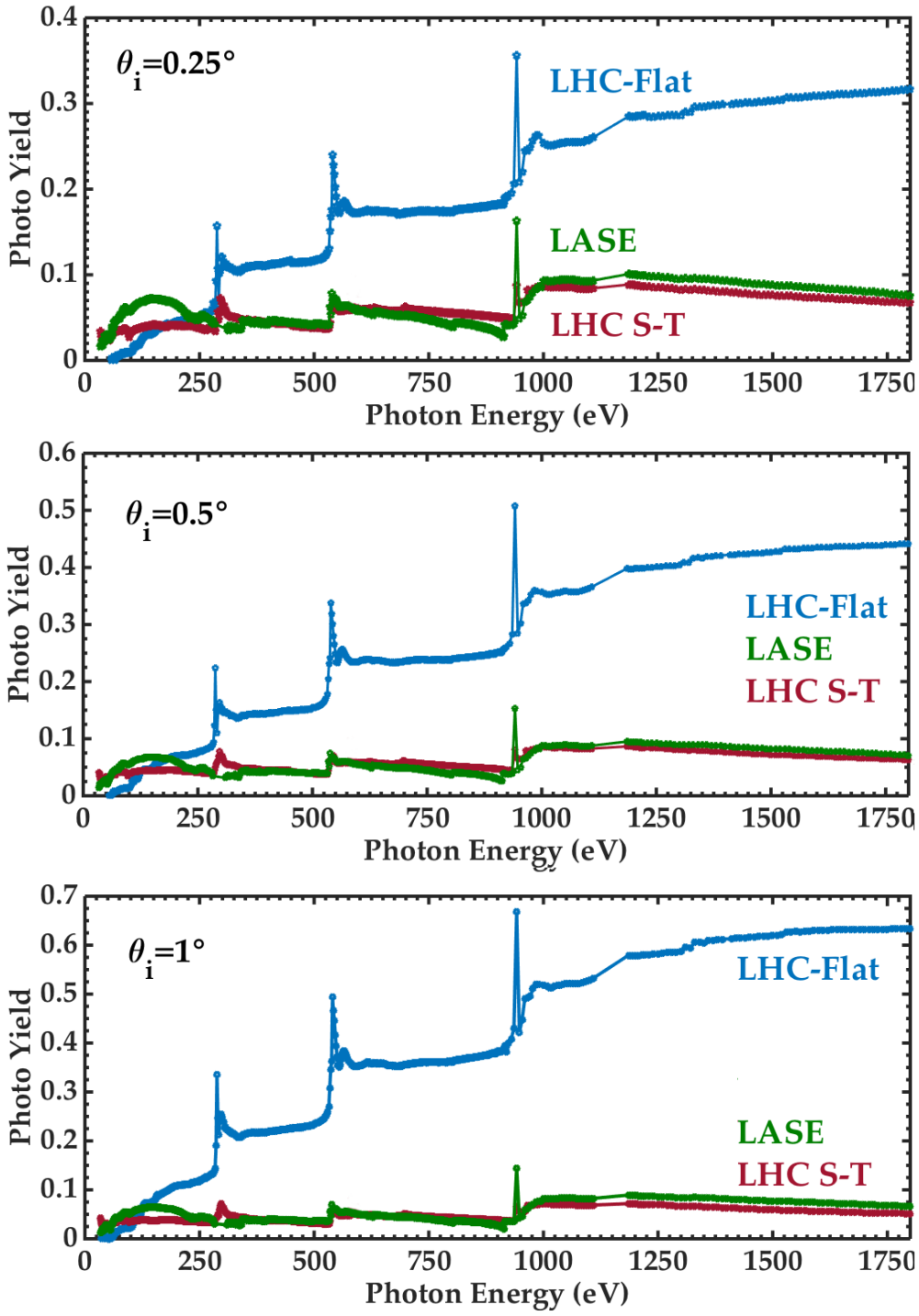

Figure 4.38: Photo Yield Vs Photon Energy of LHC-Flat, LHC-ST and LASE samples for $\theta_i = 0.25°$ (top panel), $\theta_i = 0.5°$ (middle panel), and $\theta_i = 1°$ (bottom panel) incidence angle.

Finally the comparison between the three copper samples R_t is shown in fig. 4.39. If we look at this figure, we can see that for each given incidence angle θ_i the total Reflectivity of the samples again is reduced after the surface treatments. In particular in comparison with the LHC-Flat sample (green points) the Saw-Tooth process produces a drop in total Reflectivity of more than one order of magnitude (red points), while the laser treatment results in a further decrease of two orders of magnitude (top panel, $\theta_i = 0.25°$). This effect is even more accentuated if we consider higher incidence angles.

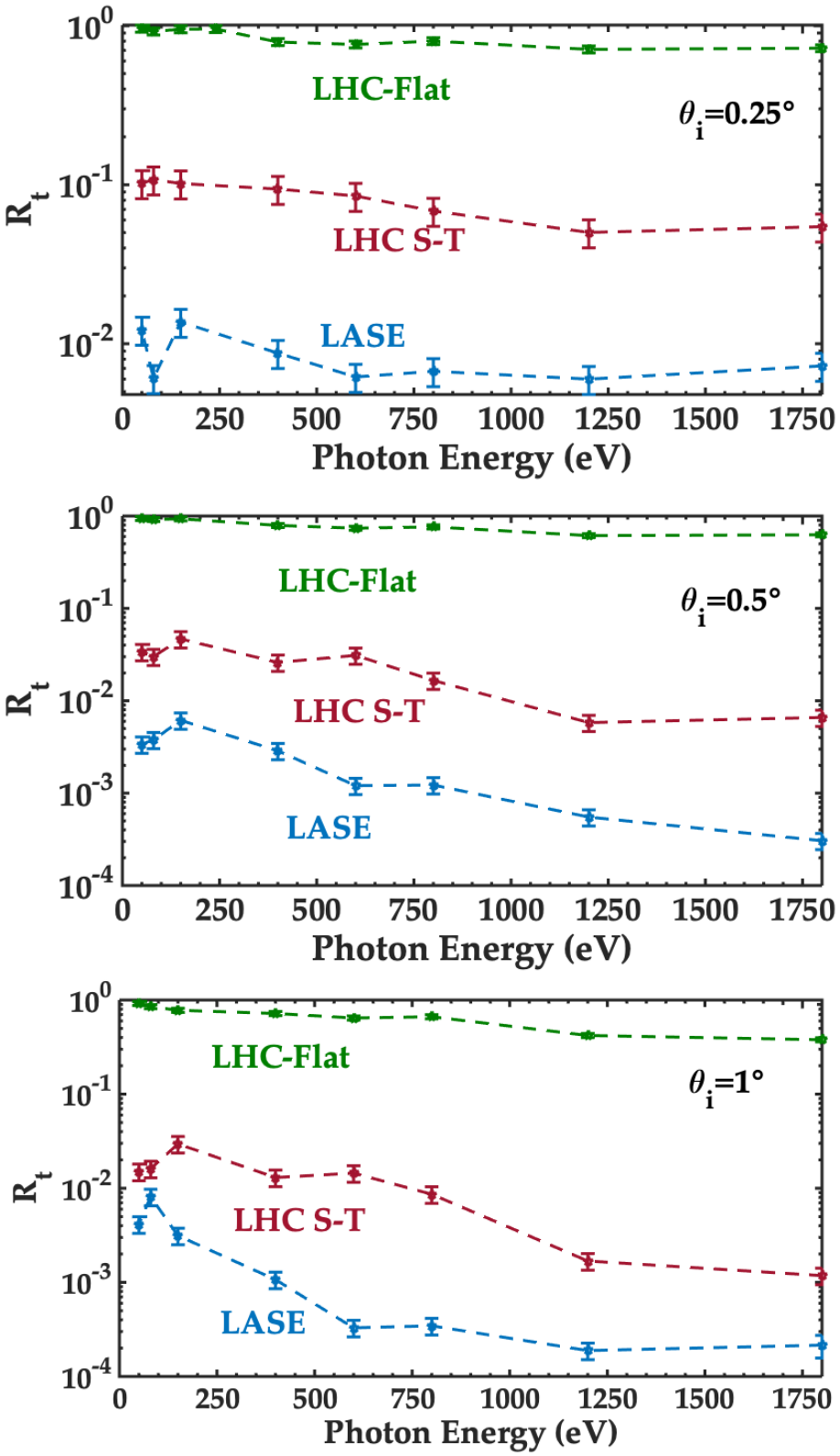

Figure 4.39: Total Reflectivity Vs Photon Energy of LHC-Flat, LHC-ST and LASE samples for $\theta_i = 0.25°$ (top panel), $\theta_i = 0.5°$ (middle panel), and $\theta_i = 1°$ (bottom panel) incidence angle.

Chapter 5

Conclusions

The work of this thesis aimed to study Reflectivity and Photo Yield properties of materials used or planned to be used in future high energy hadron colliders, as the Future Circular hadron Collider (FCC-hh). In order to reach the necessary strong magnetic field to bend the trajectories of the particles, the operation parameters of these machines impose the use of superconductiong magnets. These magnets need a very low operation temperature and in this conditions Synchrotron Radiation Heat Load is a crucial problem. Carbon coating of a smooth vacuum chamber surface was suggested to move the heat load from machine cold parts to warmer areas. At the same time Synchrotron Radiation (SR) can induce photon stimulated desorption and consequently vacuum instability. Moreover, SR impinging accelerator walls generates photoelectrons, which could trigger triggering a cascade process that culminates with the formation of an electron cloud and beam instability (coupled bunch and single bunch instabilities).

The photoelectrons are emitted mainly in dipoles, and, if they are generated in orbit plane, they could be pushed back to the wall. by the magnetic field. This happens when the electrons are generated directly by the Synchrotron Radiation. On the contrary, if they are generated in parallel to the magnetic field they will spiral around the field lines and will hit the chamber wall top and bottom generating secondary electrons. To avoid these problems the inner part of bending magnets must be protected by a beam screen able to minimize the production of photoelectrons.

As example, the beam screen proposed for FCC-hh is very complex and it is divided in two chambers. To reduce the synchrotron radiation reflectivity the secondary chamber is modulated with a saw-tooth profile. To mitigate the secondary emissions the inner chamber is, also, laser treated (LASE).

In this work Specular Reflectivity, PY and R_t have been measured in the photon energy region between 35 and 1800 eV for various Cu

samples surfaces as a function of their microscopic roughness, coating and macroscopic surface treatment. By this characterization several experimental parameters can be extracted. Such results were obtained, for the first time in this context, in very close to operational and geometrical conditions. The results here presented can be useful for the different simulation codes used to study and validate the design and performance of present and planned accelerators.

The experimental approach and the BESSY II Optics Beamline set-up, normally used to investigate optical surfaces, have been validate and confirmed to be well suited to study technical materials. Our data clearly show the importance of air contaminants in Reflectivity behaviour and the role played by roughness. They underline, in particular, the importance of scattered light and the need to consider the Total Reflectivity instead of Specular Reflectivity R_t to correctly simulate quantities related to the presence of SR in the accelerator.

Carbon coating increases both Specular and Total Reflectivities (as long as incidence angle is below its critical angle), in particular at high energy, i.e after the absorption edge of Carbon. Consequently it reduces absorption and related Heat Load. Photo Yield does not seem to significantly depend on roughness but it decreases with CC. PY shows peaks in correspondence of absorption edges. In presence of the Carbon coating the Cu L_{2-3} peak disappears and consequently a notably reduction in photoelectrons production occurs.

With the results of Reflectivity and Photo Yield measurements, I have compared the behaviour of copper flat samples (LHC Beam Screen, in flat zone, included), with and without 50 nm of Carbon Coating (CC), and Saw-toothed and laser ablated (made by the Science & Technology Facility Council (STFC)) copper samples.

For LASE Cu, the reflectivity has been found to be substantially lower than for untreated copper and for LHC Saw-Tooth sample, yielding very low electron densities and impingement rates on the vacuum chamber. However, the photo yield of Saw-Toothed copper and LASE are the same.

An important consideration to be made here, is that, in most of the aforementioned simulations, Reflectivity and PY are single numbers estimating how many photons and photoelectrons are produced by a surface once the total spectrum, called "White light" (WL) of the SR generated by the circulating beam, hits the surface. Our data shows that the study of "at wave-length metrology" of R, R_t and PY do strongly depend on the photon energy and on the angle of incidence. To include such dependencies in the simulation codes may indeed be quite complex and time consuming, but it may become a necessary step to improve and validate simulations.

We have reported here clear evidences that small angle scattering

occurs, as measured by R, and an even more significant number of large angle scattered photons will continue irradiating accelerator walls. The consequences of using such measured data into simulation codes will have to be carefully considered and a common effort will be needed to define the required acceptable approximation.

Acknowledgements

At the end of this Ph.D course I want to thank prof. M. Migliorati and Sapienza University, dr. R. Cimino, dr. R. Larciprete and all the INFN-NCV project MICA; dr. F. Schäfers, dr. A. Sokolov, dr. M. Sertsu and dr. F. Siewert of HZB. Thank for the opportunity you gave me.

We thank Alexander Pilz for his very useful cooperation in the preparation of the Cu sam- ples of different roughness and N. Kos for helping us with the preparation of some of the samples.

Re search leading to these results has also received funding by the project CALIPSOplus, under the Grant Agreement 730872 from the EU Framework Programme for Research and Innovation HORIZON 2020. We thank R. Valizadeh, O. Malyshev for providing us with the LASE sample.

I thankfully acknowledge HZB for for the allocation of synchrotron radiation beamtime and for financial support. I also thank Jana Buchheim and Grzegorz Gwalt of HMI for performing White Light Interferometer and AFM measurements (first roughness measurements) and dr.Francesca Scaramuzzo for the help of AFM measurements at CNIS (second roughness measurements). I want to thank also dr. M. Angelucci, dr. A. Liedl, I. Bellafont and dr. L.A. Gonzalez for the help during the long beamtime shifts.

I would also like to thank my family and dr. L. Spallino, V. Tullio, V. Sciarra, A. Balerna, E. Belli, M. Marongiu, A. Vannozzi, V. Martinelli. Thank you for being part of my world in these years. A special thanks to Simone, without him I would never have participated in the Ph.D admission test and this work would never have been written.

Grazie!

List of Figures

Bibliography

[1] URL: http://tlep.web.cern.ch/content/fcc-hh (cit. on p. 9).

[2] URL: https://www.helmholtz-berlin.de/media/media/nutzerdienst/experimental_facilities_bessy_ii_and_ber_ii.pdf (cit. on pp. 54, 55).

[3] URL: http://www.hamamatsu.com/resources/pdf/ssd/g1115_etc_kgpd1002e.pdf (cit. on p. 61).

[4] URL: http://gwyddion.net (cit. on p. 62).

[5] URL: https://www.helmholtz-berlin.de/forschung/oe/fg/nanometeroptik/methods/software_en.html (cit. on p. 63).

[6] D Alesini et al. "DA Φ NE Operation with Electron-Cloud-Clearing Electrodes". In: *Physical review letters* 110.12 (2013), p. 124801 (cit. on pp. 30, 31).

[7] V Anashin et al. "Photodesorption and power testing of the SR crotch-absorber for BESSY-II". In: *Proc. of EPAC-98, Stokholm* 3 (1998), 2163e5 (cit. on p. 15).

[8] M Angelucci, R Larciprete, and R Cimino. "Experimental investigation of adsorption and desorption processes of cryosorbed gases on proposed FCC accelerator walls". In: *FCC week*. Vol. Berlin, Germany. 2017 (cit. on pp. 22, 23).

[9] Gianluigi Arduini et al. "Transverse Behaviour of the LHC Proton Beam in the SPS: an Update". In: *Particle Accelerator Conference, 2001. PAC 2001. Proceedings of the 2001*. Vol. 3. IEEE. 2001, pp. 1883–1885 (cit. on pp. 16, 25).

[10] V Baglin. *Measurement of the primary phodesorption yield at 4.2 K, 77 K and room temperature in a quasi-closed geometry*. Tech. rep. 1996 (cit. on pp. 13, 14).

[11] V Baglin, IR Collins, and Oswald Gröbner. *Photoelectron yield and photon reflectivity from candidate LHC vacuum chamber materials with implications to the vacuum chamber design*. Tech. rep. 1998 (cit. on pp. 33, 34).

[12] V Baglin et al. *Cryogenic Beam Screens for High-Energy Particle Accelerators*. Tech. rep. CERN-ATS-2013-006. Geneva: CERN, 2013. URL: https://cds.cern.ch/record/1507613 (cit. on pp. 12, 49).

[13] V Baglin et al. "Measurements at EPA of vacuum and electron-cloud related effects". In: *Chamonix 2001, LEP performance* 5 (2001), pp. 10–10 (cit. on p. 34).

[14] V Baglin et al. *The secondary electron yield of technical materials and its variation with surface treatments*. Tech. rep. 2000 (cit. on p. 21).

[15] Eleonora Belli et al. "Single beam collective effects in FCC-ee due to beam coupling impedance". In: *arXiv preprint arXiv:1609.03495* (2016) (cit. on p. 27).

[16] Scott Berg. *Energy gain in an electron cloud during the passage of a bunch*. Tech. rep. CERN-LHC-Project-Note-97, 1997 (cit. on p. 18).

[17] Max Born and Emil Wolf. *Principles of Optics*. 1980 (cit. on p. 40).

[18] G Bregliozzi et al. "Vacuum stability and residual gas density estimation for the vacuum chamber upgrade of the ATLAS interaction region of the Large Hadron Collider". In: *Vacuum* 86.11 (2012), pp. 1682–1687 (cit. on p. 12).

[19] Yunhai Cai, M Pivi, and MA Furman. "Buildup of electron cloud in the PEP-II particle accelerator in the presence of a solenoid field and with different bunch pattern". In: *Physical Review Special Topics-Accelerators and Beams* 7.2 (2004), p. 024402 (cit. on p. 31).

[20] Sergio Calatroni et al. "First accelerator test of vacuum components with laser-engineered surfaces for electron- cloud mitigation". In: *Physical Review Accelerators and Beams* 20.11 (2017), p. 113201 (cit. on p. 50).

[21] L Calliari, M Filippi, and N Laidani. "Electron beam irradiation of hydrogenated amorphous carbon films". In: *Surface and Interface Analysis: An International Journal devoted to the development and application of techniques for the analysis of surfaces, interfaces and thin films* 36.8 (2004), pp. 1126–1129 (cit. on p. 29).

[22] P Chiggiato et al. "Observations of Electron Cloud Effects with the LHC Vacuum System". In: *Conf. Proc.* Vol. 110904. IPAC-2011-TUPS018. 2011, pp. 1560–1562 (cit. on pp. 23, 24).

[23] R Cimino. "interaction between beams and vacuum system walls". In: *Cern Accelerator School: Vacuum for Particle Accelerators*. Vol. Gloumslöv, Sweden. 2017 (cit. on p. 23).

[24] R Cimino, V Baglin, and IR Collins. "VUV synchrotron radiation studies of candidate LHC vacuum chamber materials". In: *Vacuum* 53.1-2 (1999), pp. 273–276 (cit. on pp. 30, 34–36, 68).

[25] R Cimino, V Baglin, and F Shäfers. "Potential Remedies for the High Synchrotron-Radiation-Induced Heat Load for Future Highest-Energy-Proton Circular Colliders". In: *Phys. Rev. Lett.* 115 (2015), p. 264804 (cit. on pp. 10, 45, 46, 77, 80).

[26] R Cimino and T Demma. "Electron clouds in accelerators". In: *Int. J. Mod. Phys. A* 29.17 (2014), 1430023 (65 pages) (cit. on pp. 16–19, 21, 26, 28, 29, 31).

[27] R Cimino et al. "Nature of the decrease of the secondary-electron yield by electron bombardment and its energy dependence". In: *Physical review letters* 109.6 (2012), p. 064801 (cit. on pp. 29, 30).

[28] Roberto Cimino et al. "Can low-energy electrons affect high-energy physics accelerators?" In: *Physical review letters* 93.1 (2004), p. 014801 (cit. on pp. 24, 25, 29).

[29] I Collins. "Electron Cloud Investigations". In: *CERN LHC-SL Seminar given on*. Vol. 11. 1999 (cit. on p. 49).

[30] DT Cromer and JT Waber. "Mean atomic scattering factors in electrons for free atoms and chemically significant ions". In: *International tables for X-ray crystallography* 4 (1974) (cit. on p. 41).

[31] Jean Daillant and Alain Gibaud. *X-ray and neutron reflectivity: principles and applications*. Vol. 770. Springer, 2008 (cit. on p. 79).

[32] Barbara Dalena et al. *Solenoid and Synchrotron Radiation effects in CLIC*. Tech. rep. 2009 (cit. on p. 4).

[33] T. Demma. "Electron cloud simulations for DAFNE". In: *ICFA Beam Dyn. Newslett.* 48 (2009), pp. 64–71 (cit. on p. 25).

[34] Philipp Dijkstal et al. *Simulation studies on the electron cloud build-up in the elements of the LHC Arcs at 6.5 TeV*. Tech. rep. 2017 (cit. on p. 33).

[35] G Dugan et al. "Observations and Predictions at CesrTA, and Outlook for ILC". In: *ECLOUD'12, La Biodola, Isola d'Elba, Italy (arXiv preprint arXiv:1308.1295*. 2013 (cit. on pp. 24, 25).

[36] F Eggenstein et al. "A reflectometer for at-wavelength characterization of XUV-reflection gratings". In: *Advances in Metrology for X-Ray and EUV Optics V*. Vol. 9206. International Society for Optics and Photonics. 2014, p. 920607 (cit. on p. 59).

[37] Berndt Feuerbacher, B Fitton, and Roy F Willis. *Photoemission and the electronic properties of surfaces*. John Wiley & Sons, 1978 (cit. on p. 20).

[38] H Fukuma. "Electron cloud effects at KEKB". In: (2002) (cit. on p. 19).

[39] Hitoshi Fukuma et al. "Recent observations of collective effects at KEKB". In: *e+ e-Factories* (2003) (cit. on p. 24).

[40] Miguel A Furman and Glen R Lambertson. "The electron-cloud instability in the arcs of the PEP-II positron ring". In: (1998) (cit. on p. 25).

[41] C Garion. "FCC-hh beam screen design and prototyping". In: *09th WP4 Meeting, EuroCirCol*. Vol. Frascati, Italy. 2018 (cit. on p. 47).

[42] J Gómez-Goñi, O Gröbner, and AG Mathewson. "Comparison of photodesorption yields using synchrotron radiation of low critical energies for stainless steel, copper, and electrodeposited copper surfaces". In: *Journal of Vacuum Science & Technology A: Vacuum, Surfaces, and Films* 12.4 (1994), pp. 1714–1718 (cit. on pp. 13, 15).

[43] LA Gonzalez, R Larciprete, and R Cimino. "The effect of structural disorder on the secondary electron emission of graphite". In: *AIP Advances* 6.9 (2016), p. 095117 (cit. on p. 27).

[44] Oswald Gröbner. *Dynamic outgassing*. Tech. rep. Cern, 1999 (cit. on p. 14).

[45] DR Grosso et al. "Effect of the surface processing on the secondary electron yield of Al alloy samples". In: *Physical Review Special Topics-Accelerators and Beams* 16.5 (2013), p. 051003 (cit. on p. 22).

[46] DR Grosso et al. "SEY of al samples from the dipole chamber of Petra III at DESY". In: *Proc-IPAC2011, San Sebastián, Spain* (2011) (cit. on p. 22).

[47] Gerardo Guillermo CantÃ³n et al. *JACoW: Comparing Behaviour of Simulated Proton Synchrotron Radiation in the Arcs of the LHC with Measurements*. Tech. rep. 2017 (cit. on p. 63).

[48] ZY Guo et al. "Studies on the Photoelectron Cloud at the BEPC". In: *APAC*. Vol. 1. 2001, p. 377 (cit. on p. 25).

[49] Eugene Hecht and A Zajac. *Optics*. Addison Wesley, New York, 2002 (cit. on p. 39).

[50] BL Henke, EM Gullikson, and JC Davis. *X-ray interactions-photoabsorption, scattering, transmission and reflection at e= 50-30,000 ev, z= 1-92 (vol 54, pg 181, 1993)*. 1993 (cit. on p. 41).

[51] Burton L Henke, Jerel A Smith, and David T Attwood. "0.1–10-keV x-ray-induced electron emissions from solids?Models and secondary electron measurements". In: *Journal of Applied Physics* 48.5 (1977), pp. 1852–1866 (cit. on p. 41).

[52] B Henrist et al. "The secondary electron yield of TiZr and TiZrV non-evaporable getter thin film coatings". In: *Applied surface science* 172.1-2 (2001), pp. 95–102 (cit. on pp. 27, 28).

[53] Giovanni Iadarola and Giovanni Rumolo. "Electron cloud in the CERN accelerators (PS, SPS, LHC)". In: *arXiv preprint arXiv:1309.6795* (2013) (cit. on p. 16).

[54] Giovanni Iadarola et al. *JACoW: Evolution of Python Tools for the Simulation of Electron Cloud Effects*. Tech. rep. 2017 (cit. on p. 33).

[55] M Izawa, Y Sato, and T Toyomasu. "The vertical instability in a positron bunched beam". In: *Physical review letters* 74.25 (1995), p. 5044 (cit. on p. 25).

[56] John David Jackson. *Classical electrodynamics*. John Wiley & Sons, 1999 (cit. on pp. 2, 4–6).

[57] JM Jimenez et al. *Electron cloud with LHC-type beams in the SPS: A review of three years of measurements*. Tech. rep. CERN, 2003 (cit. on p. 19).

[58] R Kersevan. "The Vacuum System of the Future Circula Collider: Challenges and Innovations". In: *Beam Dynamics meets Vacuum, Collimations, and Surfaces*. Vol. Geneva, Switzerland. 2017 (cit. on pp. 12, 27).

[59] AA Krasnov. "Molecular pumping properties of the LHC arc beam pipe and effective secondary electron emission from Cu surface with artificial roughness". In: *Vacuum* 73.2 (2004), pp. 195–199 (cit. on p. 27).

[60] E La Francesca et al. "Photo Reflectivity and Photoelectron Yield from Copper Technical Surfaces." In: *submitted* (2019) (cit. on p. 63).

[61] E La Francesca et al. "Reflectivity and Photo Yield measurements of technical surfaces". In: *FCC Week 2017,* vol. Berlin, Germany. 2017 (cit. on p. 63).

[62] E La Francesca et al. "Study of Reflectivity and Photo Yield on FCC-hh proposed beam screen surfaces". In: *FCC Week 2018*. Vol. Amsterdam, Nederlands. 2017 (cit. on p. 63).

[63] Rosanna Larciprete et al. "Evolution of the secondary electron emission during the graphitization of thin C films". In: *Applied Surface Science* 328 (2015), pp. 356–360 (cit. on pp. 27, 28).

[64] Karl-Heinz Leitz et al. "Metal ablation with short and ultrashort laser pulses". In: *Physics Procedia* 12 (2011), pp. 230–238 (cit. on p. 50).

[65] A Liedl et al. "Metrology for High Energy Accelerator: SR at wave-length Investigations on Technical Surface". In: *International Workshop on X-ray Optics and Metrology (IWXM 2018)*. Vol. Taiwan. 2018 (cit. on p. 63).

[66] A Liedl et al. "Photo reflectivity and PEY of technical surfaces". In: *ECLOUD'18, Isola d'Elba, Italy (arXiv preprint arXiv:1308.1295*. 2013 (cit. on p. 63).

[67] N Mahne et al. "Photon reflectivity distributions from the LHC beam screen and their implications on the arc beam vacuum system". In: *Applied surface science* 235.1-2 (2004), pp. 221–226 (cit. on pp. 34, 35, 92).

[68] S Mobilio, F Boscherini, and C Meneghini. *Synchrotron Radiation*. John Wiley & Sons, 1999 (cit. on p. 2).

[69] Stephen Myers. "The large hadron collider 2008–2013". In: *International Journal of Modern Physics A* 28.25 (2013), p. 1330035 (cit. on p. 48).

[70] L. Nevot and 761 (1980). P. Croce Rev. Phys. Appl. 15. "Caractérisation des surfaces par réflexion rasante de rayons X. Application à l'étude du polissage de quelques verres silicates". In: *Rev. Phys. Appl.* 15 (1980), p. 761 (cit. on p. 44).

[71] Michiru Nishiwaki and Shigeki Kato. "Graphitization of inner surface of copper beam duct of KEKB positron ring". In: *Vacuum* 84.5 (2009), pp. 743–746 (cit. on p. 29).

[72] Michiru Nishiwaki and Shigeki Kato. "Influence of electron irradiation and heating on secondary electron yields from non-evaporable getter films observed with in situ x-ray photoelectron spectroscopy". In: *Journal of Vacuum Science & Technology A: Vacuum, Surfaces, and Films* 25.4 (2007), pp. 675–679 (cit. on p. 29).

[73] Michiru Nishiwaki and Shigeki Kato. "Study on secondary electron emission from carbon materials". In: *Journal of the Vacuum Society of Japan* 48 (2006), pp. 118–120 (cit. on p. 29).

[74] Kazuhito Ohmi et al. *Study of Electron Cloud Instabilities in FCC-hh*. Tech. rep. 2015 (cit. on p. 7).

[75] F Perez et al. *Analysis of beam-induced vacuum effects*. Tech. rep. EuroCirCol-P2-WP4-D4.4. ALBA, CERN, 2018 (cit. on pp. 10–12, 15, 47, 49–52).

[76] F Perez et al. *Preliminary beam screen and beam pipe engineering design*. Tech. rep. EuroCirCol-P2-WP4- D4.3. ALBA, CERN, 2018 (cit. on p. 47).

[77] HR Philipp and Edward D Palik. "Handbook of optical constants of solids". In: *Palik (Ed.)(Academic, Orlando 1985) p* 749 (1985), p. 74 (cit. on p. 41).

[78] M Pivi et al. "Secondary electron yield and groove chamber tests in PEP-II". In: *Particle Accelerator Conference, 2007. PAC. IEEE*. IEEE. 2007, pp. 1997–1999 (cit. on p. 27).

[79] M Pivi et al. "Sharp reduction of the secondary electron emission yield from grooved surfaces". In: *Journal of Applied Physics* 104.10 (2008), p. 104904 (cit. on pp. 27–29).

[80] MTF Pivi et al. *Recommendation for Mitigations of the Electron Cloud Instability in the ILC*. Tech. rep. Lawrence Berkeley National Lab.(LBNL), Berkeley, CA (United States), 2011 (cit. on p. 26).

[81] Francesco Ruggiero. "Electron cloud in the LHC". In: *Beam dynamics issues for e+ e- factories. Proceedings, Advanced ICFA Workshop, ICFA'97, Frascati, Italy, October 20-25, 1997*. 1998, pp. 437–443 (cit. on p. 15).

[82] Giovanni Rumolo and Frank Zimmermann. "Electron cloud simulations: beam instabilities and wakefields". In: *Physical Review Special Topics-Accelerators and Beams* 5.12 (2002), p. 121002 (cit. on pp. 18, 19).

[83] F Schäfers and R Cimino. "Soft X-ray reflectivity: from quasi-perfect mirrors to accelerator walls". In: *arXiv preprint arXiv:1308.1295* (2013) (cit. on pp. 34, 36, 37, 41–43).

[84] F Schäfers and M Krumrey. *REFLEC-A program to calculate VUV and soft x-ray optical elements and synchrotron radiation beamlines*. Tech. rep. Technischer Bericht TB 201, BESSY, Berlin, 1996 (cit. on p. 41).

[85] Frank Siewert. "Slope error and surface roughness". In: *Modern Developments in X-Ray and Neutron Optics*. Springer, 2008, pp. 175–179 (cit. on p. 43).

[86] A Sokolov et al. "At-wavelength metrology facility for soft X-ray reflection optics". In: *Review of Scientific Instruments* 87.5 (2016), p. 052005 (cit. on p. 55).

[87] AA Sokolov et al. "An XUV optics beamline at BESSY II". In: *Proc. SPIE*. Vol. 9206. 2014, 92060J (cit. on p. 55).

[88] L Spallino et al. "Study of Vacuum stability and desorption processes at low temperature for various FCC-hh candidate materials." In: *FCC week 2018*. Vol. Amsterdam, Nederlands. 2018 (cit. on p. 47).

[89] G Stupakov and M Pivi. *Suppression of the effective secondary emission yield for a grooved metal surface*. Tech. rep. CERN, 2004 (cit. on pp. 27, 29).

[90] Y Suetsugu. "High-Intensity Synchrotron Radiation Effects". In: *arXiv preprint arXiv:1608.02462* (2016) (cit. on pp. 8, 26).

[91] Y Suetsugu et al. "First experimental and simulation study on the secondary electron and photoelectron yield of NEG materials (Ti–Zr–V) coating under intense photon irradiation". In: *Nuclear Instruments and Methods in Physics Research Section A: Accelerators, Spectrometers, Detectors and Associated Equipment* 554.1-3 (2005), pp. 92–113 (cit. on p. 22).

[92] Yusuke Suetsugu et al. "Design and construction of the SuperKEKB vacuum system". In: *Journal of Vacuum Science & Technology A: Vacuum, Surfaces, and Films* 30.3 (2012), p. 031602 (cit. on pp. 26, 27).

[93] Richard Talman. "Scaling behavior of circular colliders dominated by synchrotron radiation". In: *International Journal of Modern Physics A* 30.23 (2015), p. 1544003 (cit. on pp. 5, 8).

[94] P Thieberger et al. "Secondary-electron yields and their dependence on the angle of incidence on stainless-steel surfaces for three energetic ion beams". In: *Physical Review A* 61.4 (2000), p. 042901 (cit. on p. 17).

[95] Makoto Tobiyama et al. "Coupled bunch instability caused by an electron cloud". In: *Physical Review Special Topics-Accelerators and Beams* 9.1 (2006), p. 012801 (cit. on p. 25).

[96] Do H Tomboulian and PL Hartman. "Spectral and angular distribution of ultraviolet radiation from the 300-Mev Cornell synchrotron". In: *Physical Review* 102.6 (1956), p. 1423 (cit. on p. 2).

[97] Reza Valizadeh et al. "Low secondary electron yield engineered surface for electron cloud mitigation". In: *Applied Physics Letters* 105.23 (2014), p. 231605 (cit. on p. 51).

[98] Reza Valizadeh et al. "Reduction of secondary electron yield for E-cloud mitigation by laser ablation surface engineering". In: *Applied Surface Science* 404 (2017), pp. 370–379 (cit. on pp. 50, 51, 94).

[99] L Wang. *Solenoid effects on an electron cloud*. Tech. rep. SLAC National Accelerator Lab., Menlo Park, CA (United States), 2018 (cit. on pp. 31, 32).

[100] L Wang, TO Raubenheimer, and G Stupakov. "Suppression of secondary emission in a magnetic field using triangular and rectangular surfaces". In: *Nuclear Instruments and Methods in Physics Research Section A: Accelerators, Spectrometers, Detectors and Associated Equipment* 571.3 (2007), pp. 588–598 (cit. on p. 27).

[101] F Zimmermann. "Electron-cloud effects in past and future machines-Walk through 50 years of electron-cloud studies". In: *arXiv preprint arXiv:1308.1274* (2013) (cit. on p. 49).

[102] Frank Zimmermann. "Review of single bunch instabilities driven by an electron cloud". In: *Physical Review Special Topics-Accelerators and Beams* 7.12 (2004), p. 124801 (cit. on pp. 24, 25).